

Optical characterization of the Si:Se⁺ spin-photon interface

by

Adam DeAbreu

B.Sc., Simon Fraser University, 2016

Thesis Submitted in Partial Fulfillment of the
Requirements for the Degree of
Master of Science

in the
Department of Physics
Faculty of Science

© Adam DeAbreu 2018
SIMON FRASER UNIVERSITY
Summer 2018

Copyright in this work rests with the author. Please ensure that any reproduction
or re-use is done in accordance with the relevant national copyright legislation.

Approval

Name: Adam DeAbreu

Degree: Master of Science (Physics)

Title: Optical characterization of the Si:Se⁺ spin-photon interface

Examining Committee: **Chair:** Nancy Forde
Professor

Stephanie Simmons
Senior Supervisor
Associate Professor

Michael Thewalt
Supervisor
Professor

Simon Watkins
Internal Examiner
Professor

Date Defended: August 27, 2018

Abstract

The combination of both matter qubits and photonic qubits presents a very promising method for generating entanglement between qubits in order to scale up both quantum computing and quantum communication platforms. Hosting both qubits in silicon would be a favourable approach as silicon has not only the most mature microelectronics industry but also the most mature photonics industry. Singly ionized selenium donors (Si:Se^+) have recently been identified as a possible candidate. Si:Se^+ possess the excellent coherence lifetimes of conventional donor spin qubits in silicon but additionally has photonic access to the spin states at a convenient wavelength, $2.9 \mu\text{m}$. The spin-photon interface of Si:Se^+ has the potential to be the basis for an integrated, all silicon, quantum computer. For this work we made custom samples with the specific purpose of measuring the crucial optical properties that determine the viability of the Si:Se^+ spin-photon interface as a basis for a quantum architecture. We present photoluminescence, absorption, hole burning, and magnetic resonance experiments towards the characterization of the Si:Se^+ spin-photon interface. We determined a transition dipole moment of 1.96 ± 0.08 Debye, a lower bound for the zero-phonon line fraction of $> 15.1 \pm 0.3 \%$, and a lower bound for the radiative efficiency of $> 0.75 \pm 0.08 \%$. Further results of the peak and area conversion factors and the dependence of peak energy and linewidth on electrically neutral impurities are also presented.

Keywords: silicon; selenium donors; photonics; quantum information

Acknowledgements

Physics is best done as a collaborative effort and I have had the good fortune of having the best collaborators. First and foremost, I would like to thank my supervisors, Stephanie Simmons and Mike Thewalt, for their endless support and guidance. Your seemingly infinite stores of knowledge and expertise are the foundation upon which this work is built.

I must thank my fellow students, Kevin Morse, Rohan Abraham, Camille Bowness, Timothy Richards, Laurent Bergeron, Alex Kurkjian, and Camille Chartrand, for making every day in the lab an absolute joy.

Finally, I would like to thank my Mom and Dad for their tireless support and encouragement, without which I would not have made it to where I am today. You shaped who I am and lit the spark of curiosity and wonder that led to my love of science.

To everyone else who have come along on this crazy adventure, I thank you all.

Table of Contents

Approval	ii
Abstract	iii
Acknowledgements	iv
Table of Contents	v
List of Tables	vii
List of Figures	viii
1 Introduction	1
1.1 Quantum Information	1
1.2 Spin-Photon Interface	3
1.3 Donors in Silicon	4
2 Background Theory	7
2.1 Properties of Bulk Silicon	7
2.2 Silicon as an Optical Medium	8
2.3 Optical Properties	11
2.3.1 Broadening Mechanisms	15
2.3.2 Hole Burning	16
2.4 Magnetic Resonance	18
2.4.1 Instantaneous Diffusion and Tip-Angle	22
2.5 Selenium Donors	23
2.5.1 Se Spin-Photon Interface	26
2.6 Diffusion	28
3 Sample Preparation and Experimental Techniques	30
3.1 Sample Preparation	30
3.2 FTIR	35
3.2.1 Photoluminescence	38

3.2.2	Absorption	39
3.2.3	Hole Burning	40
3.3	Magnetic Resonance and Tip-Angle	41
3.3.1	Laser/RF Scan	41
3.3.2	Pulsed RF Experiments	42
4	Experimental Results and Discussion	44
4.1	Impurities	44
4.1.1	Impurities – Photoluminescence	44
4.1.2	Impurities – Absorption	46
4.1.3	Impurities – Profiles	49
4.2	Se ⁺ Optical Properties	51
4.2.1	Se ⁺ – Photoluminescence	51
4.2.2	Se ⁺ – Linewidth	53
4.2.3	Se ⁺ – Transition Dipole Moment	56
4.2.4	Se ⁺ – Tip-Angle	59
4.2.5	Se ⁺ – Radiative Lifetime and Conversion Factors	63
4.2.6	Se ⁺ – Hole Burning	64
4.3	Se ⁰ Optical Properties	66
5	Conclusion and Future Work	68
5.1	Se ⁺ Spin-Photon Interface Assessment	68
5.2	Future Work	70
	Bibliography	72

List of Tables

Table 3.1	Name, silicon substrate, estimated doping, and diffusion source for all samples studied in this work. Sample(s) grouped together were diffused in the same ampule. Sample names beginning with a ‘w’ are wafer samples. Doping values marked with a † are from Devyatykh et al. [100] all other doping values are estimates.	34
Table 4.1	The boron, oxygen, and carbon concentrations of the samples studied in this paper. Impurities identified from photoluminescence spectra are also shown. Samples grouped together are from the same ampule. Impurities marked with an * were not observed but inferred from spectra of other samples from the same ampule. Concentration values marked with a † are from Devyatykh et al. [100], all other values are determined from absorption spectra features.	49
Table 4.2	Diffusion properties of impurities seen in wafer samples. All values from <i>Intrinsic Point Defects, Impurities, and Their Diffusion in Silicon</i> [99].	50
Table 4.3	The conversion factors to convert from peak absorption coefficient of the 1s:A \Rightarrow 1s:T ₂ Γ ₇ spectral line to the concentration of Se ⁺ for the specified isotopic combinations. These values are all calculated at a temperature of 1.8 K and a resolution of 0.1 cm ⁻¹	64
Table 4.4	The conversion factors to convert from peak absorption coefficient of the Se ⁰ 1s:A \Rightarrow 1s:T ₂ spectral line to the average concentration of Se ⁰ for the specified isotopic combinations. These values are all calculated at a temperature of 1.8 K and a resolution of 0.1 cm ⁻¹	67
Table 5.1	Optical properties of the Si:Se system determined in this work. μ is the transition dipole moment, f is the area conversion factor, $\tau_{\text{res}}^{\text{rad}}$ is the resonant radiative lifetime, $\tau_{\text{total}}^{\text{rad}}$ is the total radiative lifetime, and τ_{exc} is the excited state lifetime.	69

List of Figures

Figure 2.1	Schematic diagram showing donor (left) and acceptor (right) levels in the silicon bandgap as well as a compensated system (center) with the donor level ionized and the acceptor level filled. The conduction band (CB) and valence band (VB) are split by the energy of the bandgap, E_g . The ionization energy of the donor level, E_i , is also shown.	8
Figure 2.2	Schematic diagram showing the energy-momentum phase space of the indirect silicon bandgap. Optical transitions in silicon without donors (a) and with a donor level present (b) are shown. Red arrows represent an absorbed or emitted photon, green arrows represent emitted phonons, and black arrows represent the energy change of electrons (blue circles) and holes (white circles) due to absorption/emission of photons/phonons. a) From left to right the transitions are: above bandgap light is absorbed; a photon is emitted without a phonon; a photon is emitted with a momentum conserving phonon. b) From left to right the transitions are: non-resonant light ionizing a donor and subsequent phonon cascade back to an excited state; resonant light exciting a transition from the ground state to an excited state; emission of resonant light as an electron decays from an excited state to the ground state.	10
Figure 2.3	Schematic diagram illustrating the effect of spectral hole burning from a laser tuned to the peak of an inhomogeneously broadened spectral line. The total linewidth, $\Delta\omega_{\text{total}}$, is due to many shifted transitions, each with a homogeneous linewidth, $\Delta\omega_{\text{hom}}$. The laser, tuned to the peak of the spectra (red dashed line, ω_{laser}), burns a hole of linewidth $\Delta\omega_{\text{hole}} = 2\Delta\omega_{\text{hom}}$	18
Figure 2.4	Bloch diagrams showing a) a $\pi/2$ rotation about the x -axis and b) T_1 and T_2 decay processes. See text for details.	19
Figure 2.5	RF pulse sequences used in this work. (a) Rabi pulse sequence. (b) Hahn-echo pulse sequence. (c) Tip-angle pulse sequence for arbitrary refocusing pulse angle, θ	21

Figure 2.6	Si: ⁷⁷ Se energy level diagram. (a) The energy levels of the neutral charge state, Se ⁰ . Valley-orbit interactions split the 1s state into 1s:A, 1s:T ₂ , and 1s:E. The 1s:T ₂ state is further split into a spin singlet and spin triplet due to an exchange interaction with the second bound electron. (b) The energy levels of the singly-ionized charge state, Se ⁺ . Valley-orbit interactions split the 1s state into 1s:A, 1s:T ₂ , and 1s:E. Spin-valley interactions split the 1s:T ₂ level into Γ_7 and Γ_8 . Electron-nucleus hyperfine interaction splits the 1s:A level into singlet, S, and triplet, T states. (c) Under the effects of a magnetic field Γ_7 splits with (anti-) alignment with the magnetic field. The singlet and triplet states also split with magnetic field. At high magnetic field the states can be described by the electron and nuclear spins, single and double arrow respectively. The energies of the relevant transitions for this thesis work have been indicated.	24
Figure 2.7	Absorption spectra comparing different isotopic combinations of silicon and selenium. As the samples become more isotopically pure the linewidth narrows significantly and the two transitions, T \Rightarrow 1s:T ₂ Γ_7 and S \Rightarrow 1s:T ₂ Γ_7 become resolvable. (Inset) the lambda transition composed of the two transitions T \Rightarrow 1s:T ₂ Γ_7 and S \Rightarrow 1s:T ₂ Γ_7 . . .	26
Figure 2.8	Schematic diagram of a cavity coupled to an atomic system with a lambda transition. The lambda transition is composed of the two transition d \Rightarrow e and c \Rightarrow e. The cavity frequency, ω_c is resonant with the c \Rightarrow e transition and is thus coupled. Probing the transmission spectra of the cavity will give the spectra shown to the right depending on the state of the atomic system. If in the detuned state, d, there is a single peak at the bare cavity frequency (blue spectra). If in the coupled state, c, there will be two peaks (red spectra) split by $2g$ which is proportional to the transition dipole moment, μ . . .	27
Figure 3.1	Calculated concentration profiles after a 1200 °C diffusion for 7 days for (a) a 0.5 mm thick silicon wafer diffused with SeO ₂ (ie both Se and O) and (b) a 2 mm thick silicon block sample diffused with elemental Se (ie only Se). The three different boron levels are also shown.	32
Figure 3.2	A comparison of the surface damage present for samples from Ampule 1 and Ampule 2. Images of samples (a) ^{nat} Si: ⁷⁷ Se:Al and (b) ^{nat} Si: ⁷⁸ Se:Al. Surface profilometry of samples (c) ^{nat} Si: ⁷⁷ Se:Al and (d) ^{nat} Si: ⁷⁸ Se:Al. Note that the surface profile of ^{nat} Si: ⁷⁷ Se:Al, (c), is plotted on an axis 10 times smaller than ^{nat} Si: ⁷⁸ Se:Al, (d). . . .	33

Figure 3.3	Schematic diagram showing the three configurations in which we use Fourier transform infrared spectroscopy. (a) Components highlighted in green are used for photoluminescence measurements. A liquid-helium cooled sample is excited with a laser source and the emission from the sample is collected as the source light to the FTIR. (b) Components highlighted in orange are used for absorption measurements. A broad band light is used as the source and a liquid-helium cooled sample is placed in the FTIR arm before the detector. (c) Components highlighted in red are used for hole burning measurements. This is the same setup as absorption with the addition of a perpendicular laser used to resonantly excite a transition.	38
Figure 3.4	Experimental setups used for magnetic resonance and tip-angle experiments. In both setups a liquid-helium cooled sample is illuminated with a laser source. A Helmholtz coil pair surrounding the cryostat is used to generate a static, vertical, magnetic field, B_0 . The sample is in a resonator with an RF magnetic field, B_1 , perpendicular B_0 . (a) Setup used for both laser and RF scans. The laser light is modulated by a chopper and a lock-in measurement is made as either the laser or the RF source is scanned. (b) Setup used for pulsed RF experiments. A computer controls the timing of RF pulses, shutter open/close, and triggering of a counter.	41
Figure 3.5	Schematic diagram of the transient area readout method. The integrated signal of Bin A is subtracted from Bin B to obtain the transient area (hatched area). The transient area for three different final state distributions is shown: 0 % in readout state (red), 50 % in readout state (blue), 100 % in readout state (orange).	43
Figure 4.1	Photoluminescence spectra of the bound exciton (BE) no-phonon (NP) region showing donor and acceptor bound exciton recombination. The NP BE recombination luminescence lines of multiple impurities are indicated. B_{2e} corresponds to the recombination of two excitons at a boron center. Gallium, arsenic, and aluminum have been unintentionally introduced during the diffusion process (see text). An additional, unknown, line (?) is present after polishing and etching the samples. A spectra of $w^{28}\text{Si}:\text{Se}:\text{LB}$ before polishing/etching is not shown as the surface damage was too extensive to resolve any spectral features. Spectra were recorded at a resolution of 1 cm^{-1} . At this resolution the splitting of the B_{NP} line is partially resolved (*) [78].	45

Figure 4.2	Absorption spectra of the $w^{28}\text{Si}:^{77}\text{Se}:\text{IB}$ sample before and after diffusion. The phonon mode used to calculate the pathlength is labeled TA + TO (TA: transverse acoustic, TO: transverse optic). The carbon local vibrational mode (LVM) at 607 cm^{-1} was used to calculate [C]. The boron $2p'$ line at 669 cm^{-1} was used to calculate [B]. The absence of the electronic boron lines indicate that the sample is fully compensated. The oxygen LVM at 1136 cm^{-1} was used to calculate [O]. The spectra are shown at the relevant resolutions for the peak conversion factors used. To the left of the split axis the spectra is at a resolution of 1 cm^{-1} . To the right of the split the spectra is at a resolution of 0.5 cm^{-1} . The right side has also been multiplied by a factor of 0.2 for ease of viewing.	47
Figure 4.3	Calculated concentration profiles for the impurities introduced during diffusion of (a) a wafer sample, and (b) a block sample. It was seen that all impurities are present in wafer samples, although, Al was only seen in Ampule 2 sample, while only C and O were confirmed to be in the block samples. It is assumed that the impurities are introduced at the solid solubility limit at $1200\text{ }^\circ\text{C}$ and diffused for 7 days. The boron levels of the different wafer samples studied are shown as well.	51
Figure 4.4	The photoluminescence spectrum of the $\text{Se}^+ 1s:\text{T}_2\Gamma_7 \Rightarrow 1s:\text{A}$ transition measured at a resolution of 1 cm^{-1} . The resonant zero-phonon line is labeled ZPL. The spectrum has been normalized to the ZPL line and is clipped. The phonon sideband is visible to lower energies. (Upper inset) The same spectrum showing the unclipped height of the ZPL. The phonon density of states [112] in silicon is overlaid with the peaks in the distribution labeled by the phonon mode (T/L: transverse/longitudinal, O/A: optic/acoustic) and the direction in the lattice labeled by the symmetry site (L, W, X).	53
Figure 4.5	High resolution scans of the $\text{Se}^+ 1s:\text{A} \Rightarrow 1s:\text{T}_2\Gamma_7$ for all ^{28}Si samples. The different peak positions and linewidths are due to different [O] (see Fig. 4.6). The $^{28}\text{Si}:^{78}\text{Se}:\text{IB}$ sample had zero transmission at the peak for high resolution scans so we instead show a low resolution scan to show the peak position and the high resolution scan of the $^{80}\text{Se} 1s:\text{A} \Rightarrow 1s:\text{T}_2\Gamma_7$ in the same sample to compare linewidth. The resolution used for each spectra is listed in the legends.	54

Figure 4.6	(a) Linewidth of the $\text{Se}^+ 1s:A \Rightarrow 1s:T_2\Gamma_7$ transition versus $[\text{O}]$ for all ^{28}Si samples, fit with a line. The selenium isotope of the transition is indicated. (b) The peak energy of the $\text{Se}^+ 1s:A \Rightarrow 1s:T_2\Gamma_7$ transition versus $[\text{O}]$ for all ^{28}Si samples. The two selenium isotopes studied are fit separately. In both (a) and (b) the data corresponding to the $^{28}\text{Si}:^{77}\text{Se}:\text{IB}$ sample are marked with an arrow. These data points are excluded from the fits.	56
Figure 4.7	Absorption spectra of all wafer samples showing the (a) $^{77}\text{Se}^0 1s:A \Rightarrow 1s:T_2$, (b) $^{77}\text{Se}^+ 1s:A \Rightarrow 1s:T_2\Gamma_7$, (c) $^{78}\text{Se}^0 1s:A \Rightarrow 1s:T_2$, and (d) $^{78}\text{Se}^+ 1s:A \Rightarrow 1s:T_2\Gamma_7$ transitions for the wafer samples. The different lineshapes and absorption strengths are due to the different isotopic combinations and the different boron concentrations. Higher $[\text{B}]$ samples have stronger Se^+ transitions and weaker Se^0 transitions, and vice-versa for lower $[\text{B}]$ samples. All spectra were measured at 1.8 K at a resolution of 0.1 cm^{-1}	57
Figure 4.8	Transition dipole moment, μ , for all wafer samples using the estimate $[\text{Se}^+]=[\text{B}]$. The average transition dipole moment is 1.73 ± 0.05 Debye which is a lower bound (see text). The points are coloured based on which ampule the sample was from.	58
Figure 4.9	(a) Laser scan of the $^{77}\text{Se}^+ 1s:A \Rightarrow 1s:T_2\Gamma_7$ transition of the $w^{28}\text{Si}:^{77}\text{Se}:\text{IB}$ sample. (b) RF scan of the singlet to triplet transitions of the $w^{28}\text{Si}:^{77}\text{Se}:\text{IB}$ sample with the laser tuned to the triplet peak. (c) Rabi pulse of the $S \Leftrightarrow T_+$ transition. In this instance the time to rotate the spins by π radians was measured to be 14 μs . . .	60
Figure 4.10	Repeated measurements of a $3\pi/4$ tip-angle pulse sequence (black inset). The baseline subtracted transient area was determined by taking the difference of back to back measurements at a given dark time, one using the black inset pulse sequence, and one using the blue inset blue sequence. The blue inset pulse sequence gives a measure of the decoherent baseline (see text). Using maximum magnitude at each dark time the envelope was fit to an exponential with time constant, $T_2 = 10.1 \pm 0.4$ ms. This envelope is mirrored about the y-axis to show the expected minimum magnitude envelope. The drops in phase noise are indicated by red arrows at ≈ 0 and ≈ 33 ms. . .	61
Figure 4.11	Inverse $T_{2,\theta}$ coherence times measured from tip-angle pulse sequences at different angles, θ . The result was fit with a line and the concentration, $[\text{Se}^+] = (5.2 \pm 0.4) \times 10^{14} \text{ cm}^{-3}$ was extracted which is lower than the boron concentration, $[\text{B}] = (5.9 \pm 0.8) \times 10^{14} \text{ cm}^{-3}$. . .	62

Figure 4.12	Absorption coefficient spectra of the $^{28}\text{Si}:^{77}\text{Se}:\text{IB}$ sample with and without a hole burning laser tuned to the triplet transition (red arrow). The difference is also shown in which the hole and anti-hole are visible. The resolution is 0.002 cm^{-1}	65
Figure 4.13	Absorption coefficient area of $[\text{Se}^0]$ versus $[\text{Se}^+]$ for all wafer samples studied. The samples from Ampule 1 and Ampule 2 have been fit with a lines separately, dashed blue and dashed orange lines respectively. From the fit to Ampule 2 samples we obtained a lower bound for the Se^0 conversion factor, $f_{\text{Se}^0} > (1.5 \pm 0.5) \times 10^{15}\text{ cm}^{-1}$ (see text). .	66

Chapter 1

Introduction

1.1 Quantum Information

The progression of technological advancement is encapsulated in Moore's law [1] – stating the doubling every year in the number of components per integrated circuit. However, since first described in 1965, physical devices have increasingly fallen short of this trend [2]. In 1975 Gordon Moore revised the prediction to doubling every two years, and in 2015 he predicted that Moore's law would be "...dying in the next decade or so" [3].

This saturation of Moore's law is due to transistors becoming so small – approaching the atomic scale – that quantum effects begin to limit their functionality [4, 5]. However, this is not the end of technological advancement; if quantum mechanics is limiting classical computing then we will harness these quantum effects to create a new manner of computation – quantum computing.

Quantum computing is not only the continuation of Moore's law, but a means to unlock problems otherwise impossible for classical computing. Whole classes of problems have resource requirements that scale exponentially with the size of the problem when working with a classical resource, making them intractable for classical computing. These same problems scale polynomially when a quantum resource is used (see <https://math.nist.gov/quantum/zoo/> [6] for a comprehensive list of quantum algorithms). This is the power of quantum computers: the ability to outscale classical computers and solve otherwise inaccessible problems.

The idea of quantum computing was first proposed by Richard Feynman in 1981 where he envisioned a programmable quantum computer as a means to simulate other quantum mechanical systems [7]. A system composed of 50 spin-1/2 particles would require a classical computer to store 2^{50} numbers to describe the system (the complex values defining each particle). Assuming single precision (32 bits) this requires $\approx 3.2 \times 10^{16}$ bits, or 4 Petabytes, to store the state of 50 particles. Already this begins to strain the memory capabilities of the latest supercomputer: IBM Summit with ≈ 10 Petabytes of memory [8]. Simply doubling the size of the simulation and we see the (classically) insurmountable problem: 4×10^{31}

bits of data are needed, or 5×10^{14} Summit supercomputers. A quantum computer could store this with just 100 quantum bits – qubits.

Efficient quantum simulations have the potential to aid in many practical problems including performing efficient nitrogen fixation [9], protein folding [10], and quantum chemistry [11]. On top of this, quantum computing has been shown to possess the same exponentially superior scaling for a whole range of problems including prime factoring [12], database searching [13], and machine learning [14].

The base requirements of a quantum computer are a qubit and the generation of entanglement between qubits. A qubit is a two level quantum mechanical system whose state can be initialized, controlled, and read out. Qubits have been engineered out of many different materials and systems including quantum dots in III-V material [15], nitrogen-vacancy centers in diamond [16], superconducting qubits [17], ion traps [18], photons [19], donors in insulators [20], donors in ZnO [21], and donors in silicon [22]. Entanglement between separate qubits has been seen in many systems including quantum dots [23], nitrogen-vacancy centers [24], superconducting qubits [25], ion traps [26], photons [27], and donors in silicon [28], among others.

While in theory a quantum computer might only need qubits and entanglement, in practice, to be viable as a technology much more stringent requirements are needed [29]. An arbitrary superposition of a qubit must be long lived (relative to the time it takes to perform a calculation), and initialization, control, and readout must be high fidelity to properly perform error correction [30, 31]. Finally, the system must scale efficiently. If the costs to increase the size of the quantum computer is exponential then you lose all benefit of working with a quantum computer in the first place. This is currently the most daunting problem. While entanglement can be generated between small numbers of qubits, it has not been implemented in a manner capable of being efficiently scaled up.

In parallel with quantum computing, in the encompassing field of quantum information, is quantum communication. Rather than using quantum mechanics for computational work, quantum communication uses the quantum properties for security. Due to the no-cloning theorem [32] and the monogamy of entanglement [33] information encoded via the sharing of entangled qubits can be made physically secure from unwanted eavesdropping. Whereas classical encoding schemes rely on the fact that breaking the code is computationally prohibitive, a quantum encoding scheme relies on the fact that the presence of a third party eavesdropper physically changes the exchanged qubits and is detectable [34].

As quantum communication involves the transfer of qubits over great distances, the prototypical ‘flying’ qubit is the photon. Photon based quantum communication platforms have been demonstrated over fibre-optic cables [35], to orbiting satellites [36], and short-range commercial systems are available now [37]. Despite appearing to have a lead on quantum computing, quantum communication has yet to be employed on a world wide scale.

The missing component for a large scale network is the quantum repeater [38, 39]. As photons are transferred between nodes through free space or through fibre optics the range is limited by photon loss. Unfortunately, the very same properties that make a quantum communication channel secure inhibit a simple ‘amplification’ of signal. Instead, a quantum communication channel must be extended by linking together quantum repeaters with short photonic connections between each node. A quantum repeater works by swapping entanglement between memory qubits in adjacent nodes via a photonic qubit connection. The memory resource needed has most often been proposed to be a matter qubit (although all photon quantum repeaters have been proposed [40]) meaning the same requirements for coherence lifetime, high-fidelity initialization, control, and readout along with scalable interactions are needed for a large-scale quantum communication network. Furthermore, if a matter qubit is used, a method of transferring between memory qubit and photonic, flying, qubit is needed [29].

These formidable tasks necessary for quantum computation or quantum communication mean that the particular choice of architecture – of quantum mechanical system – is extremely important. At the moment it is not clear which system will emerge as the definitive quantum computing/communication technology. Many different systems (as listed above) are being actively researched and refined to meet the strict technological requirements for a robust, high-fidelity, scalable quantum computer or quantum communication network. New proposals are continually being released, new ideas are being investigated, and new theoretical work is being done. It is a great time to be a part of, and to contribute to, the exciting work in this field.

1.2 Spin-Photon Interface

As mentioned, generating entanglement between separate qubits in a scalable manner is a remaining challenge for many qubit architectures. The difficulty stems from needing the qubits to be very isolated to have long lifetimes but still able to generate interactions to have entanglement.

Early quantum computing proposals envisioned having the entangling interaction be a wavefunction overlap that could be turned on and off with an electrostatic barrier potential. This was proposed for phosphorus donors [41] and electron quantum dots [42]. However, the precise placement needed for both the qubits and the accompanying control structure make these schemes technologically difficult.

It was realized early on that a hybrid system of both matter and photon qubits could provide a much easier pathway to scalable interactions [43, 44, 45]. Spatially separate qubits could be as isolated as possible and exchanged photons would be used to generate entanglement. A two node system of physically separated qubits, capable of generating entanglement,

is a sufficient building block for both a universal quantum computer [46] and a large scale quantum communication network [47].

What was originally thought of as an auxiliary requirement for a quantum computer, “the ability to interconvert stationary and flying qubits” [29] has become the main subject of study for many of the previously mentioned qubit systems. Many of these systems possess a ‘spin-photon’ interface which has the potential to interconvert between a spin qubit and a photon qubit.

To be a suitable candidate for a quantum computing/communication architecture the requirements of the spin-photon interface are just as strict as the requirements imposed upon the matter qubit. A suitable spin-photon interface should have a strong light-matter interaction with a high transition dipole moment. The luminescence of the system should have a high radiative efficiency and have minimal non-resonant emission, i.e., a high zero phonon line fraction. Additionally, although not required, photonic access in the telecommunication wavelength (1450-1650 nm) would be extremely useful for integration with the widespread telecommunication infrastructure already available.

1.3 Donors in Silicon

The doubling of components per integrated chip has been driven by the continual advancement and refinement in the complementary metal-oxide-semiconductor (CMOS) industry. At the heart of this industry – in addition to our computers and cell phones – is silicon. Working with the excellent scalability of a silicon based system would be invaluable in generating the large number of qubits necessary for practical quantum computation.

There is, in fact, a native silicon-based qubit that has shown a lot of promise. The spin degrees of freedom of substitutional donor impurity atoms in silicon have been studied as qubits for decades. Many different donor defects have been shown to possess extremely long lifetimes [48, 49] with phosphorus holding the record for longest lifetimes [22]. As such, phosphorus donors have been the basis of many proposed quantum computing architectures [41, 50, 51].

Exciting work has progressed in the construction and demonstration of single phosphorus donor devices [52]. Initialization, control, and readout has been demonstrated to a high enough fidelity for error correction [53]. However, a remaining difficulty is generating coupling between qubits – the final step to a scalable quantum computer. Proposed methods include using the native magnetic dipole moment [50], or intentionally perturbing the system to generate a strong electrical dipole moment to couple to a superconducting microwave cavity [51].

A promising alternative to phosphorus is the deep double donor selenium (Si:Se). Singly-ionized selenium (Si:Se⁺) has the same ground state Hamiltonian as phosphorus and has been shown to possess the same excellent coherence properties [54]. Importantly, Si:Se⁺

possesses a strong, native, electric dipole moment – an optical transition from ground state to the first excited state – at a convenient wavelength in the mid-infrared. This transition is spin selective and active in both luminescence and in absorption [55, 54] with a transition energy of 427 meV, or 2.9 μm [54].

Although this spin-photon interface does not operate in the desired telecom band, 2.9 μm light can still be confined and guided within silicon waveguides. This means that both the matter qubit and photonic qubit of a Si:Se⁺ spin-photon interface can be hosted entirely in silicon. While not at the ideal wavelength, much of the incentive to work in the telecom regime – the mature silicon photonic industry – can still be utilized at 2.9 μm .

Not only is silicon the most mature industry for electronics but also the most mature photonics platform [56]. An abundance of silicon photonics components are already accessible including waveguides [57], grating couplers [58], directional couplers [59], resonators [60], and high-efficiency single-photon detectors [61] all of which can be adapted for implementation in a Si:Se based spin-photon technology.

The spin-photon interface of the Si:Se⁺ system is thus a very promising system with which to develop into a quantum technology. Not only does selenium possess long lifetimes but it also has the advantage of possessing a fully CMOS compatible spin-photon interface with both the spins and photons hosted in silicon.

Prior to this work, the exact optical properties of the Si:Se⁺ spin-photon interface had yet to be measured precisely. Morse et al. [54] performed preliminary measurements, however, they were limited to lower bounds due to the sample used being unsuited for the measurements made. This is the focus of this work: to create appropriate Si:Se⁺ samples and perform the necessary measurements to determine the key optical parameters, namely, the transition dipole moment, the zero-phonon line fraction, and the radiative efficiency. The results will determine the feasibility of utilizing the Si:Se⁺ spin-photon interface as the base unit on the path towards integrated silicon quantum optoelectronics.

The organization of this thesis is as follows: first we will introduce the necessary background information to understand the physical system of study, Si:Se, along with the optical properties to be determined and the measurement methods employed. We will then explain the method by which we prepared our samples along with our experimental apparatus and techniques. We will present our results of the optical properties of the Si:Se spin-photon interface and conclude with an assessment of possible implementation schemes.

Concerning the key optical properties that define a spin-photon interface we measured the transition dipole moment (1.96 ± 0.08 Debye) and placed lower bounds on both the zero-phonon line fraction – the fraction of light emitted in the zero phonon line versus the phonon sideband – ($> 15.1 \pm 0.3$ %) and the radiative efficiency of all luminescence ($> 0.75 \pm 0.08$ %). In addition, we've also determined parameters that will be essential for the creation of samples and devices in future work. We have determined the integral and peak conversion factors as well as the dependence of the linewidth of the Si:Se⁺ lowest excited

state transition on the concentration of neutral impurities. We also investigated the optical properties of the neutral charge state, Si:Se^0 . For a summary of all optical parameters determined in this work, for both charge states, Si:Se^+ and Si:Se^0 , see Tab. 5.1.

Chapter 2

Background Theory

In this section we will introduce the background theory for the experimental results to follow. The discussion will start with an overview of silicon focusing, in particular, on donors in silicon and the optical properties of silicon. Next a theoretical derivation of the optical properties of a two-level system will be presented. Magnetic resonance control of spin qubits and the idea of a ‘tip-angle’ measurement for determining concentration of spin qubits will be introduced. The system of study, the selenium double donor in silicon, and its spin-photon interface will be introduced and discussed. Finally, the theory of diffusion will be presented for future discussion of sample preparation.

2.1 Properties of Bulk Silicon

Since the first silicon transistor in 1954 [62] silicon has become one of the most important elements used everyday, being omnipresent in nearly all electronic devices. Silicon is a semiconductor meaning it possesses a bandgap – a region in the electron energy-momentum phase space where no allowed energy levels exist. At zero temperature, in pure silicon, the bandgap separates the filled valence band at lower energies from the empty conduction band at higher energies (see Fig. 2.1). The separation, the bandgap energy, E_g , is 1.17 eV at 4.2 K [63]. In the valence band electrons are bound to silicon atoms, whereas in the conduction band, electrons can move freely.

Realistically, any silicon sample studied will not be pure silicon, and will contain an abundance of defects. In fact, many defects are introduced in order to create the transistors and diodes that compose modern solid state electronics [64]. In the simplest form these defects are other elements taking the place of silicon atoms in the lattice. These defects will act as ‘donors’ or ‘acceptors’ depending on whether they donate an electron or accept an electron.

A defect element from group V, with one extra valence electron compared to silicon, will have an unpaired electron when substituting a silicon atom in the lattice. This defect is thus a donor defect as it will have one additional electron bound to it. The ionization

energy of this electron, E_i , will be less than the silicon bandgap and thus will create a filled level near the conduction band. Conversely, elements from group III, with one less electron than silicon, will form acceptor defects with unfilled energy levels near the valence band. If both donor and acceptor defects are present then the low lying, empty, acceptor states will ionize the donor defects – this is known as compensation. Diagrams of these three scenarios, donor, acceptors, and compensated, are shown in Fig. 2.1.

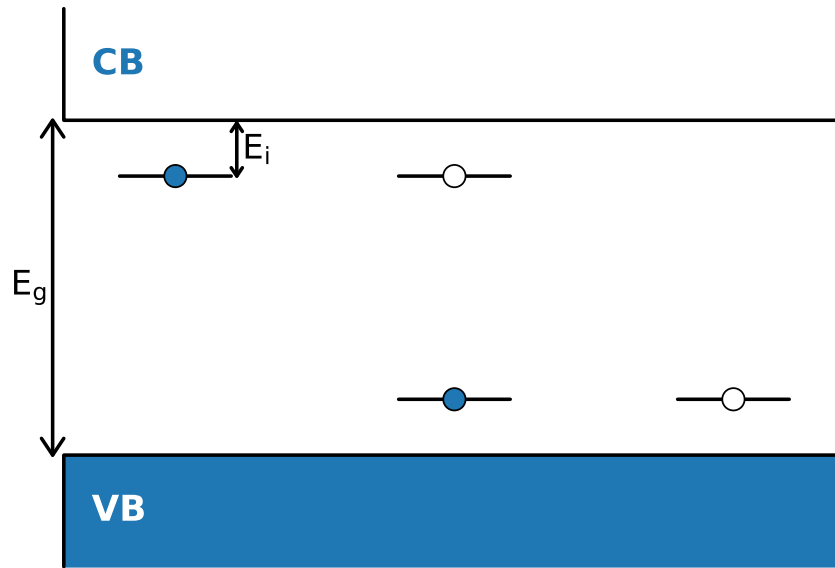


Figure 2.1: Schematic diagram showing donor (left) and acceptor (right) levels in the silicon bandgap as well as a compensated system (center) with the donor level ionized and the acceptor level filled. The conduction band (CB) and valence band (VB) are split by the energy of the bandgap, E_g . The ionization energy of the donor level, E_i , is also shown.

2.2 Silicon as an Optical Medium

Due to the bandgap, pure silicon will be transparent to light with energy less than E_g as there are no electronic transitions that can absorb the light. If the energy of the photon is greater than E_g then an electron can be excited from the valence band to the conduction band as seen in the left most transition shown in Fig. 2.2 a. From here a decay process will occur as the electron returns to the valence band. However, as silicon is an ‘indirect’ bandgap semiconductor [65] – meaning the conduction band minima and valence band maxima are not at the same momentum – the decay process must involve both an energy and a momentum transfer. As photons have insignificant momentum an entirely radiative process [66], ie only emitting a photon, is very unlikely. The dominant decay mechanism is the emission of a photon along with a momentum conserving phonon or a purely non-

radiative process through the emission of phonons [67]. Due to the indirect bandgap silicon is often considered a poor optical material in comparison to direct bandgap semiconductors such as the III-V materials [68].

When donor and acceptor impurities are added to pure silicon the possible optical transitions, both in absorption and in luminescence, become very rich. Of particular interest are those transitions made possible due to donor impurities. Donors, with their single bound electron, possess a series of excited states similar to those of hydrogen although they are modified by the silicon lattice [69]. Donors will have a ground state below the conduction band edge and a series of excited states extending to the conduction band minimum as shown in Fig. 2.2 b. The separation between ground state and conduction band is the ionization energy, E_i , analogous to the ionization energy of an atom.

This system presents a number of new optical transitions as illustrated schematically in Fig. 2.2 b. Resonant light can excite electrons from the ground state to any of the excited states (dependent on selection rules [70]). Likewise, radiative recombination from excited states back down to the ground state are possible. If the two states overlap sufficiently in k-space, then the requirement of an emitted phonon is not necessary, leading to the possibility of purely radiative emission being the dominate decay path. Furthermore, non-resonant light can excite electrons into the conduction band where the electron can decay through the excited states back to the ground state. The individual transitions can be radiative or non-radiative.

In addition to bare silicon and donor levels, there are many more absorption and photoluminescence transitions possible in silicon. Electrically neutral species can also absorb light, causing local lattice vibrations. Holes, quasiparticles due to the absence of an electron, which can be bound to acceptors at low temperatures, also possess a series of hydrogenic states extending from the acceptor level to the valence band within which optical transitions are possible.

Excitons, quasiparticles of an electron-hole pair bound together, can self-annihilate releasing light. Excitons can also bind to donor and acceptor impurities which shift the frequency of emitted light based on the defect. When bound to an acceptor/donor the electron can be scattered by the short range potential near the impurity ion, known as the central cell potential. If scattered to the Brillouin zone centre, ie to a state of zero momentum, the recombination of electron and hole can occur without emitting a phonon. This transition is known as the no-phonon line.

For an overview of these optical transitions, see Pajot [70] for hydrogenic systems and Davies [71] for photoluminescence transitions. In this work we will investigate optical transitions in all of the above varieties.

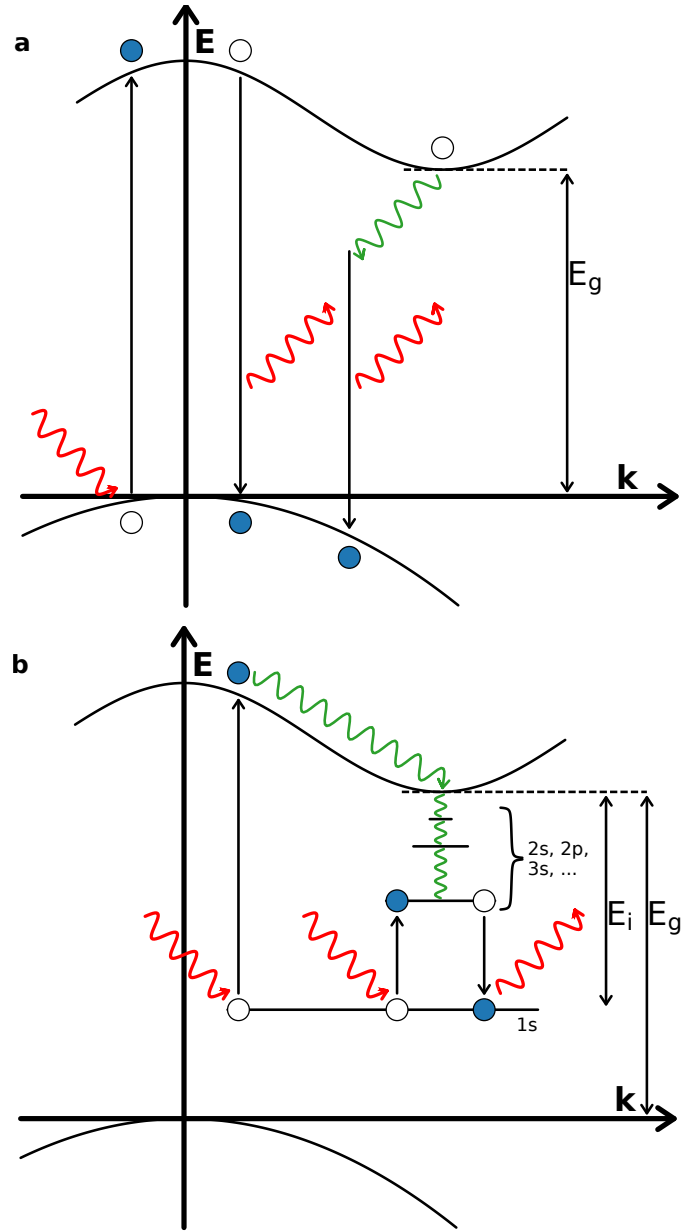


Figure 2.2: Schematic diagram showing the energy-momentum phase space of the indirect silicon bandgap. Optical transitions in silicon without donors (a) and with a donor level present (b) are shown. Red arrows represent an absorbed or emitted photon, green arrows represent emitted phonons, and black arrows represent the energy change of electrons (blue circles) and holes (white circles) due to absorption/emission of photons/phonons. a) From left to right the transitions are: above bandgap light is absorbed; a photon is emitted without a phonon; a photon is emitted with a momentum conserving phonon. b) From left to right the transitions are: non-resonant light ionizing a donor and subsequent phonon cascade back to an excited state; resonant light exciting a transition from the ground state to an excited state; emission of resonant light as an electron decays from an excited state to the ground state.

2.3 Optical Properties

With such an abundance of optical processes available in silicon we will take the time now to define the important optical properties that determine the optical responses: μ , the transition dipole moment, a measure of the strength of the light-matter interaction, and τ , the radiative lifetime, a measure of the rate of photon emission. Furthermore, we will relate these properties to quantities measurable in experiment.

We will restrict this theoretical discussion to a 2 level optical system, for instance, an atom with ground and excited state electronic levels. All of the following will be directly applicable to optical transitions in silicon. In particular, the electronic levels of a donor in silicon can be viewed as similar to those of an isolated atom.

This discussion follows the derivation presented by Hilborn [72]. Our discussion begins with the Einstein coefficients which describe the spontaneous emission and induced absorption and emission of a 2 level optical system. Consider a system with an upper level, 2, and a lower level, 1, with N_2 atoms in the upper level and N_1 atoms in the lower level. The A coefficient is defined by the rate of spontaneous emission, W_{21}^s , as:

$$W_{21}^s = A_{21}N_1. \quad (2.1)$$

If level 1 is the only lower level that level 2 can decay to, then A_{21} is simply $1/\tau$ where τ is the radiative lifetime of level 2.

The B coefficients are defined by the rates of induced absorption, W_{12}^i , and induced emission, W_{21}^i , as:

$$\begin{aligned} W_{12}^i &= B_{12}pN_1, \\ W_{21}^i &= B_{21}pN_2. \end{aligned} \quad (2.2)$$

where p is the energy density per unit angular frequency.

These A and B coefficients are related as

$$\begin{aligned} B_{21} &= \frac{\pi^2 c^3}{\hbar \omega_{21}^3} A_{21} \\ B_{21} &= \frac{g_1}{g_2} B_{12} \end{aligned} \quad (2.3)$$

where c is the speed of light, \hbar is the reduced Planck's constant, ω_{21} is the resonant angular frequency of the $2 \leftrightarrow 1$ transition, and g_1 and g_2 are the degeneracy factors of levels 1 and 2 respectively.

From a full quantum electrodynamics treatment of spontaneous emission it can be shown that [73, 74]

$$A_{21} = \frac{1}{\tau} = \frac{2\omega_{21}^3 e^2}{3\epsilon_0 \hbar c^3} |\langle 1 | \mathbf{r} | 2 \rangle|^2, \quad (2.4)$$

where ϵ_0 is the permittivity of free space, and \mathbf{r} is the position operator.

The transition dipole moment μ_{21} is defined by

$$\mu_{21}^2 \equiv e^2 |\langle 1 | \mathbf{r} | 2 \rangle|^2. \quad (2.5)$$

This value represents the strength of the transition from level 1 to 2. A higher value indicates higher probability of the transition occurring when the system is illuminated with resonant light. A value of zero would indicate the transition is not dipole allowed and likewise there being no radiative decay path available, $\tau \Rightarrow \infty$.

We would now like to relate these quantities to a measurement that can be made on a sample. We will find that we can relate the radiative lifetime (and thus the transition dipole moment) to the absorption coefficient of a sample. The absorption coefficient, $\alpha(\omega)$, with units of inverse length is the penetration depth into a sample of light at frequency ω . In the most general form:

$$I(\omega, x) = I_0 e^{-\alpha(\omega)x} \quad (2.6)$$

where $I(\omega, x)$ is the intensity of light of frequency ω at a distance x into the sample. By ‘sample’ we mean any collection of 2 level optical centers, this may be atoms in a gas cell or donor impurities in a piece of silicon.

The absorption coefficient is, in general, dependent on the frequency of light. Additionally, if the distribution of centers is not uniform in the sample, α can depend on the depth into the sample. In this case the intensity after some small length Δx is approximately (dropping the explicit frequency dependence for clarity)

$$I(\Delta x) = I(0) e^{-\alpha(\Delta x)\Delta x} \quad (2.7)$$

Moving another Δx into the sample:

$$I(2\Delta x) = I(\Delta x) e^{-\alpha(2\Delta x)\Delta x} \quad (2.8)$$

Thus an arbitrary distance, $x = N\Delta x$, into the sample, the intensity will be:

$$I(x = N\Delta x) = \prod_{i=1}^N I(i\Delta x) \quad (2.9)$$

$$I(i\Delta x) = I((i-1)\Delta x) e^{-\alpha(i\Delta x)\Delta x}$$

In the limit $\Delta x \Rightarrow 0$, $N \Rightarrow \infty$, we obtain

$$I(x) = I(0) e^{-\int_0^x \alpha(x') dx'} \quad (2.10)$$

$$I(x) = I(0) e^{-\bar{\alpha}x}$$

where $\bar{\alpha}$ is the average absorption coefficient over the length of sample measured.

We can determine the absorption coefficient (or likewise the average absorption coefficient) by measuring the intensity of light after passing through a sample of a known length ($I(x = L_{\text{sample}}, \omega)$) and by measuring the intensity of light before entering the sample (I_0). In practice one measures the intensity of light with and without the sample in the path of the light.

We will now show the relation between the average absorption coefficient and the optical properties defined, μ_{21} and τ . Consider a sample populated with 2 level optical centers. Suppose each individual center has a frequency response to light given by $g(\omega)$. In general $g(\omega)$ will be a sharply peaked lineshape to which we will impose the normalization

$$\int_{-\infty}^{\infty} g(\omega) d\omega = 1, \quad (2.11)$$

where the negative lower bound is for ease of calculation.

Suppose a beam of light impinges upon the sample, the power lost as the beam propagates into the sample will be

$$-dP(\omega) = \hbar\omega W_{12}^i g(\omega) = \hbar\omega B_{12} p N_1 g(\omega). \quad (2.12)$$

Suppose the beam of light has an area, A , then the total number of centers in level 1 in a slice, dx , is $N_1 = n_1(x) A dx$ where $n_1(x)$ is the number of centers in level 1 per volume a distance x into the sample ($n_1(x)$ is assumed to be constant in the transverse direction). Plugging this into Eqn. 2.12 we have

$$-dP(\omega, x) = \hbar\omega B_{12} p n_1(x) A g(\omega) dx. \quad (2.13)$$

Using the fact that $I = P/A$ and $I = cp$ we have

$$\frac{-1}{I(\omega, x)} \frac{dI(\omega, x)}{dx} = \hbar\omega B_{12} n_1(x) g(\omega) / c \quad (2.14)$$

By differentiating Eqn. 2.6 it becomes clear that the left hand side of Eqn. 2.14 is equal to the absorption coefficient $\alpha(\omega, x)$. Thus we have

$$\alpha(\omega, x) = \hbar\omega B_{12} n_1(x) g(\omega) / c. \quad (2.15)$$

Integrating over the sample length, L ,

$$\bar{\alpha}(\omega) = \hbar\omega B_{12} \bar{n}_1 g(\omega) / c, \quad (2.16)$$

and over all frequencies,

$$\int \bar{\alpha}(\omega) d\omega = \hbar\omega_{21}B_{12}\bar{n}_1/c, \quad (2.17)$$

where we have assumed that $g(\omega)$ is sharply peaked and thus we can replace ω by the resonant frequency ω_{21} .

Along with Eqn. 2.2 we now have both the radiative lifetime and transition dipole moment defined in terms of a measurable quantity: the absorption coefficient area. In practice we will assume that $\bar{\alpha}(\omega)$ goes to zero sufficiently far from ω_{21} and integrate the spectra only in a region about the transition of interest. The final expressions for radiative lifetime and transition dipole moment are summarized below.

A final property of interest is the idea of an area or integral conversion factor, f . From Eqn. 2.17 the absorption coefficient area is proportional to the average concentration of electrons in level 1. A sufficiently cold sample, in thermal equilibrium, will have all electrons in the ground state in which case \bar{n}_1 is the average concentration of optically active centers in the sample, \bar{n}_i (along the light beam's path). Thus a conversion factor

$$f_i \equiv \frac{\bar{n}_i}{\int \bar{\alpha}(\nu) d\nu} \quad (2.18)$$

is of great use as it allows an absorption spectrum to provide a measure of the concentration of an impurity of interest.

Furthermore, a conversion factor can be defined based on the peak absorption coefficient, $\bar{\alpha}(\omega_{\max})$, as

$$k_i \equiv \frac{\bar{n}_i}{\bar{\alpha}(\omega_{\max})}. \quad (2.19)$$

However, the peak absorption coefficient will depend on the exact conditions of the sample. The temperature, strain, and isotopic composition can all change $\bar{\alpha}(\omega_{\max})$ whereas the total area will remain unchanged (see Sec. 2.3.1).

In the final equations below we make the assumption that the concentration of electrons in the ground state is equal to the concentration of centers, $\bar{n}_1 = \bar{n}_i$. Additionally, we must account for the fact that the centers in the sample can equivalently be donors in a semiconductor, or any other collection of two level optical systems embedded in a given medium. In doing so we must account for the difference in the refractive index, n , of the medium containing the centers, $c \Rightarrow c/n$. Likewise, $\epsilon_0 \Rightarrow \epsilon_0\epsilon_r$ where ϵ_r is the relative permittivity of the material.

The final formula for the transition dipole moment, radiative lifetime, integral conversion factor, and peak conversion factor are listed below:

$$\begin{aligned}
\tau &= \frac{g_2 \pi^2 c^2 \bar{n}_i}{g_1 n^2 \omega_{21}^2 \int \bar{\alpha} d\omega} \\
\mu_{21} &= \sqrt{\frac{1}{\tau} \frac{3\epsilon h c^3}{2\omega_{21}^3 n^3}} \\
f_i &= \frac{\bar{n}_i}{\int \bar{\alpha} d\omega} \\
k_i &= \frac{\bar{n}_i}{\bar{\alpha}(\omega_{\max})}
\end{aligned} \tag{2.20}$$

2.3.1 Broadening Mechanisms

The term ‘bulk’ measurement is used to describe measurements – like that defined above – involving a macroscopic sample with many centers distributed throughout, in contrast to measurements on a single center. In any macroscopic sample each center will have a frequency response, $g(\omega)$, with the same linewidth, but the peak frequency can be shifted depending on the local environment. Factors such as strain in the crystal lattice [75], electric fields [76], and the isotopic composition of the center and the surrounding lattice [77] can all cause shifts in each center’s spectral response.

A bulk measurement of absorption or photoluminescence will be the sum of all these different spectral responses, all at slightly different peak positions. The result is a spectrum much broader than any individual center’s linewidth. This is known as inhomogeneous broadening, as it is due to inhomogeneities in the local environment about each center.

An important note is that while these effects cause broadening, the total area of the spectrum, $\bar{\alpha}(\omega)$, will not change. Although shifted, each center has the same frequency response lineshape satisfying $\int g(\omega) d\omega = 1$. This is why the integral conversion factor, f_i , is valid for any sample, whereas the peak conversion factor, k_i , depends on the exact conditions of the sample.

A particularly important inhomogeneous broadening mechanism is that due to the isotopes of the host lattice [77]. Silicon has three stable isotopes ^{28}Si , $\sim 92.2\%$; ^{29}Si , $\sim 4.7\%$; and ^{30}Si , $\sim 3.1\%$ [77] all of which are present in natural silicon. The bandgap, dielectric constant, and effective mass of donor bound electrons all change with the average mass of the surrounding lattice. This leads to shifts in transition energies due to the statistical fluctuations of the isotopes around an impurity. By working with isotopically purified ^{28}Si , optical transitions can become extremely sharp making resolvable fine structure that would otherwise be obscured [78, 79, 80, 55].

Suppose all inhomogeneous broadening mechanisms could be removed from a sample and the intrinsic response of the center, $g(\omega)$, could be studied. The spectrum would still have a linewidth associated with it, known as the homogenous linewidth. This intrinsic

linewidth is due to the fact that the excited lifetime is finite and thus there is quantum mechanical uncertainty of the transition energy:

$$\Delta E \Delta t \approx \hbar. \quad (2.21)$$

Thus, a photon will be absorbed or emitted in the frequency range

$$\Delta\omega = \frac{\Delta E}{\hbar} \approx \frac{1}{\Delta t}. \quad (2.22)$$

Setting Δt to the excited state lifetime, τ_{exc} , $\Delta\omega$ is the homogeneous linewidth of the transition [70]. This homogeneous linewidth is also known as the lifetime-limited linewidth.

In a two-level system the time to leave the excited state is trivially equal to the time to return to the ground state. However, in more complicated systems transitions from the excited state to states other than the ground state are also possible. For instance, transitions to an energy level above the first excited state can be thermally activated. This means the time to leave the excited state is, in general, lower than the time to return to the ground state.

We will define the time to return to the ground state as, τ_{exc} and refer to it simply as the excited state lifetime but must note that using the homogeneous linewidth to determine τ_{exc} can only give a lower bound:

$$\tau_{\text{exc}} > \frac{1}{\Delta\omega_{\text{hom}}}. \quad (2.23)$$

If the excited state only decays radiatively then $\tau_{\text{exc}} = \tau$. However, in general, non-radiative processes can occur in a physical medium, such as through phonon emission as discussed in Sec. 2.1 or Auger recombination in the case of excitons bound to donors or acceptors [81]. We can define the radiative efficiency as the ratio τ_{exc}/τ . This gives the ratio of radiative recombination to non-radiative recombination. A value of 1 indicates only radiative decays occur in transitioning from level 2 to 1.

The final property to define is the idea of zero phonon line (ZPL) fraction. While a transition could be purely radiative, involving the emission of a single photon, there is the possibility that the decays involve the emission of a phonon and a lower energy photon. In general a photoluminescence spectrum will have a ZPL line at the resonant frequency as well as a phonon sideband of lower energy photons emitted along with one or more phonons to conserve energy. The ratio of the area of the ZPL line to the area of all emission is the ZPL fraction.

2.3.2 Hole Burning

With the abundance of inhomogeneous broadening mechanisms it is very hard to create a sample for which a spectral feature is at the lifetime-limited, homogeneous, linewidth in

silicon. However, with the aid of a laser to perform ‘hole burning’ the homogenous linewidth can be observed in an absorption spectrum.

Imagine a narrow linewidth laser (much less than the homogeneous linewidth) tuned to the center frequency of an inhomogeneously broadened transition exciting some electrons to the excited state. Suppose we could perform an absorption measurement before the electrons return back to the ground state, what would the spectrum look like? The laser would only be able to strongly excite those centers within one homogeneous linewidth of the applied laser frequency. Centers with transition frequencies shifted outside of this range by inhomogenous broadening mechanisms will not be strongly excited. This leads to a ‘hole’ being ‘burned’ into the spectral line. A schematic diagram of this is shown in Fig. 2.3.

The size of the hole burned will depend on the homogeneous linewidth, a narrower linewidth will lead to a narrower hole, and on the power of the pumping laser. Low power will only marginally pump those transitions with small overlap with the laser frequency, while high power will pump these transitions more. The hole linewidth is given by [82]:

$$\Delta\omega_{\text{hole}} = \Delta\omega_{\text{hom}}[1 + \sqrt{1 + I/I_{\text{sat}}}] \quad (2.24)$$

Where $\Delta\omega_{\text{hole}}$ is the linewidth of the hole, $\Delta\omega_{\text{hom}}$ is the homogeneous linewidth of the center, I is the laser power, and I_{sat} is the power needed to ‘saturate’ the transition. A transition is said to be saturated when difference in populations $\Delta N = N_1 - N_2$ drops to half of the thermal equilibrium difference.

If the inhomogeneities leading to the inhomogeneous broadening are not static there can also be centers that are shifted in energy so that their linewidth come in and out of overlap with the laser on the time scale of the hole burning measurement. The net effect is the hole burned will be larger than if the inhomogeneities were all static. Thus, for sufficiently low pump power, the linewidth of the hole burnt will have a lower bound of twice the homogeneous linewidth:

$$\Delta\omega_{\text{hole}} > 2\Delta\omega_{\text{hom}} \quad (2.25)$$

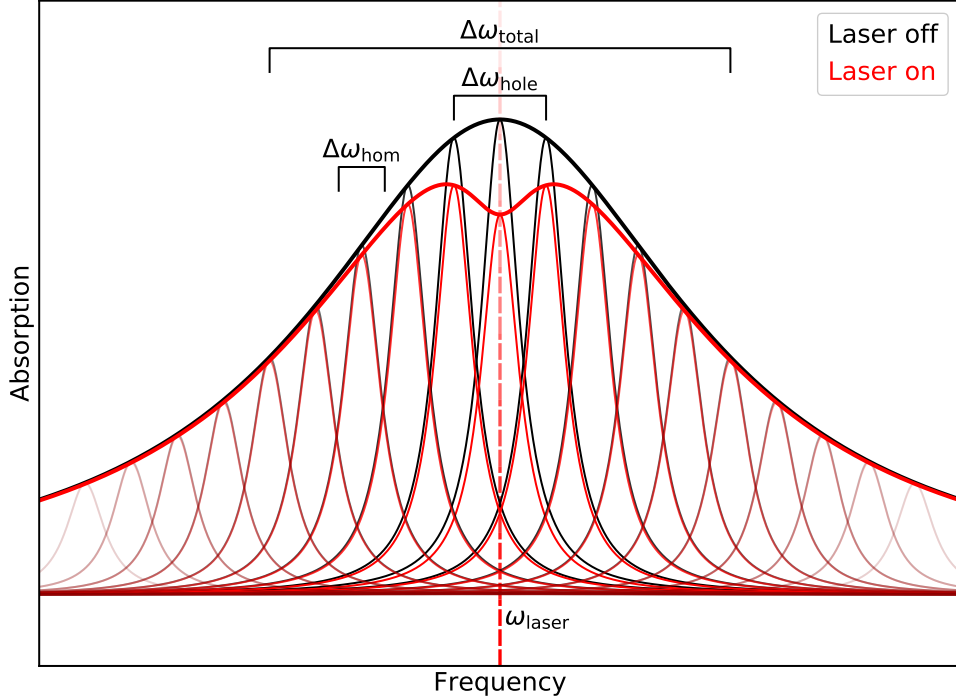


Figure 2.3: Schematic diagram illustrating the effect of spectral hole burning from a laser tuned to the peak of an inhomogeneously broadened spectral line. The total linewidth, $\Delta\omega_{\text{total}}$, is due to many shifted transitions, each with a homogeneous linewidth, $\Delta\omega_{\text{hom}}$. The laser, tuned to the peak of the spectra (red dashed line, ω_{laser}), burns a hole of linewidth $\Delta\omega_{\text{hole}} = 2\Delta\omega_{\text{hom}}$.

2.4 Magnetic Resonance

In addition to introducing a myriad of optical transitions in silicon, donor defects can also display magnetic resonance (MR) transitions, observable via the application of radio-frequency (RF) magnetic fields [83]. These transitions may be between the spins states of an electron, the spins states of the nucleus, or even between superposition states of the two spins. As these spin states (or superposition states) define the qubit of study for donor impurities the application of RF magnetic fields is the manner in which donor impurity qubits are controlled.

As we will see, the control and manipulation of donor spins can be used to determine the concentration donor spins in a sample via a ‘tip-angle’ measurement. As seen in Eqn. 2.20 the concentration of optical active centers is an important quantity for determining the optical properties.

The two states of the donor spin qubit can be mapped onto a Bloch sphere with one eigenstate, termed $|0\rangle$, at the north pole and one eigenstate, termed $|1\rangle$, at the south pole. Any superposition of these two states, $|\Psi\rangle$, defined as

$$|\Psi\rangle = \cos \frac{\theta}{2} |0\rangle + e^{i\phi} \sin \frac{\theta}{2} |1\rangle \quad (2.26)$$

can be mapped to the sphere as the unit vector

$$\vec{a} = (\sin \theta \cos \phi, \sin \theta \sin \phi, \cos \theta) \quad (2.27)$$

where $0 \leq \theta \leq \pi$ and $0 \leq \phi \leq 2\pi$. In general, a pair of eigenstates described in this manner, and used as a qubit is simply called a ‘spin’ as the system can be mapped directly to a spin-1/2 particle. The two states, $|0\rangle$ and $|1\rangle$, are also equivalently called ‘spin up’ and ‘spin down’.

In a bulk sample with many spins a Bloch sphere representation can illustrate the average state of all the spins. In this case the vector representing the system need not be a unit vector and can lie below the surface of the Bloch sphere. Examples of Bloch sphere representations are shown in Fig. 2.4

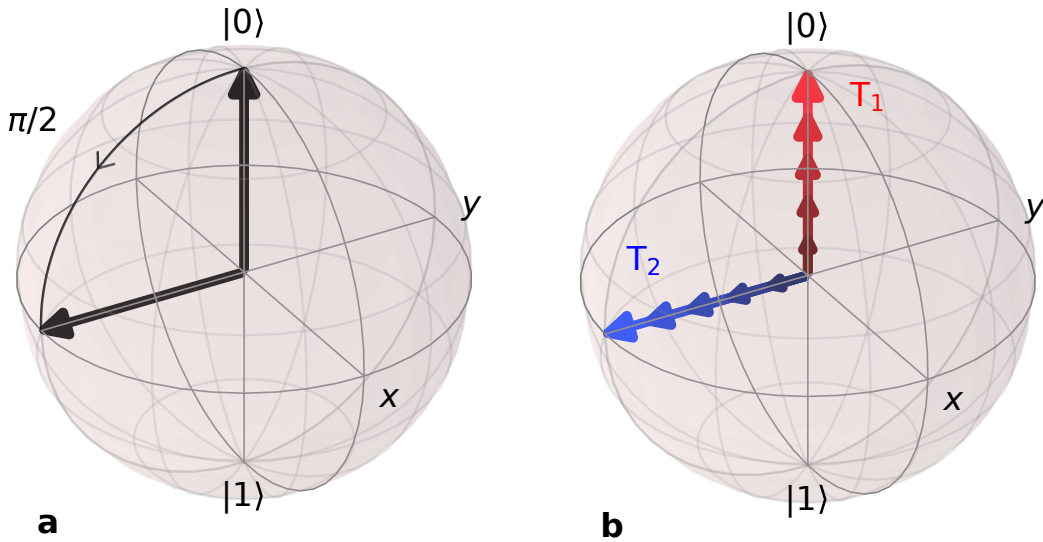


Figure 2.4: Bloch diagrams showing a) a $\pi/2$ rotation about the x -axis and b) T_1 and T_2 decay processes. See text for details.

By applying RF magnetic fields transverse to the quantization axis (z -axis) at a frequency equal to the transition frequency between the two spin states the state on the Bloch sphere will rotate (see Fig. 2.4 a). The phase of the oscillating RF field determines the axis about which the spins will rotate (this phase is usually defined relative to the first application of the RF field with 0° being the x -axis). This control allows a collection of spins to be

rotated to arbitrary superposition states and introduces the idea of an RF pulse sequence. By first initializing all spins to an eigenstate ($|0\rangle$ or $|1\rangle$) specific durations of RF pulses in specific combinations allow for the measurement of the quantum properties of the ensemble of spins upon readout of the final state of the spin ensemble.

The exact methods by which a ensemble of spins are initialized and read out are system dependent. In general, initialization places all spins into a known eigenstate and readout involves the measurement of a signal proportional to the projection of the spins onto a known eigenstate.

Two important properties to be measured are the T_1 and T_2 lifetimes. Depending on the temperature and the energy splitting of the spin states the thermal equilibrium of a collection of spins will be some distribution of spin up and spin down. By initializing (and possibly rotating) the spins can be brought out of thermal equilibrium. T_1 is the time constant associated with the exponential decay back to thermal equilibrium. This is shown schematically in Fig. 2.4 b showing a decay to a thermal equilibrium state of 50/50 spin up/spin down. The average state (represented by the red vector) decays from a highly polarized state (bright red) to an unpolarized state (dark red). As a T_1 decay is associated with changes in the population of a state (the diagonal terms of the density matrix) it is also known as the population lifetime.

A T_2 decay, on the other hand, is concerned with changes in the coherence of a system (the off-diagonal terms of the density matrix). After initializing a system, the spins can be placed into a superposition state by a $\pi/2$ RF pulse. T_2 is the time constant associated with the exponential decay of the *transverse* polarization. This is shown schematically in Fig. 2.4 b showing the average state (represented by the blue vector) decaying from a state with a large transverse polarization (bright blue) to a state with no net transverse polarization (dark blue). As a T_2 decay is associated with the changes in the coherence of the state it is also known as the coherence lifetime.

Another important decay rate is the dephasing time constant, T_2^* . Just as there are optical broadening effects due to inhomogeneity in a sample, static inhomogeneities in a sample will lead to a rapid decay of transverse polarization. When rotated to a superposition state on the equator of the Bloch sphere the spins will precess about the z-axis with a frequency determined by the energy difference between the two spin states. If all spins have the same energy difference then in the rotating reference frame all spins will overlap. However, inhomogeneities in the sample lead to different energy differences and thus different oscillation frequencies. In the rotating reference frame the result is individual spins accumulate phase relative to the average and the individual spins spread out. The average transverse polarization decays away with a time constant, T_2^* , the dephasing time constant.

As superposition states are the fundamental resource manipulated in a quantum algorithm, a long T_2 is needed to ensure an algorithm can be completed before a state decays away. T_2 is limited by T_1 as $T_2 \leq 2T_1$ [83], thus a long T_1 is needed as well. While a T_1

measurement can be performed using only initialization and readout, a T_2 measurement requires RF pulse sequences.

The first pulse sequence of note is the Rabi pulse sequence. The angle of rotation of an RF pulse of a given length depends on the power of the pulse. In an experiment the power applied to the spins is not easy to determine as all sources of attenuation must be accounted for between RF source and the sample. A Rabi pulse sequence (shown in Fig. 2.5 a) allows one to determine the conversion from RF pulse length to rotation angle. By continually increasing the length, t , of the applied pulse, the spins are rotated more and more about the Bloch sphere (about the x -axis). The readout signal will then be sinusoidal, oscillating at a frequency proportional to the applied RF power. By performing a Rabi pulse sequence the pulse length needed to rotate by any angle can be determined.

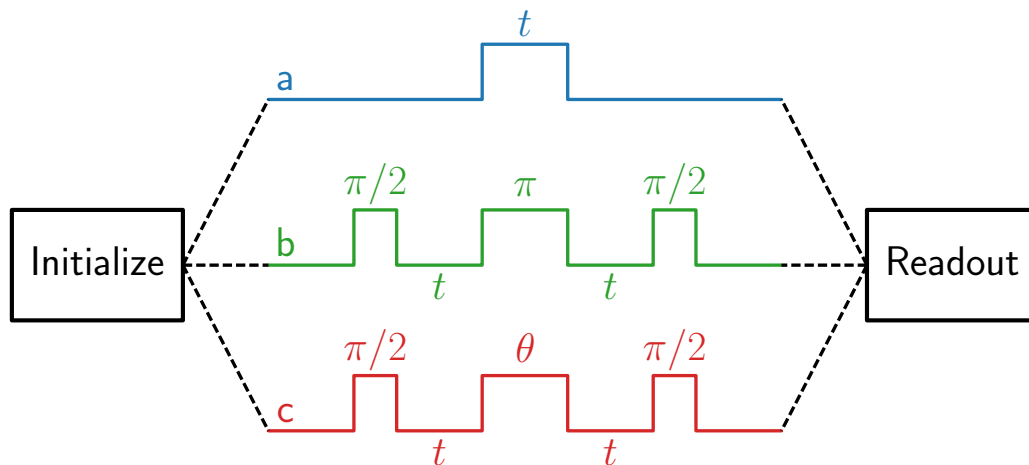


Figure 2.5: RF pulse sequences used in this work. (a) Rabi pulse sequence. (b) Hahn-echo pulse sequence. (c) Tip-angle pulse sequence for arbitrary refocusing pulse angle, θ .

The next pulse sequence of note is the Hahn echo pulse sequence [84]. This pulse sequence, shown in Fig. 2.5 b, allows for a measurement of the T_2 coherence time of a qubit system. Specifically, this is the Hahn echo T_2 as there exist other RF pulse sequence that can be used to determine a coherence lifetime, such as the XYXY pulse sequence [85]. The initial pulse rotates the spins into the x-y plane of the Bloch sphere where the spins undergo oscillations about the z-axis at a frequency given by the energy difference between spin up and spin down. Due to static inhomogeneities in the sample the spins will start to dephase with a time constant T_2^* . Specifically, over the span of the first free evolution time, t , the average transverse polarization will have rotated $\omega_{ave}t$, where ω_{ave} is the average transition frequency. Each spin with a transition energy, ω_i , will have acquired a phase relative to the average, $\Delta\phi_i = (\omega_i - \omega_{ave})t$.

To account for this acquired phase, a ‘refocusing’ π pulse is applied to rotate the spins 180° about the x -axis. This shifts the acquired phase, $\Delta\phi_i \Rightarrow \pi - \Delta\phi_i$. During the next free evolution time, t , the spins will again acquire the phase $\Delta\phi_i = (\omega_i - \omega_{\text{ave}})t$ which results in all spins have accumulated the same phase, π . The final pulse rotates the spins back to the z -axis (ie. into an eigenstate) to be ready for readout (this step isn’t always needed, it depends on the readout method). This pulse sequence cancels out static inhomogeneities allowing for a measure of the Hahn-echo T_2 by varying the evolution time, $2t$.

2.4.1 Instantaneous Diffusion and Tip-Angle

When working with a bulk sample with a high concentration of spins, the interactions between spins often cannot be neglected. Dipolar interactions between spins lead to direct and indirect spin ‘flip-flops’ which cause decoherence [86]. While a Hahn echo can cancel out static inhomogeneities present in the environment, if the source of decoherence is due to the spins themselves then this cannot be corrected by a Hahn echo because the refocusing pulse makes the spins non-static. During the refocusing pulse of a Hahn echo pulse sequence the flipping of the spins is equivalent to flipping many magnetic dipole moments, this leads to a change of the local magnetic field at each spin. As the arrangement of spins is random so too are the local field changes. As such the Hahn echo introduces a non-static inhomogeneity in magnetic field which leads to decoherence. This is known as instantaneous diffusion of magnetization in the spectral dimension [86, 87].

The rate of decoherence will depend on a number of factors: the concentration of spins in the bulk sample, n_i , as fewer spins leads to greater isolation from the changes in magnetic field. It depends on the sensitivity of the transition energy to changes in magnetic field, $\partial\nu/\partial B$. And it depends on the angle of the refocusing pulse, θ . As the rotation angle goes to zero the pulse sequence become equivalent to flipping only a single spin. In this low pulse angle regime all other spins appear static and thus their decoherence effects are canceled out when measuring the T_2 lifetime of the single test spin.

The effects of instantaneous diffusion can be mapped out using ‘tip-angle’ pulse sequences (see Fig. 2.5 c). These sequences are equivalent to the Hahn echo pulse sequence with the π pulse replaced by a rotation by θ . The measured coherence time for a tip-angle sequence of angle θ , $T_{2,\theta}$ will be [86]

$$\frac{1}{T_{2,\theta}} = \frac{1}{T_{2,\text{Int}}} + n_i \left(2\pi \frac{\partial\nu}{\partial B} \right)^2 \frac{\pi}{9\sqrt{3}} \mu_0 \hbar \sin^2 \frac{\theta}{2} \quad (2.28)$$

where μ_0 is the permeability of free space and $T_{2,\text{Int}}$ is the intrinsic Hahn echo T_2 in the limit of zero instantaneous diffusion, ie, a single isolated spin.

Measuring $T_{2,\theta}$ not only allows a measure of the intrinsic Hahn echo T_2 , but it also allows a measure of the average concentration of spins, \bar{n}_i . In practice measurements at low

refocusing pulse angles become unfeasible as less spins are refocused for the final readout resulting in less signal.

2.5 Selenium Donors

While donor defects in silicon provide possibilities for optical transitions, the example used, group V donors, have optical transitions in the technically challenging Terahertz regime. This is due to the group V donors being ‘shallow’, so called due to their small ionization energy (E_i in Fig. 2.2). Phosphorus, for example, has a binding energy of 45.6 meV [70] and thus any excited state transitions must be lower than this energy.

Group VI atomic defects, on the other hand, possess much larger binding energies. As these elements have two additional valence electrons, and two additional nuclear charges (unshielded by the core electrons) these defects act as helium atoms rather than hydrogen atoms in silicon [88]. Furthermore, even when one of the electrons is ionized these elements still act as a donor due to possessing two unpaired electrons [88]. For this reason group VI donors are referred to as deep double donors.

The binding energies for the two charge states of selenium are 307 meV [70] for the neutral state, Se^0 , and 593 meV [70] for the singly-ionized state, Se^+ . Both charge states exhibit a series of hydrogenic states extending to the conduction band, just like the shallow donors [89, 90]. However, due to the larger ground state binding energies, transitions from the ground state to the excited states are in the mid-infrared (MIR) regime ($\lambda = 2.5 - 25 \mu\text{m}$). This is much more accessible than the Terahertz regime of shallow donors allowing for an optical probe of the ground state.

Both charge states possess a ground state with a 1s manifold which is split into six sublevels due to the sixfold valley degeneracy of the silicon conduction band [69]. These sublevels are split by valley-orbit terms to a singlet, 1s:A, a triplet, 1s:T₂, and a doublet, 1s:E [89]. These energy levels for both Se^0 and Se^+ are shown in Fig. 2.6 a and b.

Including the spin of the electron these levels experience yet more splittings. Due to an exchange interaction between the two electrons of the neutral species the 1s:T₂ state splits to a spin singlet, 1s:T₂, and a spin triplet 1s:³T₂ [91, 70], this is shown in Fig. 2.6 a. Concerning the singly-ionized charge state: a spin-valley interaction splits the 1s:T₂ state into a singlet, 1s:T₂Γ₇, and a doublet, 1s:T₂Γ₈ [89], this is shown in Fig. 2.6 b.

Of particular interest is the spin-1/2 isotope, ⁷⁷Se. The singly-ionized charge state ⁷⁷Se⁺ possess the same (up to factors) ground state Hamiltonian as ³¹P [54]

$$\mathcal{H} = \frac{g_e \mu_B}{h} B_0 S_z - \frac{g_n \mu_N}{h} B_0 I_z + A \vec{S} \cdot \vec{I} \quad (2.29)$$

Where A , the hyperfine constant, g_e and g_n , the electronic and nuclear g-factors are specific to the particular system. μ_B and μ_N are the Bohr and nuclear magneton, respectively, h is the Planck constant, S and I are the electron and nucleus Pauli spin operators, and

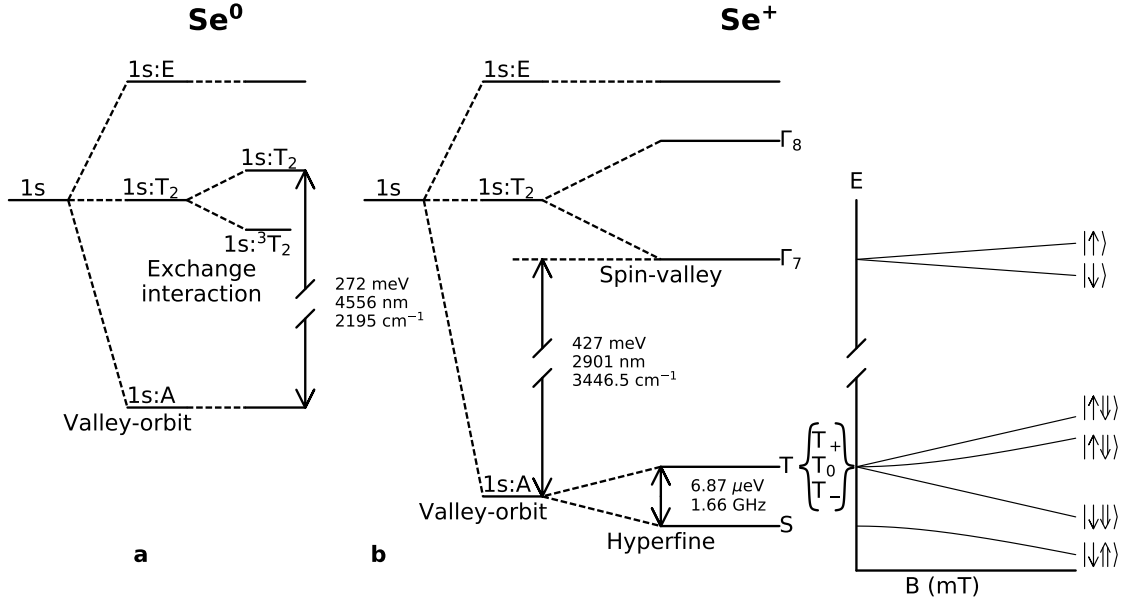


Figure 2.6: Si:⁷⁷Se energy level diagram. (a) The energy levels of the neutral charge state, Se⁰. Valley-orbit interactions split the 1s state into 1s:A, 1s:T₂, and 1s:E. The 1s:T₂ state is further split into a spin singlet and spin triplet due to an exchange interaction with the second bound electron. (b) The energy levels of the singly-ionized charge state, Se⁺. Valley-orbit interactions split the 1s state into 1s:A, 1s:T₂, and 1s:E. Spin-valley interactions split the 1s:T₂ level into Γ₇ and Γ₈. Electron-nucleus hyperfine interaction splits the 1s:A level into singlet, S, and triplet, T states. (c) Under the effects of a magnetic field Γ₇ splits with (anti-) alignment with the magnetic field. The singlet and triplet states also split with magnetic field. At high magnetic field the states can be described by the electron and nuclear spins, single and double arrow respectively. The energies of the relevant transitions for this thesis work have been indicated.

B_0 is the magnetic field. $^{77}\text{Se}^+$ possesses a hyperfine constant, $A = 1.66$ GHz [55, 54] and g-factors, $g_e = 2.0057$, and $g_n = 1.07$ [55].

At zero field, the hyperfine coupling between the electron and nuclear spin splits the $1s:A$ state into a singlet, S, and a triplet T (T_-, T_0, T_+). These energy levels are shown in Fig. 2.6 c. $1s:T_2\Gamma_7$, $1s:A:S$, and $1s:A:T$ have a Zeeman interaction changing their energy in the presence of a magnetic field. This is shown schematically in Fig. 2.6 c (exact energies are solutions to the Breit-Rabi formula [92]).

By working with sufficiently purified silicon-28 the individual transitions $1s:A:T \Leftrightarrow 1s:T_2\Gamma_7$ and $1s:A:S \Leftrightarrow 1s:T_2\Gamma_7$ become resolvable (see Fig. 2.7) [55, 54]. These two transitions comprise a lambda transition as shown in the inset of Fig. 2.7.

This arrangement allows population to be hyperpolarized between the two states via optical pumping. By tuning a laser to the $T \Rightarrow \Gamma_7$ transition electrons in the T state will be excited to Γ_7 . From here the electrons can decay to either S or T, however, if they decay to the T state, the laser will excite them back to the excited state. The net effect is the electrons are ‘pumped’ into the S state. The S state is said to be hyperpolarized as its population is much higher than the thermal equilibrium population. The T state can likewise be hyperpolarized by tuning the laser to the $S \Rightarrow \Gamma_7$ transition.

Morse et al. studied the qubit composed of the $S \Leftrightarrow T_0$ transition at Earth’s field using this hyperpolarization scheme to initialize the selenium centers in a bulk sample and RF magnetic field to rotate about the Bloch sphere defined by S and T_0 . They measured a very long Hahn echo T_2 of 2 seconds [54], and recent work has measured a 4 hour T_1 population lifetime [93].

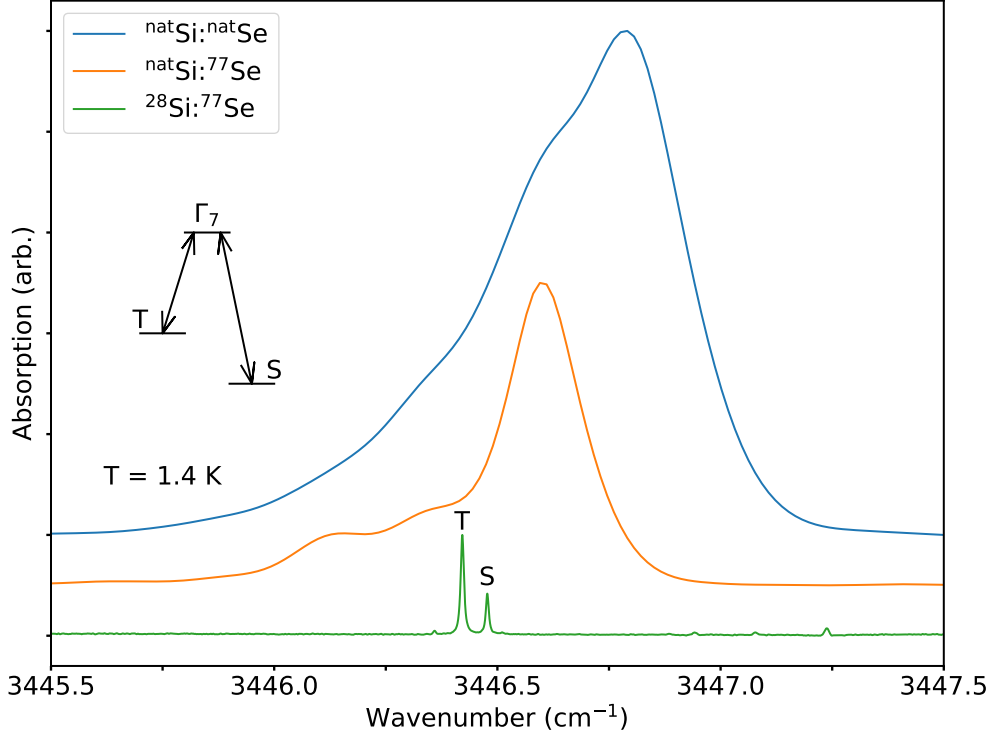


Figure 2.7: Absorption spectra comparing different isotopic combinations of silicon and selenium. As the samples become more isotopically pure the linewidth narrows significantly and the two transitions, $T \Rightarrow 1s:T_2\Gamma_7$ and $S \Rightarrow 1s:T_2\Gamma_7$ become resolvable. (Inset) the lambda transition composed of the two transitions $T \Rightarrow 1s:T_2\Gamma_7$ and $S \Rightarrow 1s:T_2\Gamma_7$.

2.5.1 Se Spin-Photon Interface

The spin-photon interface of the $\text{Si}^{77}\text{Se}^+$ system has a lot of promise to be the basis of a quantum computing architecture. Not only is it an excellent qubit but it possesses optical accessibility at a wavelength compatible with silicon photonics (2.9 μm). Having an entirely silicon based spin-photon interface allows the use of the scalability of the CMOS and silicon photonic industries. As the system is active in both absorption and luminescence both processes have the possibility of being used to generate entanglement between qubits.

The first possibility for an entanglement scheme, highlighted by Morse et al. [54], is to utilize cavity quantum electrodynamics (cQED) qubit coupling. The basis of the idea is that placing an atom with a two level optical transition of frequency ω_{21} into an optical cavity that confines light at frequency ω_c causes non-linear effects if $\omega_{21} = \omega_c$. In this situation the system is described by the Jaynes-Cumming model [45]

$$\mathcal{H} = \hbar\omega_{21}\sigma_{21}^\dagger\sigma_{21} + \hbar\omega_c a^\dagger a + \hbar g(\sigma_{21}a + \sigma_{21}a^\dagger) \quad (2.30)$$

where σ_{21}^\dagger and σ_{21} are the atomic raising and lowering operators, a^\dagger and a are the photon creation and annihilation operators, and g is the cavity-atom coupling constant, given by:

$$g = \mu_{21} \sqrt{\frac{\omega_{21}}{2\epsilon_0 \hbar V}} \quad (2.31)$$

where V is the modal volume of the cavity. The energy eigenstates of this system are [45]:

$$E_0 = 0, \quad (2.32)$$

$$E_{N,\pm} = N\hbar\omega_c + \hbar \frac{\Delta_{ac}}{2} \pm \frac{\hbar}{2} \sqrt{\Omega_N^2 + \Delta_{ac}^2}.$$

Where N is the total number of excitation quanta in the system. The two level atom being in the excited state is one excitation quantum and N photons in the cavity are N excitation quanta. $\Delta_{ac} = \omega_{21} - \omega_c$ is the detuning between atomic and cavity frequencies. $\Omega_N = 2g\sqrt{N}$ is the N -quanta Rabi frequency.

If the atom-cavity detuning is large the energy eigenstates approach those of an uncoupled system. Probing the cavity, only light resonant with the bare cavity frequency (or a higher harmonic) will transmit. If the atom-cavity detuning is small the eigenstates split by Ω_N , thus, probing the cavity will reveal two transmission peaks.

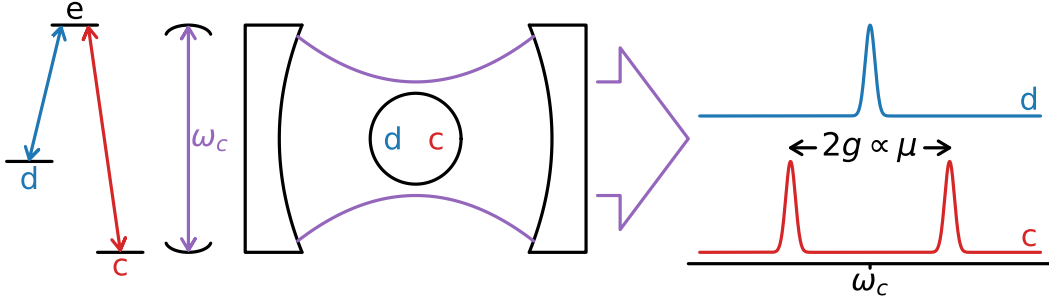


Figure 2.8: Schematic diagram of a cavity coupled to an atomic system with a lambda transition. The lambda transition is composed of the two transition $d \Rightarrow e$ and $c \Rightarrow e$. The cavity frequency, ω_c is resonant with the $c \Rightarrow e$ transition and is thus coupled. Probing the transmission spectra of the cavity will give the spectra shown to the right depending on the state of the atomic system. If in the detuned state, d , there is a single peak at the bare cavity frequency (blue spectra). If in the coupled state, c , there will be two peaks (red spectra) split by $2g$ which is proportional to the transition dipole moment, μ .

Consider placing instead a three-level atomic system, with two low lying states and one excited state composing a lambda transition, into the cavity as shown in Fig. 2.8. We will refer to the states as coupled, c , for which the transition frequency to the excited state, e , is resonant with the cavity frequency, and detuned, d , for which the transition frequency to e is detuned far from the cavity frequency. If the electron is in the detuned state, d , the cavity

will have only a single transmission peak at the bare cavity frequency, ω_c . If the electron is in the coupled state, c , the cavity will have two transmission peaks separated by $\Omega_1 = 2g$.

This maps over exactly to the three-level lambda transition of Si:⁷⁷Se⁺. Photonic cavities have been made on silicon-on-insulator chips with a resonant frequency in the mid-infrared [94]. Placing a single selenium atom into a cavity resonant with the $S \Leftrightarrow 1s:T_2\Gamma_7$ transition will create a system equivalent to that shown in Fig. 2.8 with the S state the coupled state, and the T state the detuned state. The qubit state can be determined by measuring the transmission via an adjacent on-chip waveguide.

With multiple cavities connected via an on-chip waveguide, entanglement can be generated between qubit-cavity systems via, for example, the bounce-bounce entanglement scheme [95]. Additionally, this provides a non-destructive means of measuring the spins state by probing the cavity with many photons at the bare cavity frequency and monitoring if the photons reflect or transmit.

Here we see the first optical property of note: the transition dipole moment, μ , for the $1s:A \Leftrightarrow 1s:T_2\Gamma_7$ transition. This value determines the splitting present in the coupled system. This is crucial as a low transition dipole moment results in a low splitting which makes resolving the two cases, coupled versus uncoupled, much harder.

Another possibility is to use the spin-dependent luminescence. Suppose the spin qubit is in an arbitrary superposition of S and T₀. By selectively exciting the $S \Rightarrow 1s:T_2\Gamma_7$ transition with a resonant optical pulse the state can be determined by measuring the resulting luminescence. If the spin is in T₀ there will be no luminescence, if the spin is in S there will be luminescence as the electron decays to the ground state. This readout scheme requires a high radiative efficiency as non-radiative decays can lead to misidentification of the state. In comparison to the cavity readout scheme this would be destructive and could not be done with multiple photons.

There is also the possibility of using the spin-dependent luminescence to entangle physically separate qubits [96, 97] as has been demonstrated with NV center qubits [24]. Such schemes require high radiative efficiency as well as high ZPL fraction as there is the requirement that the photons emitted be indistinguishable.

A measurement of these key optical properties, transition dipole moment, radiative efficiency, and ZPL fraction are crucial for any future implementations of the Si:⁷⁷Se⁺ spin-photon system. These values will inform the viability of the different spin-photon entanglement schemes presented as well as the requirements for the silicon photonic devices. In this work we attempt to measure these optical properties for future work with this system.

2.6 Diffusion

The theoretical discussion presented has all concerned bulk measurements on macroscopic samples with many centers – in our case, many Si:Se⁺ centers. The method by which we cre-

ate suitable samples is by incorporating selenium atoms into a silicon sample via diffusion. Simply put, diffusion is the redistribution of mobile atoms from regions of high concentration to regions of low concentration. In practice, this entails exposing silicon samples to gaseous selenium, allowing time for the selenium atoms to dissolve into the silicon lattice and redistribute throughout the silicon sample.

The one dimensional concentration profile, C , of any diffused impurity is determined by the diffusion equation [98]:

$$\frac{\partial C}{\partial t} = D \frac{\partial^2 C}{\partial x^2}. \quad (2.33)$$

Where x is the dimension of interest and t is time. D is the diffusivity, a physical property dependent on the diffusing element and the substrate into which it diffuses. The diffusivity depends exponentially on the temperature at which diffusion takes place,

$$D = D_0 e^{-\frac{E_a}{kT}}. \quad (2.34)$$

Where k is Boltzmann's constant, T is the temperature, D_0 and E_a are the element specific maximum diffusivity and activation energy.

In the case we are concerned with – the dopant provided by an ambient gas – we can assume that there is an infinite source at the boundary of our material. In this case the solution to Eqn. 2.33 is

$$C(x, t) = C_s \operatorname{erfc}\left(\frac{x}{2\sqrt{Dt}}\right). \quad (2.35)$$

Where $\operatorname{erfc}()$ is the complimentary error function and C_s is the surface concentration. For gas phase diffusion, the surface concentration will be limited by the solid solubility – the maximum concentration that an impurity can be present in a material. For gas phase diffusion, if the concentration outside the silicon is well above the solid solubility then C_s will be constant at the solid solubility. In general, the solid solubility is not well modeled by an Arrhenius equation as is the diffusivity. However, there is a large amount of literature mapping out the solid solubility of dopants in silicon upon which we can draw (Pichler [99] and the references therein).

In particularly thin samples, the dopant diffusion from both sides of the sample must be accounted for when determining the final diffusion profile. For a sample with $C(x; t = 0) = 0$ and $C(x = 0, L; t) = C_s$, Eqn. 2.33 can be solved via separation of variables as the following:

$$C(x, t) = \sum_{n=1}^{\infty} B_n \sin\left(\frac{n\pi x}{L}\right) e^{-Dn^2\pi^2 t/L^2} \quad (2.36)$$

$$B_n = \frac{2}{L} \int_0^L -C_s \sin\left(\frac{n\pi x}{L}\right) dx$$

Chapter 3

Sample Preparation and Experimental Techniques

In this section we outline our sample preparation procedure and the samples made for this work. Next we discuss the experimental equipment, setups, and techniques used for the measurements on the created samples. We will introduce the idea of Fourier transform infrared (FTIR) spectroscopy and its use for photoluminescence, absorption, and hole burning measurements. As well we will discuss our experimental design for magnetic resonance experiments.

3.1 Sample Preparation

Si:Se⁺ samples were made by diffusing selenium into p-type, boron doped, silicon samples. As boron is an acceptor, neutral selenium is singly or possibly doubly ionized as the sample is partially compensated. Both isotropically purified ²⁸Si and commercially available float-zone ^{nat}Si were used as silicon substrates. The ²⁸Si material had two levels of isotopic enrichment: 99.991 % ²⁸Si, 75 ppm ²⁹Si and 99.995 % ²⁸Si, 45 ppm ²⁹Si [100, 101]. The ²⁸Si had two levels of boron doping, a low boron (LB), [B] = (4.5 ± 1.0) × 10¹³ cm⁻¹ [100], and an intermediate boron (IB), [B] ≈ 1 × 10¹⁵ cm⁻¹. The ^{nat}Si had high boron (HB), [B] ≈ 5 × 10¹⁵ cm⁻¹.

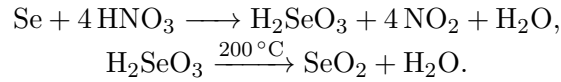
In all samples the boron was introduced during the growth of the silicon crystal, therefore, we assume the boron concentration is uniform throughout. As [Se⁺] is an important factor for calculating the optical properties, our goal was to create samples with a uniform [Se⁺]. The requirement for the diffusion is then to have [Se] > [B] across the sample to have the boron compensated and the sample be n-type everywhere, with [Se⁺] largely defined by [B].

Selenium is a relatively slow diffuser ($D_0 = 0.123$ cm²/s, $E_a = 2.457$ eV [99]) requiring many days at > 1000 °C temperatures to see non-negligible diffusion. To have [Se] > [B] across an entire sample would require diffusing into wafer-thin samples. However, the

conventional method of using elemental selenium as the diffusion source is unsuitable for diffusion into wafer samples as silicon sublimates in selenium vapour, etching away the surface. In order to diffuse into wafer samples we used selenium dioxide (SeO_2) as the diffusion source.

Selenium dioxide has been successful in diffusing selenium into silicon wafers without excessive surface damage [102, 103]. We attribute this protection from sublimation to oxygen forming a passivating silicon dioxide (SiO_2) layer. The selenium can diffuse through the oxide layer but does not etch the underlying silicon.

To this end we made batches of selenium dioxide using isotopically pure selenium via the following chemical reaction [104]:



Selenium was dissolved in 6 molar nitric acid, the solution was then heated in a furnace at 200°C until all the water evaporated leaving SeO_2 . Batches of $^{\text{nat}}\text{SeO}_2$, $^{77}\text{SeO}_2$, and $^{78}\text{SeO}_2$, were made.

Wafer samples were ≈ 0.5 mm thick, samples were different shapes, all roughly $10\text{ mm} \times 10\text{ mm}$. Additional thicker samples diffused with elemental selenium, created for previous work, were also studied. These thicker samples will be collectively referred as ‘block’ samples in contrast to the wafer samples. Although not studied in this work, aluminum doped $^{\text{nat}}\text{Si}$ block samples were also included during some of the diffusion processes.

The diffusion process involved sealing silicon sample(s) along with a selenium source in a quartz ampule. The ampules were then placed in a furnace at a set temperature for a set time. Six different ampules were made.

The preparation and diffusion process was the same for the first five ampules. For Ampules 1-5, sample(s) were cleaned by soaking in acetone, then isopropanol, then deionized water. They were then placed in a quartz ampule along with a source of selenium. The ampule was evacuated, backfilled with argon to a pressure of ≈ 100 Torr, then sealed. Ampules were then placed in a furnace at 1200°C for 7 days. After diffusion the samples were quickly quenched in water to avoid forming selenium pairs [99].

Ampule 6 was prepared and handled in the exact same manner as the other ampules but had a two part diffusion process. The first diffusion was at 1200°C for 5 days. Afterwards, absorption measurements (see Sec. 3.2.2) showed no sign of substitutional Se in the sample. This could possibly be due to the ampule cracking during the diffusion and all selenium vapour leaving the ampule. A second diffusion at 1200°C for 7 days was performed after which Se was confirmed to be present in the sample via an absorption measurement. The samples and selenium source included in each ampule are shown in Tab. 3.1.

The temperature and duration of the wafer diffusions were selected as it was consistent with previous diffusions and was sufficient to have $[\text{Se}] > [\text{B}]$ throughout the sample (see

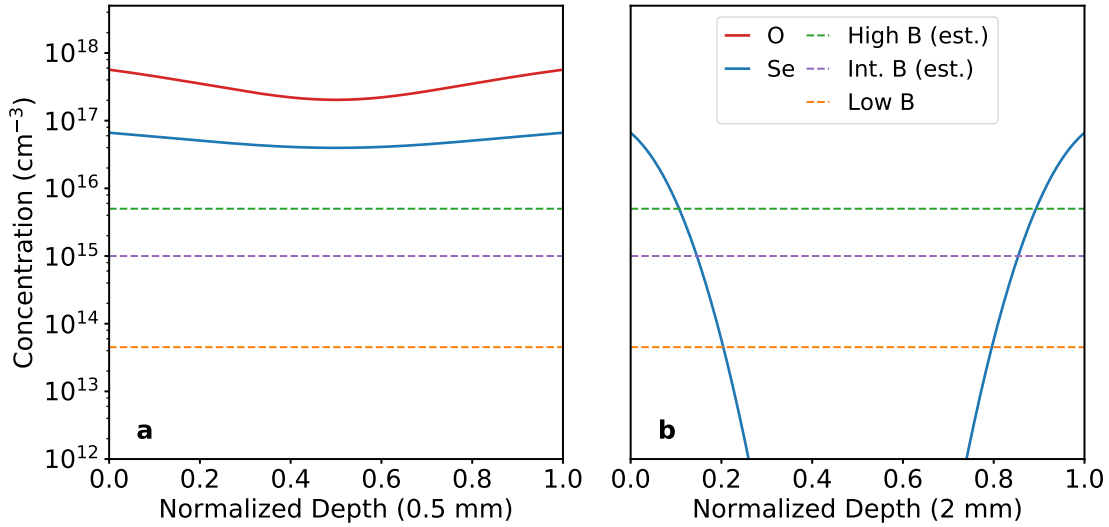


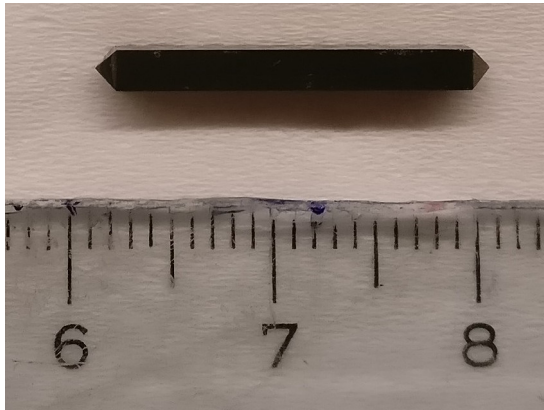
Figure 3.1: Calculated concentration profiles after a 1200 °C diffusion for 7 days for (a) a 0.5 mm thick silicon wafer diffused with SeO_2 (ie both Se and O) and (b) a 2 mm thick silicon block sample diffused with elemental Se (ie only Se). The three different boron levels are also shown.

Fig. 3.1 a). As a consequence of working with SeO_2 the diffusion was also expected to introduce a significant concentration of oxygen ($D_0 = 0.16 \text{ cm}^2/\text{s}$, $E_a = 2.529 \text{ eV}$). Block samples were not expected to have $[\text{Se}] > [\text{B}]$ across the entire sample as shown in Fig. 3.1 b).

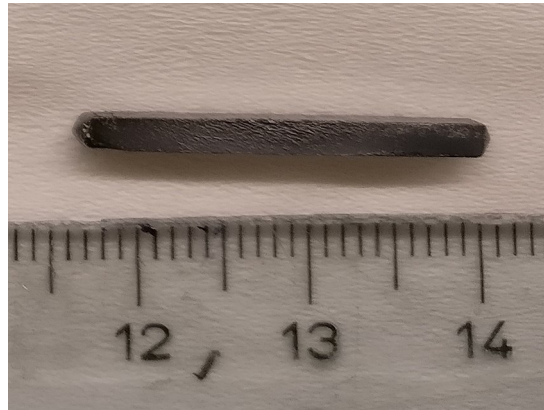
The elementally diffused samples from Ampule 4, 5, and 6 had etched surfaces as expected. Sample(s) from Ampules 1 and 3 showed no sign of etching, and there was a silicon dioxide layer present, as expected. The samples from Ampule 2, unexpectedly, also showed signs of etching. This could be due to the SeO_2 used containing a non-negligible amount of elemental Se. The SeO_2 used for Ampule 2 did have a red tinge rather than the pure white colour of the other SeO_2 batches. This could be due to elemental selenium present in the allotrope known as red selenium. If the SeO_2 used had a large portion of elemental Se this could result in insufficient oxygen to form a protective oxide layer.

Fig. 3.2 shows a comparison of the surface damage of samples from Ampules 1 and 2. Fig. 3.2 c and d show the surface profile of the two samples, measured with a Bruker Dektak XT profileometer. The sample from Ampule 1 has a much smoother surface.

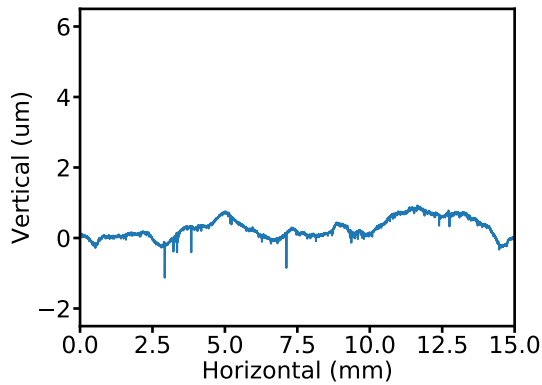
The wafer samples from Ampule 1 and Ampule 2 were polished to remove $\approx 50 \mu\text{m}$ from each side. After cleaning by soaking in acetone, then isopropanol, then deionized water, the samples were etched with a 10:1 $\text{HNO}_3:\text{HF}$ solution for ≈ 5 minutes which removed $\approx 10 \mu\text{m}$ from each side. This was done to remove surface damage and to remove surface layers in case of cross contamination from aluminum doped $^{\text{nat}}\text{Si}$ samples present in each ampule (see Sec. 4.1 for discussion of aluminum). The sample from Ampule 3 was etched with HF



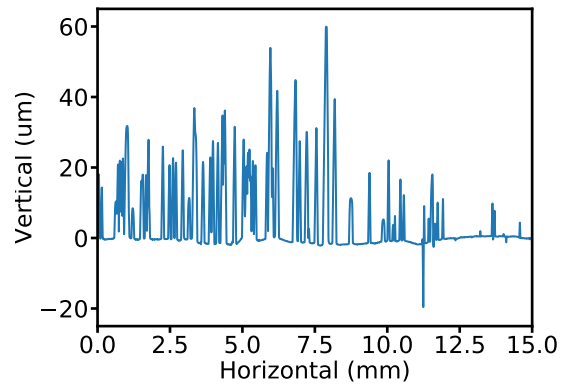
(a) $\text{natSi:}^{77}\text{Se:Al}$



(b) $\text{natSi:}^{78}\text{Se:Al}$



(c) $\text{natSi:}^{77}\text{Se:Al}$ surface profile



(d) $\text{natSi:}^{78}\text{Se:Al}$ surface profile

Figure 3.2: A comparison of the surface damage present for samples from Ampule 1 and Ampule 2. Images of samples (a) $\text{natSi:}^{77}\text{Se:Al}$ and (b) $\text{natSi:}^{78}\text{Se:Al}$. Surface profilometry of samples (c) $\text{natSi:}^{77}\text{Se:Al}$ and (d) $\text{natSi:}^{78}\text{Se:Al}$. Note that the surface profile of $\text{natSi:}^{77}\text{Se:Al}$, (c), is plotted on an axis 10 times smaller than $\text{natSi:}^{78}\text{Se:Al}$, (d).

for ≈ 5 minutes to remove the silicon dioxide surface that formed. The block samples were etched with a 10:1 $\text{HNO}_3:\text{HF}$ solution for ≈ 5 minutes to remove surface damage.

	Se Source	Sample Name	Si substrate	Doping (est.)
Ampule 1	$^{77}\text{SeO}_2$	w ^{nat} Si: ^{77}Se :HB	^{nat} Si wafer	B (5×10^{15})
		w ^{28}Si : ^{77}Se :IB	^{28}Si (99.995 %) wafer	B (1×10^{15})
		w ^{28}Si : ^{77}Se :LB	^{28}Si (99.995 %) wafer	B ($(4.5 \pm 1.0) \times 10^{13}$ †)
		^{nat} Si: ^{77}Se :Al	^{nat} Si ($2 \times 2 \times 20$ mm ³)	Al (1.5×10^{15})
Ampule 2	$^{78}\text{SeO}_2$	w ^{nat} Si: ^{78}Se :HB	^{nat} Si wafer	B (5×10^{15})
		w ^{28}Si : ^{78}Se :IB	^{28}Si (99.995 %) wafer	B (1×10^{15})
		w ^{28}Si : ^{78}Se :LB	^{28}Si (99.995 %) wafer	B ($(4.5 \pm 1.0) \times 10^{13}$ †)
		^{nat} Si: ^{78}Se :Al	^{nat} Si ($1.8 \times 1.8 \times 25$ mm ³)	Al (5×10^{14})
Ampule 3	^{nat} SeO ₂	w ^{nat} Si: ^{nat} Se:HB	^{nat} Si wafer	B (5×10^{15})
Ampule 4	^{77}Se	^{28}Si : ^{77}Se :LB	^{28}Si (99.991 %) ($2 \times 2 \times 10$ mm ³)	B ($(4.5 \pm 1.0) \times 10^{13}$ †)
Ampule 5	^{78}Se	^{28}Si : ^{78}Se :IB	^{28}Si (99.995 %) ($10 \times 10 \times 3.5$ mm ³)	B (1×10^{15})
Ampule 6	^{77}Se	^{28}Si : ^{77}Se :IB	^{28}Si (99.995 %) ($10 \times 10 \times 3.5$ mm ³)	B (1×10^{15})

Table 3.1: Name, silicon substrate, estimated doping, and diffusion source for all samples studied in this work. Sample(s) grouped together were diffused in the same ampule. Sample names beginning with a ‘w’ are wafer samples. Doping values marked with a † are from Devyatyhk et al. [100] all other doping values are estimates.

3.2 FTIR

We measured photoluminescence and absorption spectra using a Bruker IFS 125HR Fourier transform infrared (FTIR) spectrometer. The basic function of an FTIR spectrometer is to have a light source feed into a Michaelson interferometer with one arm stationary, one arm ending with a movable mirror, and a detector at the output. A schematic is shown in Fig. 3.3. For simplicity we will consider an ideal, partially silvered mirror with 50 % transmission and reflection.

When the two arms of the interferometer are equal length the light will constructively interfere at the output. Moving one arm's mirror away from this zero path length difference point by a distance $d = c\tau/2$ the electric field at the detector will be

$$E_d = \frac{E(t)}{2} + \frac{E(t + \tau)}{2} \quad (3.1)$$

The intensity, $I_d = |E_d|^2$, will then be:

$$I_d = \frac{|E(t)|^2}{4} + \frac{|E(t + \tau)|^2}{4} + \frac{\Re\{E(t)E^*(t + \tau)\}}{2} \quad (3.2)$$

Where $\Re\{\}$ is the real component. If we consider monochromatic light, $E(t) = E_0 e^{-i\omega_0 t}$, and have $|E_0|^2 = I_0$, then we have:

$$\begin{aligned} I_d &= \frac{I_0}{2} (1 + \Re\{e^{-i\omega_0 t} e^{i\omega_0 (t+\tau)}\}) \\ I_d(\tau) &= \frac{I_0}{2} (1 + \cos(\omega_0 \tau)). \end{aligned} \quad (3.3)$$

Expressing this in terms of the mirror's position, $d = c\tau/2$, we have

$$I_d(d) = \frac{I_0}{2} (1 + \cos(2\omega_0 d/c)). \quad (3.4)$$

Taking the Fourier transform of this gives a delta function spike at the frequency of the input light (ignoring negative frequencies), ie, the power spectrum of the monochromatic light.

If there are two input frequencies then the measured intensity as a function of mirror position is

$$I_d(d) = \frac{I_0}{2} (1 + C_1 \cos(2\omega_1 d/c) + C_2 \cos(2\omega_2 d/c)) \quad (3.5)$$

where C_1 and C_2 are the fractions of the input light in each frequency. Again the Fourier transform gives the power spectrum of the source (two delta function spikes at ω_1 and ω_2). In general, the 'interferogram', the intensity as a function of mirror position, will give the power spectrum of the input light by applying a Fourier transform.

A FTIR spectrometer provides a powerful tool for both absorption and photoluminescence spectroscopy. A sample can be placed in the beam path of the output arm to measure the absorption spectra or the emitted photons of a luminescent sample can be routed to the input arm of an FTIR spectrometer to measure the photoluminescence spectra. Compared to other spectroscopy methods, FTIR has a few advantages.

Firstly, a single broadband source is all that is needed to obtain high resolution spectra at all emitted wavelengths. The resolution is not determined by the linewidth of the source (as in laser spectroscopy) but by how much of the interferogram can be measured. In any physical implementation the mirror can only move a finite amount and thus the interferogram measured will cut off at some point. This is equivalent to the interferogram being multiplied by a boxcar function. The Fourier transform is then the convolution of the true spectra and a sinc() function with a linewidth given by the inverse of the boxcar width. Thus a larger boxcar, ie, moving the mirror further, gives a finer resolution. In practice a smoother apodization function is used to avoid the ringing present in sinc() functions, however, the trade off is lower resolution. The resolution cannot be infinitely increased by moving the mirror further and further. Other optical components in the system, apertures, and internal mirrors, will begin to limit the resolution achievable.

Another advantage of using an FTIR spectrometer is quantitative results can be obtained even at resolutions too low to resolve the exact lineshape of a spectral feature. FTIR spectroscopy preserves the area of a spectral feature regardless of the resolution used.

Suppose a measured spectrum consists only of a single, sharply peaked, spectral line, $g(\omega)$, with area normalized to unity, and a linewidth $\Delta\omega$. The interferogram, as a function of mirror position, will have a linewidth of $\Delta d_{\text{int}} \propto 1/\Delta\omega$. Now suppose we are limited to a resolution too low to resolve $g(\omega)$. This may be due to intentionally lowering the resolution to increase signal to noise or to lower the time required to measure the spectra. This could also be due to the physical limitations of the system (ie the mirror cannot move any further). Regardless, the result is that the interferogram is cut-off to a width $\Delta d_{\text{co}} < \Delta d_{\text{int}}$. This cut-off is equivalent to multiplying the interferogram by an arbitrary cut-off function with the width Δd_{co} . This cut-off function, $C(t)$, can be any symmetric function that goes to zero characterized by a width Δd_{co} . The example used above, a boxcar, is one such example.

The interferogram will be given by:

$$\mathcal{FT}^{-1}[g(\omega)] \cdot C(d). \quad (3.6)$$

The spectra, given by the Fourier transform, will be the convolution of the individual Fourier transforms

$$\int_{-\infty}^{\infty} g(\omega - \omega') \mathcal{FT}[C](\omega') d\omega'. \quad (3.7)$$

The resulting area of the low resolution spectral line is

$$\begin{aligned}
 & \int_{-\infty}^{\infty} \int_{-\infty}^{\infty} g(\omega - \omega') \mathcal{FT}[C](\omega') d\omega' d\omega \\
 & \int_{-\infty}^{\infty} \mathcal{FT}[C](\omega') \int_{-\infty}^{\infty} g(\omega - \omega') d\omega d\omega' \\
 & \int_{-\infty}^{\infty} \mathcal{FT}[C](\omega') \cdot 1 d\omega'
 \end{aligned} \tag{3.8}$$

Thus, as long as the cut-off function is correctly normalized, $\int_{-\infty}^{\infty} \mathcal{FT}[C](\omega') d\omega' = 1$, the area of a spectral feature will be conserved. However, this means that as a spectral feature broadens, the peak will decrease to ensure area conservation. Thus, there is a limit to how low resolution one can go: as the peak decreases the spectral line will eventually be lost in the noise of the measurement.

This is an important fact as many of the optical properties from Sec. 2.3 rely only on the area of a spectral feature.

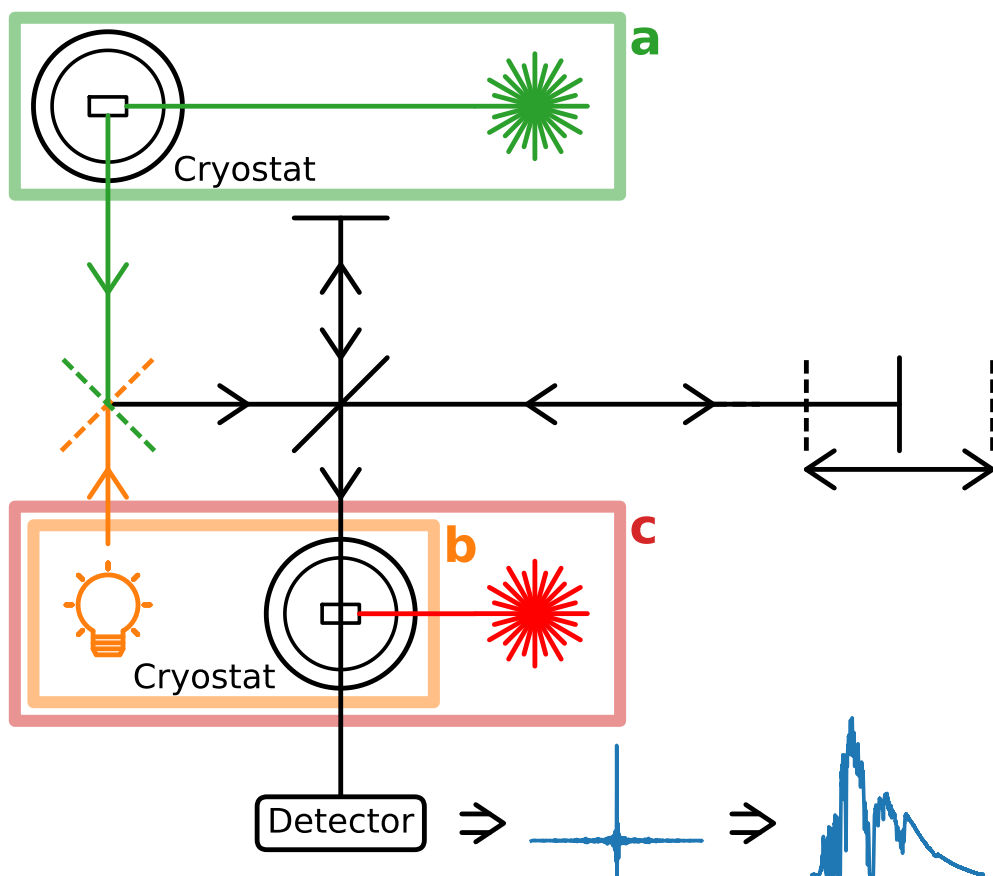


Figure 3.3: Schematic diagram showing the three configurations in which we use Fourier transform infrared spectroscopy. (a) Components highlighted in green are used for photoluminescence measurements. A liquid-helium cooled sample is excited with a laser source and the emission from the sample is collected as the source light to the FTIR. (b) Components highlighted in orange are used for absorption measurements. A broad band light is used as the source and a liquid-helium cooled sample is placed in the FTIR arm before the detector. (c) Components highlighted in red are used for hole burning measurements. This is the same setup as absorption with the addition of a perpendicular laser used to resonantly excite a transition.

3.2.1 Photoluminescence

Photoluminescence measurements were performed by exciting a liquid-helium cooled sample with laser light. The laser light was either at an above bandgap energy to excite many different luminescence processes or tuned to a resonant wavelength to selectively pump a

desired transition. In both cases a fraction of the isotropic luminescence was collected and focused into the FTIR spectrometer to act as the ‘source’. This setup is shown in Fig. 3.3 a. Exact laser wavelengths, powers, as well as detectors used are listed in the relevant sections in Ch. 4.

3.2.2 Absorption

Absorption measurements were performed by placing a liquid-helium cooled sample in the output arm of the FTIR between the beamsplitter and the detector. A Globar mid-infrared source was used. For a given absorption spectra a measurement was made with and without the sample in the FTIR output beam. These spectra were then approximated to be $I(L)$ and $I(0)$ (see Sec. 2.3) and the absorption coefficient spectra was determined as

$$\bar{\alpha}(\omega) = -\frac{1}{L} \ln \left(\frac{I(L)}{I(0)} \right). \quad (3.9)$$

This setup is shown in Fig. 3.3 b. Exact details of detectors as well as additional filters used to increase the signal to noise ratio are included in the relevant sections of Ch. 4.

When measuring the very thin wafer samples, if the sample was perpendicular to the beam of the FTIR the sample acted as a Fabry-Perot cavity causing fringes in the absorption spectra due to constructive/destructive interference from multiple internal reflections at the sample’s surfaces. To avoid these fringes we rotated the samples to be at an angle ($\approx 30\text{-}45^\circ$) relative to the beam of the FTIR to have the reflected rays spatially separated from the main beam and not contribute to the obtained spectra.

From the Sec. 2.3 we see that extracting peak, area, and linewidth values from absorption spectra are important for determining optical properties. To extract these values we fit absorption spectral lines with asymmetric pseudo-voigt functions [105]. A voigt function is the convolution of a Lorentzian and a Gaussian, whereas a pseudo-voigt function is a linear combination of a Lorentzian and a Gaussian. A pseudo-voigt function is used as it is more practical. Following Stancik et al. [105] we define the asymmetric pseudo-voigt function as:

$$V(\omega) = pL(\omega) + (1 - p)G(\omega) \quad (3.10)$$

where p is the fraction of Lorentzian to Gaussian. L and G are asymmetric Lorentzian and Gaussian distributions respectively, given by:

$$\begin{aligned} L(\omega) &= \frac{2A/\pi\gamma(\omega)}{1 + 4[(\omega - \omega_0)/\gamma(\omega)]^2}, \\ G(\omega) &= \frac{A}{\gamma(\omega)} \sqrt{\frac{4\ln 2}{\pi}} \exp \left[-4\ln 2 \left(\frac{\omega - \omega_0}{\gamma(\omega)} \right)^2 \right] \end{aligned} \quad (3.11)$$

where A is the area, ω_0 is the peak position and $\gamma(\omega)$ is the asymmetric linewidth given by

$$\gamma(\omega) = \frac{2\gamma_0}{1 + \exp[a(\omega - \omega_0)]}, \quad (3.12)$$

where a is the asymmetry parameter. Negative values of a skew the spectrum to higher frequencies, and vice versa for positive values. γ_0 is the full width at half max (FWHM), this is what we refer to as the linewidth.

3.2.3 Hole Burning

Hole burning measurements were performed using the same setup as absorption measurements with the addition of a pumping laser aligned perpendicular to the beam of the FTIR. The laser was tuned to the peak of the Si:⁷⁷Se⁺ 1s:A:T \Rightarrow 1s:T₂Γ₇ transition in order to burn a spectral hole.

The theoretical discussion of hole burning presented in Sec. 2.3.2 makes the simplification that an absorption spectrum can be measured before the population excited by the hole burning laser can return to the ground state. In practice this requires a long lived shelving state, long enough to complete the absorption measurement before population can return to the ground state. By working with the lambda transition of ⁷⁷Se (1s:A:S, 1s:T₂Γ₇, 1s:A:T, see the inset of Fig. 2.7) we pumped the population from the triplet state into the singlet state. The result is a spectral ‘hole’ is burned in the triplet peak due to the decrease in population, and a spectral ‘anti-hole’ appears in the singlet peak due to an increase in population.

In this configuration the relevant time constant to return to equilibrium is the spin population lifetime, T₁. The T₁ lifetime was found to be on the order of hours [93] allowing an FTIR scan to be made before the system returned to equilibrium.

3.3 Magnetic Resonance and Tip-Angle

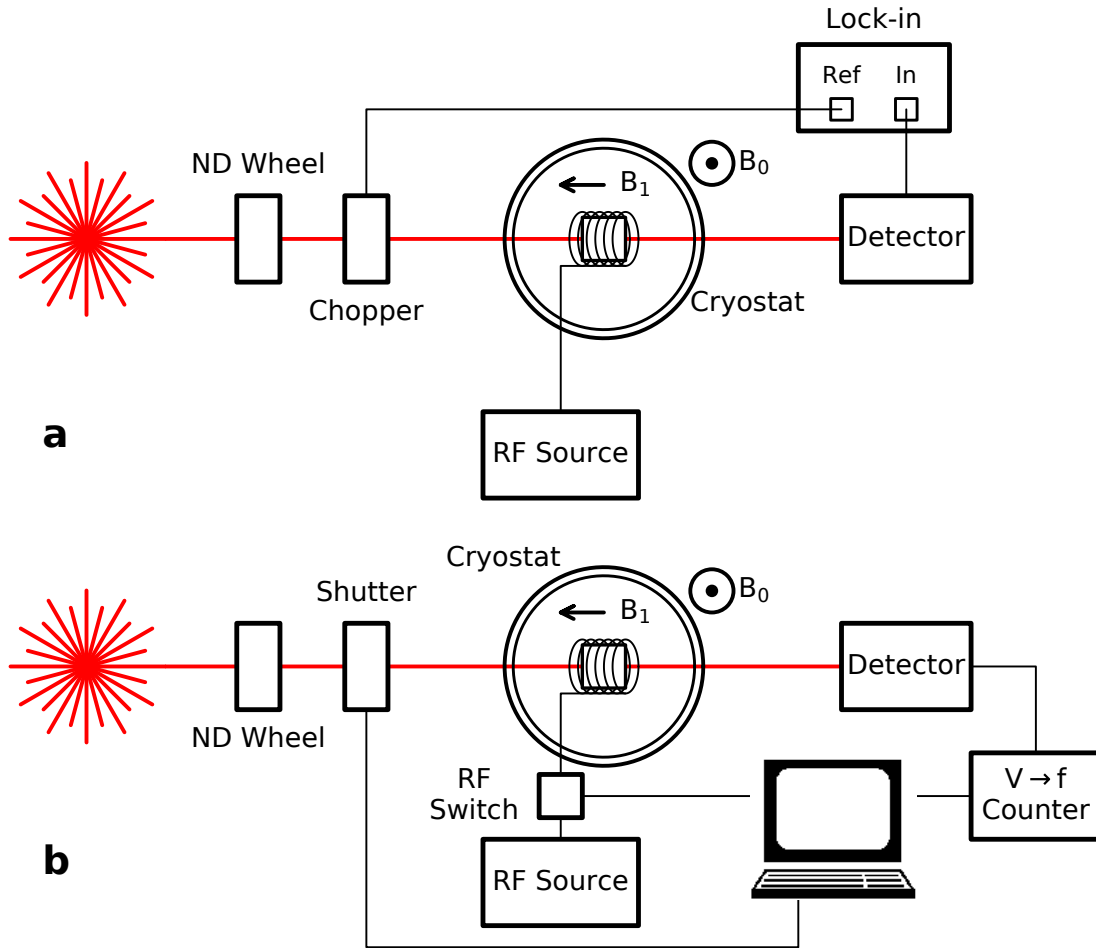


Figure 3.4: Experimental setups used for magnetic resonance and tip-angle experiments. In both setups a liquid-helium cooled sample is illuminated with a laser source. A Helmholtz coil pair surrounding the cryostat is used to generate a static, vertical, magnetic field, B_0 . The sample is in a resonator with an RF magnetic field, B_1 , perpendicular B_0 . (a) Setup used for both laser and RF scans. The laser light is modulated by a chopper and a lock-in measurement is made as either the laser or the RF source is scanned. (b) Setup used for pulsed RF experiments. A computer controls the timing of RF pulses, shutter open/close, and triggering of a counter.

3.3.1 Laser/RF Scan

Transmission spectra of the $\text{Si:Se}^+ 1s:A \Rightarrow 1s:T_2\Gamma_7$ were obtained by modulating a tunable diode laser (Nanoplus) with a chopper and performing a lock-in measurement as the frequency of the laser was scanned across the transition. A neutral density (ND) filter wheel

was used to attenuate the laser light. The detector was a liquid-nitrogen cooled InAs detector with a current amplifier (Ithaco 1212 current amplifier) used to convert the detector's response to voltage. This setup is shown in Fig. 3.4 a.

To perform a magnetic resonance RF scan we placed the sample in a split ring resonator [106] tuned to ≈ 1.66 GHz (represented as a coil in Fig. 3.4). The resonator was made by wrapping a quartz tube with copper tape leaving a slit down the length. Tuning was achieved by moving a copper plate towards or away from the slit. The resonator was excited by having a loop-terminated coaxial cable placed at one end of the resonator. This cable was then attached to an RF signal generator.

To perform the RF scan the laser was held at a constant frequency (tuned to the $1s:A:T \Rightarrow 1s:T_2\Gamma_7$ transition) and modulated by a chopper. A lock-in measurement was made as the frequency of the applied RF source was swept. A Helmholtz coil outside the cryostat was used to generate a static, vertical, magnetic field, B_0 . This was done to separate the three singlet to triplet MR transitions (see Fig. 2.6 c). This setup is shown in Fig. 3.4 a.

3.3.2 Pulsed RF Experiments

For pulsed RF measurements, such as a tip-angle measurement, a lock-in measurement is not appropriate. Instead the chopper is replaced with a shutter and the detector's signal is routed to a voltage to frequency converter and USB counter. This is shown in Fig. 3.4 b.

Pulsed RF measurements began by initializing the spins by tuning the laser to the $1s:A:T \Rightarrow 1s:T_2\Gamma_7$ transition to hyperpolarize the spins into the singlet state. This was followed by a laser off dark time wherein resonant RF pulses were applied to the resonator using an RF switch to gate a constant RF source on and off. To measure the state of the system after the pulses, the laser was again turned on, tuned to the $1s:A:T \Rightarrow 1s:T_2\Gamma_7$ transition. By monitoring the transmission versus time the final state polarization can be determined. If any spins are in the readout state, T, some laser light will be absorbed and the transmission will be initially low. As the laser pumps the spins to the S state there will be negligible absorption and the transmission will be high. This transient response was used to measure the relative population of the two states, S or T. A schematic of the transients seen is shown in Fig. 3.5 showing how the detector response changes with relative population. When 0 % of the population is in the readout state, T, there is no absorption and thus no transient (red line in Fig. 3.5). When 100 % of the population is in the readout state there is a large transient (orange line in Fig. 3.5) as electrons are pumped to the singlet state. Intermediate values between 0 % and 100 % have a transient in between these two extremes.

We used the integrated area above the transient responses as the measure of final state population (the hatched area in Fig. 3.5). To obtain this integrated area the detector's response is further amplified by a differential preamplifier (Ithaco 1201 low noise preamplifier). This signal is then routed to a voltage-to-frequency (V-f) converter. The V-f converter generates TTL (transistor-transistor logic) pulses at a frequency proportional to the input

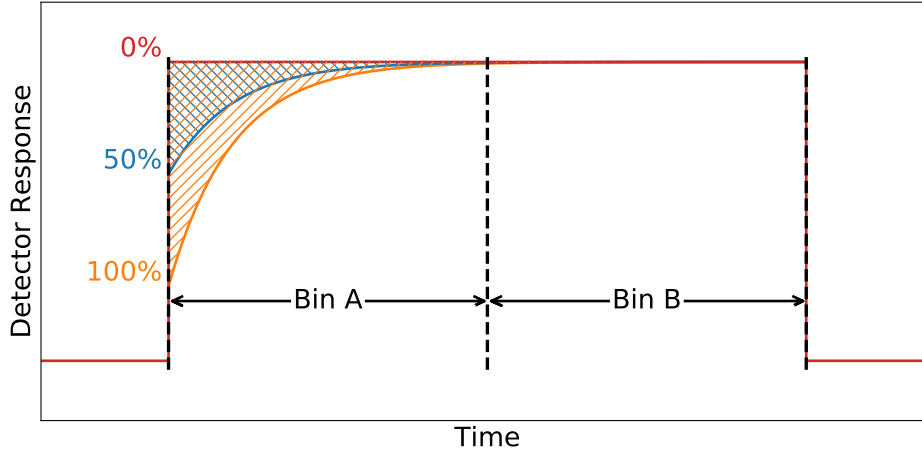


Figure 3.5: Schematic diagram of the transient area readout method. The integrated signal of Bin A is subtracted from Bin B to obtain the transient area (hatched area). The transient area for three different final state distributions is shown: 0 % in readout state (red), 50 % in readout state (blue), 100 % in readout state (orange).

voltage. The V-f converter is then connected in parallel to two channels of a USB counter. This setup allows a time integration of the area below the detector response. To obtain the area above the detector response we set the two channels of the counter to be active during different times while measuring the transient as shown in Fig. 3.5. One of the counter channels is active during the transient, the other is active after the transient has decayed away. By subtracting the two values, the area above the transient, proportional to the population of spins in the T state, is recorded as the signal.

The timing of the laser shutter, the RF pulses, and the triggering of the counter were all controlled by a computer communicating with a precisely timed TTL pulse generator (Pulseblaster).

Chapter 4

Experimental Results and Discussion

We studied the Si:Se samples through photoluminescence, absorption, tip-angle, and hole burning. We began with an investigation of the impurities present in the samples via photoluminescence and absorption spectroscopy. Next we investigated the photoluminescence and absorption spectra of the Si:Se system concluding with an evaluation of the transition dipole moment of the $\text{Si:Se}^+ 1s:A \Leftrightarrow 1s:T_2\Gamma_7$ transition. An independent verification of the transition dipole moment result was determined via the results of a tip-angle measurement of a single sample. Furthermore, we performed hole burning on a single sample to obtain an estimate of the excited state lifetime of $1s:T_2\Gamma_7$. Finally, we determined estimates of the optical properties of the neutral selenium, $\text{Se}^0 1s:A \Leftrightarrow 1s:T_2$ transition.

4.1 Impurities

Our ultimate goal was to study the optical properties of the selenium introduced in our samples. However, in addition to selenium there were also impurities present in the samples from before diffusion and impurities introduced during diffusion. In this section we present our investigation of impurities other than selenium, the results of which informed our investigations of selenium.

We investigated the photoluminescence spectra of the wafer samples which provided a qualitative measure of impurities present. Next we investigated absorption spectra to gain a quantitative measure of another subset of impurities

4.1.1 Impurities – Photoluminescence

We examined the newly created wafer samples using FTIR-photoluminescence as depicted in Fig. 3.3. We excited the samples using non-resonant, above bandgap laser light (200 mW, 532 nm). A CaF_2 beamsplitter and a liquid-nitrogen cooled Ge diode detector were used to obtain the FTIR spectra. A representative selection of the spectra is shown in Fig. 4.1.

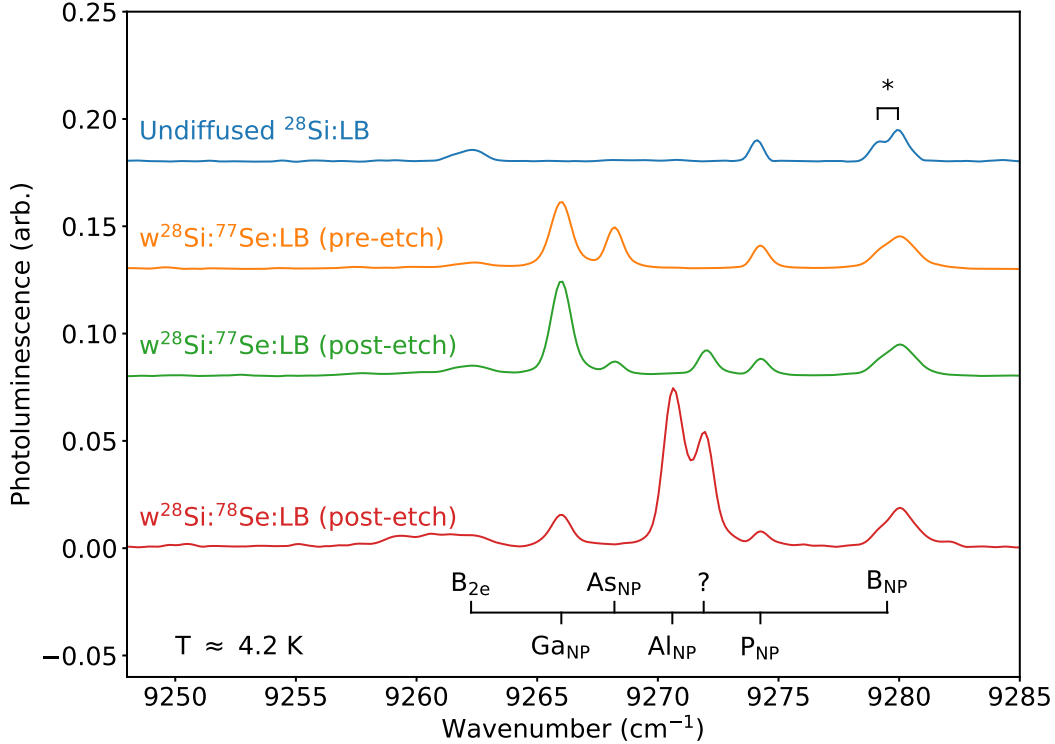


Figure 4.1: Photoluminescence spectra of the bound exciton (BE) no-phonon (NP) region showing donor and acceptor bound exciton recombination. The NP BE recombination luminescence lines of multiple impurities are indicated. B_{2e} corresponds to the recombination of two excitons at a boron center. Gallium, arsenic, and aluminum have been unintentionally introduced during the diffusion process (see text). An additional, unknown, line (?) is present after polishing and etching the samples. A spectra of $w^{28}\text{Si}:\text{}^{78}\text{Se}:\text{LB}$ before polishing/etching is not shown as the surface damage was too extensive to resolve any spectral features. Spectra were recorded at a resolution of 1 cm^{-1} . At this resolution the splitting of the B_{NP} line is partially resolved (*) [78].

The region shown is known as the no-phonon region in which excitons created by the laser light recombine at donor and acceptor impurities without the emission of a phonon. The binding of excitons is competitive between impurities, for this reason we present the low boron samples which have the clearest view of all the impurities and are not dominated by the boron recombination. We have also normalized the spectra to the boron TO (transverse optic) bound exciton phonon replica line [71] (not shown).

We see that in the bare, undiffused, material there is both boron and phosphorus [78] as expected [100]. After diffusion the samples show signs of additional impurities, namely, gallium, arsenic, and aluminum indicated by their respective no-phonon lines [71, 107, 78, 108]. There is also an unknown no-phonon line that appears only after polishing and etching the

samples, marked with a (?). The $w^{28}\text{Si}:^{78}\text{Se}:\text{LB}$ sample is only shown after the polish/etch as the untreated samples from Ampule 2 had too much surface damage to resolve any of the no-phonon lines.

Similar spectra were obtained for intermediate boron ^{28}Si samples showing the same impurities present. A summary of impurities identified in photoluminescence is shown in Tab. 4.1.

The gallium and arsenic were likely introduced as contamination from some point in the sample making procedure. Aluminum is only present in the samples from Ampule 2, most likely introduced from cross contamination from the $^{\text{nat}}\text{Si}:^{78}\text{Se}:\text{Al}$ sample. As mentioned in Sec. 3.1 the samples from Ampule 2 showed extensive surface damage as compared to the samples from Ampule 1 and 3. It is possible that the sublimation of the $^{\text{nat}}\text{Si}:^{78}\text{Se}:\text{Al}$ sample in Ampule 2 introduced aluminum into all the other samples present.

4.1.2 Impurities – Absorption

While photoluminescence measurements provide an excellent means for determining shallow donor and acceptor impurities present in a sample the results are generally qualitative. With absorption measurements it is much easier to generate quantitative measurements of impurity concentrations via tabulated area or peak conversion factors. To this end, absorption spectra of all samples were obtained using the FTIR-absorption setup shown in Fig. 3.3. A KBr beamsplitter, a Globar mid-IR source, and a liquid-nitrogen cooled mercury cadmium telluride (MCT) detector were used to obtain spectra.

Fig. 4.2 shows a region of the spectrum between $\approx 600\text{-}1200\text{ cm}^{-1}$ showing a wafer sample before and after diffusion. We see that both carbon and oxygen have been introduced into the samples during the diffusion process as evidenced by their respective local vibrational modes (LVM) seen at 607 cm^{-1} [109] and 1136 cm^{-1} [110] respectively.

Additionally, the presence of boron can be seen in the samples before diffusion as evidenced by the boron split-off band hole transition, $2p'$, at 669 cm^{-1} [111]. Acceptors, like boron, also possess a hydrogenic series of transitions, although, unlike donors these states are hole states extending to the valence band. The valence band maximum of silicon has a doubly degenerate band at zero momentum as well as a split off band due to the spin-orbit coupling of the holes. It is these split-off band hole transitions we investigated.

The B $2p'$ line is absent or reduced in samples after diffusion as the boron is being compensated by the selenium. It was found that only the wafer samples were completely compensated as indicated by the complete disappearance of the B p' lines. This is expected from the calculated diffusion profiles for the different sample widths (see Sec. 3.1).

To determine the impurity concentrations in the samples before (boron) and after (carbon, oxygen) diffusion we made use of conversion factors to convert from an impurity's spectral response to an average concentration as described in Sec. 2.3.

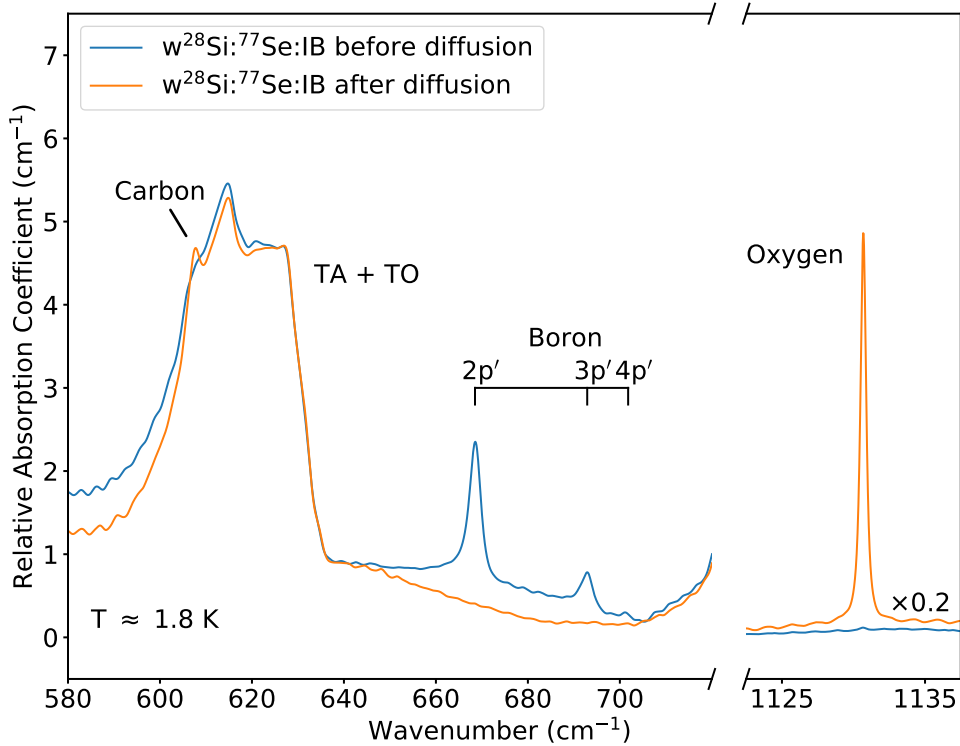


Figure 4.2: Absorption spectra of the $w^{28}\text{Si}^{77}\text{Se}:\text{IB}$ sample before and after diffusion. The phonon mode used to calculate the pathlength is labeled TA + TO (TA: transverse acoustic, TO: transverse optic). The carbon local vibrational mode (LVM) at 607 cm^{-1} was used to calculate [C]. The boron $2p'$ line at 669 cm^{-1} was used to calculate [B]. The absence of the electronic boron lines indicate that the sample is fully compensated. The oxygen LVM at 1136 cm^{-1} was used to calculate [O]. The spectra are shown at the relevant resolutions for the peak conversion factors used. To the left of the split axis the spectra is at a resolution of 1 cm^{-1} . To the right of the split the spectra is at a resolution of 0.5 cm^{-1} . The right side has also been multiplied by a factor of 0.2 for ease of viewing.

However, the wafer samples were held at an angle to the FTIR beam during measurement to reduce fringing in the spectrum. Thus, the pathlength of light through the sample is not simply the thickness of the sample. To determine the pathlength necessary to calculate the absorption coefficient (Eqn. 3.9), we made use of the TA + TO phonon feature [109] seen in Fig. 4.2 to determine the pathlength. This phonon feature is due to the silicon lattice absorbing light and exciting phonons, specifically a TA phonon (transverse acoustic) and a TO phonon (transverse optical). As this absorption feature depends only on the amount of silicon the light passes through, its size can be used to convert an absorption spectra (unitless) to an absorption coefficient spectra (cm^{-1}).

To obtain this pathlength conversion factor we measured the spectra of a much larger piece of float-zone $^{\text{nat}}\text{Si}$, with a thickness of 3.028 mm. As the sample was much thicker we could mount it perpendicular to the FTIR beam without worry of internal reflections causing substantial fringing. The absorption spectra of the phonon feature was recorded at the same temperature and resolution as the wafer samples. By dividing the thickness of the sample by the height of the phonon feature (the difference from the plateau at 630 cm^{-1} to the plateau at 640 cm^{-1}) we obtained a conversion factor of $3.80 \pm 0.04\text{ cm}^{-1}$. This process was repeated with a thick ^{28}Si sample, and the conversion factor was found to be equivalent.

For a given absorption spectra, the pathlength can be determined by dividing the height of the TA + TO phonon feature by the pathlength conversion factor. Likewise, an absorption spectra (unitless) can be converted into a absorption coefficient spectra (cm^{-1}) by normalizing the phonon height to 3.8 cm^{-1} .

After converting to absorption coefficient spectra we fit the carbon, boron, and oxygen spectral lines with asymmetric pseudo-voigt functions (Eqn. 3.10) to determine the peak value, $\bar{\alpha}_{\text{max}}$, and the area, $\int \bar{\alpha} d\nu$.

The carbon peak was isolated from the background phonon feature by subtracting the absorption coefficient spectra of undiffused samples of the same silicon isotopic composition. Matching isotopic compositions is important as the TA + TO phonon feature is at slightly different energies in ^{28}Si compared to $^{\text{nat}}\text{Si}$ due to the shift in bandgap [77]. Background features for boron and oxygen were accounted for by including either a linear component or both a linear component and a sinusoidal component.

We used the conversion factors from Zakel et al. [109] for the carbon and oxygen LVMS and the boron split-off band hole, $2p'$. The conversion factors are peak conversion factors, k , not area conversion factors, f . As such we must use the specified resolution when converting. We measured the spectral region at a resolution of 0.1 cm^{-1} then re-transformed the interferogram to 1 cm^{-1} for the carbon and boron conversion and to 0.5 cm^{-1} for the oxygen conversion.

Additionally, as the isotopic composition of the silicon substrate causes broadening (see 2.3.1) the appropriate conversion factor, $k^{28\text{Si}}$ or k^{natSi} must be used. Zakel et al. [109] provide conversion factors for both $^{\text{nat}}\text{Si}$ and ^{28}Si for all these spectral lines except boron in natural silicon, $k_{\text{B}}^{\text{natSi}}$. To determine $k_{\text{B}}^{\text{natSi}}$ we compared the max absorption coefficient, $\bar{\alpha}_{\text{max}}$, and integrated area, $\int \bar{\alpha} d\nu$, of the boron $2p'$ line in a bare ^{28}Si IB wafer and a bare $^{\text{nat}}\text{Si}$ HB wafer. We obtained

$$k_{\text{B}}^{\text{natSi}} = \frac{\bar{\alpha}_{\text{max}}^{28} \int \bar{\alpha}^{\text{nat}} d\nu}{\bar{\alpha}_{\text{max}}^{\text{nat}} \int \bar{\alpha}^{28} d\nu} k_{\text{B}}^{28\text{Si}} = (3.6 \pm 0.5) \times 10^{14}\text{ cm}^{-2}. \quad (4.1)$$

This peak conversion factor is valid for a 1 cm^{-1} resolution. This value is within error of $k_{\text{B}}^{28\text{Si}} = (3.5 \pm 0.5) \times 10^{14} \text{ cm}^{-2}$ given by Zakel et al. [109] indicating that isotopic broadening is not the dominate broadening mechanism of this line.

The boron $2p'$ of the LB samples ($w^{28}\text{Si}:^{77}\text{Se}:\text{LB}$, $w^{28}\text{Si}:^{78}\text{Se}:\text{LB}$, $^{28}\text{Si}:^{77}\text{Se}:\text{LB}$) was too weak to resolve in the absorption spectra. Instead the boron concentration was taken from Devyatykh et al. [100]. Measured impurity concentrations for all samples are shown in Tab. 4.1.

In absorption we detect oxygen and carbon in nearly all samples after diffusion, with no evidence before diffusion. The oxygen is introduced into the wafer samples due to diffusing with SeO_2 . The oxygen in the block samples could be coming from outdiffusion of the quartz ampules at the high diffusion temperature. The carbon could be due to contamination at some point in the diffusion process, possibly from residual acetone used during the pre-cleaning process.

Sample	[B] (cm^{-3})	[O] (cm^{-3})	[C] (cm^{-3})	Other
$w^{\text{nat}}\text{Si}:^{77}\text{Se}:\text{HB}$	$(4.7 \pm 0.7) \times 10^{15}$	$(2.25 \pm 0.19) \times 10^{17}$	$(1.8 \pm 0.2) \times 10^{16}$	(Ga, As)*
$w^{28}\text{Si}:^{77}\text{Se}:\text{IB}$	$(5.9 \pm 0.8) \times 10^{14}$	$(2.5 \pm 0.2) \times 10^{17}$	$(2.6 \pm 0.2) \times 10^{16}$	Ga, As
$w^{28}\text{Si}:^{77}\text{Se}:\text{LB}$	$(4.5 \pm 1.0) \times 10^{13}\dagger$	$(3.0 \pm 0.2) \times 10^{17}$	$(3.0 \pm 0.2) \times 10^{16}$	Ga, As
$w^{\text{nat}}\text{Si}:^{78}\text{Se}:\text{HB}$	$(4.7 \pm 0.7) \times 10^{15}$	$(2.4 \pm 0.2) \times 10^{17}$	$(1.43 \pm 0.18) \times 10^{16}$	(Ga, Al)*
$w^{28}\text{Si}:^{78}\text{Se}:\text{IB}$	$(5.9 \pm 0.8) \times 10^{14}$	$(2.2 \pm 0.2) \times 10^{17}$	$(1.1 \pm 0.4) \times 10^{16}$	Ga, Al
$w^{28}\text{Si}:^{78}\text{Se}:\text{LB}$	$(4.5 \pm 1.0) \times 10^{13}\dagger$	$(2.7 \pm 0.2) \times 10^{17}$	$(1.9 \pm 0.4) \times 10^{16}$	Ga, Al
$w^{\text{nat}}\text{Si}:\text{nat}\text{Se}:\text{HB}$	$(4.7 \pm 0.7) \times 10^{15}$	$(2.26 \pm 0.20) \times 10^{17}$	$(1.26 \pm 0.10) \times 10^{17}$	–
$^{28}\text{Si}:^{77}\text{Se}:\text{LB}$	$(4.5 \pm 1.0) \times 10^{13}$	$(2.4 \pm 0.2) \times 10^{16}$	$< 2 \times 10^{15}$	–
$^{28}\text{Si}:^{78}\text{Se}:\text{IB}$	$(1.32 \pm 0.19) \times 10^{15}$	$(3.5 \pm 0.3) \times 10^{16}$	$(5.0 \pm 0.3) \times 10^{15}$	–
$^{28}\text{Si}:^{77}\text{Se}:\text{IB}$	$(1.32 \pm 0.19) \times 10^{15}$	$(3.3 \pm 0.3) \times 10^{16}$	$(4.7 \pm 0.3) \times 10^{15}$	–

Table 4.1: The boron, oxygen, and carbon concentrations of the samples studied in this paper. Impurities identified from photoluminescence spectra are also shown. Samples grouped together are from the same ampule. Impurities marked with an * were not observed but inferred from spectra of other samples from the same ampule. Concentration values marked with a † are from Devyatykh et al. [100], all other values are determined from absorption spectra features.

4.1.3 Impurities – Profiles

With the exception of boron, all of these impurities were introduced during the diffusion process. The diffusion parameters of all impurities identified in the previous two sections are shown in Tab. 4.2. Shown in Fig. 4.3 are the expected concentration profiles assuming the

impurities are introduced at the solid solubility limit for the entirety of the 7 day, 1200 °C, diffusion.

Based on these diffusion profiles, the expected average concentration for carbon and oxygen in wafer samples are $1 \times 10^{16} \text{ cm}^{-3}$ and $4 \times 10^{17} \text{ cm}^{-3}$ respectively. These values agree well with the measured carbon and oxygen concentrations from the wafer samples meaning both oxygen and carbon were likely introduced close to the solid solubility limit. This was expected for oxygen but was unexpected for carbon, indicating significant contamination.

Although we have no estimate for the concentrations of gallium, arsenic, and aluminum they are probably much lower than the solid solubility. Aluminum, in particular, which we believe to come from cross contamination in Ampule 2 is most likely introduced at a surface concentration of $5 \times 10^{14} \text{ cm}^{-3}$, the concentration of aluminum in $^{\text{nat}}\text{Si}:^{78}\text{Se}:\text{Al}$. The arsenic contamination is likely small as it diffuses only a small amount into the samples much of which was removed during the polish/etch.

The aluminum and gallium contamination is particularly concerning as they are both acceptors, like boron. As we are concerned with the ionized species, Se^+ , more or less acceptors in the samples will change the concentration of Se^+ . This will be discussed further in Sec. 4.2.3.

Impurity	$C_s(1200 \text{ }^\circ\text{C}) (\text{cm}^{-3})$	$D_0 (\text{cm/s})$	$E_a (\text{eV})$
Selenium	6.6×10^{16}	0.123	2.457
Carbon	5.5×10^{16}	6.11	3.293
Oxygen	5.7×10^{17}	0.16	2.529
Aluminum	1.5×10^{19}	0.317	3.023
Gallium	4.7×10^{19}	3.81	3.552
Arsenic	4.4×10^{20}	40.9	3.971

Table 4.2: Diffusion properties of impurities seen in wafer samples. All values from *Intrinsic Point Defects, Impurities, and Their Diffusion in Silicon* [99].

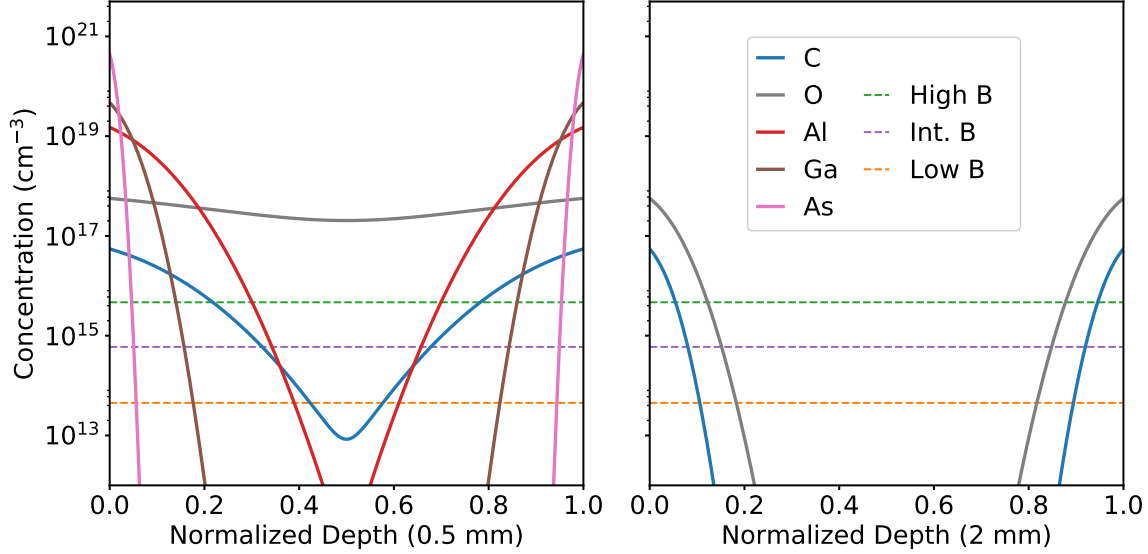


Figure 4.3: Calculated concentration profiles for the impurities introduced during diffusion of (a) a wafer sample, and (b) a block sample. It was seen that all impurities are present in wafer samples, although, Al was only seen in Ampule 2 sample, while only C and O were confirmed to be in the block samples. It is assumed that the impurities are introduced at the solid solubility limit at 1200 °C and diffused for 7 days. The boron levels of the different wafer samples studied are shown as well.

4.2 Se^+ Optical Properties

In this section we present our study of the optical properties of the $\text{Si}:\text{Se}^+$ system through investigation of photoluminescence, absorption, tip-angle, and hole burning measurements.

4.2.1 Se^+ – Photoluminescence

While the zero-phonon line (ZPL) luminescence of the $\text{Se}^+ 1s:T_2 \Rightarrow 1s:A$ transition had been observed before [54] as of yet the phonon sideband had not been observed and thus the ZPL fraction had not been determined. By using a very high power (4 W) above bandgap laser excitation we were able to resolve the phonon sideband, however, the high power resulted in local heating of the sample.

Rather than use the non-resonant above bandgap excitation used to generate luminescence signal in Sec. 4.1.1 we used a resonant pumping scheme. By tuning a laser to the $\text{Se}^+ 1s:A \Rightarrow 2p_{\pm}$ transition (4578 cm^{-1}) [90], electrons were excited to $2p_{\pm}$ and then decayed to $1s:T_2\Gamma_7$ via a phonon cascade. From $1s:T_2\Gamma_7$ we measured the emitted photons as the electron decayed back to the ground state. This resonant pumping scheme produced a sufficiently high luminescent signal to resolve the phonon sideband as there are less decay paths available to the excited electron than a non-resonant pumping scheme.

To perform the measurement we used the FTIR-photoluminescence setup as depicted in Fig. 3.3. A $\text{Cr}^{2+}:\text{ZnS}/\text{Se}$ narrowline tunable laser pumped by an erbium-fiber laser (IPG Photonics) with an output power of 1 W was used as the optical excitation source. A CaF_2 beamsplitter and liquid nitrogen-cooled InSb detector were used. Additionally, a 2440 nm long pass filter was used to filter out stray laser light. We measured the photoluminescence spectra of the $\text{w}^{\text{nat}}\text{Si}:\text{nat}\text{Se}:\text{HB}$ sample.

In Fig. 4.4 we see the photoluminescence spectrum of the $\text{Se}^+ 1s:\text{T}_2\Gamma_7 \Rightarrow 1s:\text{A}$ transition. The resonant zero-phonon line (ZPL) is visible along with the phonon-assisted sideband present at lower energies. This sideband is due to the emission of a photon and one or more phonons as an electron decays back to the ground state. The exact shape of this sideband is determined by the phonon density of states in silicon and strength of the coupling to the different phonon modes. The calculated phonon density of states [112] is shown in the inset of Fig. 4.4. While some features do line up, the system clearly couples to certain phonons preferentially. The broad feature past the edge of the phonon density of states is due to the emission of a photon and multiple phonons.

The ZPL fraction, determined from the ratio of the ZPL line area to the total area, is $15.1 \pm 0.3 \%$. There is the possibility that light emitted in the ZPL line is reabsorbed while still in the sample and then emitted into the sideband. The reverse process – an electron absorbing a lower energy photon and a phonon – has a negligible chance of occurring. Thus, this ZPL fraction is a lower bound.

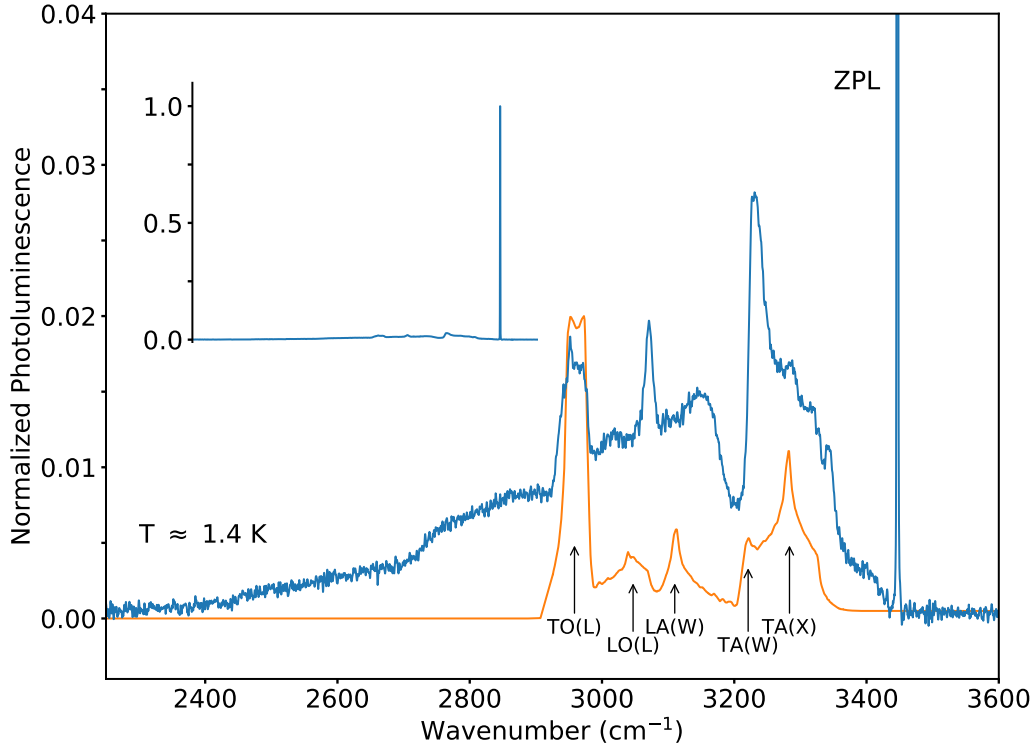


Figure 4.4: The photoluminescence spectrum of the $\text{Se}^+ 1s:T_2\Gamma_7 \Rightarrow 1s:A$ transition measured at a resolution of 1 cm^{-1} . The resonant zero-phonon line is labeled ZPL. The spectrum has been normalized to the ZPL line and is clipped. The phonon sideband is visible to lower energies. (Upper inset) The same spectrum showing the unclipped height of the ZPL. The phonon density of states [112] in silicon is overlaid with the peaks in the distribution labeled by the phonon mode (T/L: transverse/longitudinal, O/A: optic/acoustic) and the direction in the lattice labeled by the symmetry site (L, W, X).

4.2.2 Se^+ – Linewidth

High resolution absorption spectra were obtained for all ^{28}Si samples using the FTIR-absorption setup shown in Fig. 3.3. A KBr beamsplitter and a liquid-nitrogen cooled InSb detector were used. A bandpass filter (130 nm about 2850 nm) placed in front of the detector was also used to increase the signal-to-noise ratio of the measurement. These spectra are shown in Fig. 4.5. The triplet and singlet peaks of the ^{77}Se samples are clearly resolved while the spin-0 ^{78}Se samples have only a single peak.

Despite the same isotopic compositions, the wafer samples are much broader and shifted when compared to the elementally diffused block samples. This is most clear for ^{77}Se samples which also show some difference between two elementally diffused samples.

The ^{78}Se samples have the same trend, the wafer samples are broader and shifted in energy. The $^{28}\text{Si}:^{78}\text{Se}:\text{IB}$ sample had near 100 % absorption at high resolution so instead we show a lower resolution spectra to illustrate the peak energy. To compare linewidth we show the ^{80}Se line visible in the $^{28}\text{Si}:^{78}\text{Se}:\text{IB}$ sample from residual ^{80}Se .

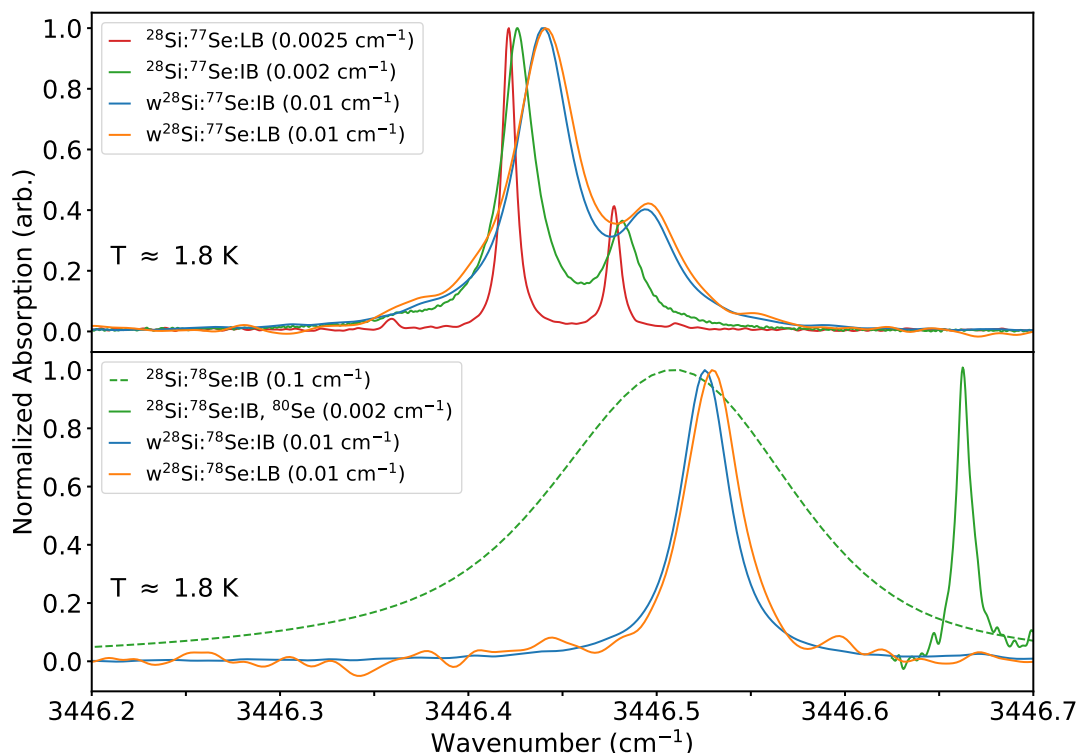


Figure 4.5: High resolution scans of the $\text{Se}^+ 1s:A \Rightarrow 1s:T_2\Gamma_7$ for all ^{28}Si samples. The different peak positions and linewidths are due to different $[\text{O}]$ (see Fig. 4.6). The $^{28}\text{Si}:^{78}\text{Se}:\text{IB}$ sample had zero transmission at the peak for high resolution scans so we instead show a low resolution scan to show the peak position and the high resolution scan of the ^{80}Se $1s:A \Rightarrow 1s:T_2\Gamma_7$ in the same sample to compare linewidth. The resolution used for each spectra is listed in the legends.

The linewidths and peak energies (extracted via fits to Eqn. 3.10) were found to depend linearly on the concentration of oxygen as seen in Fig. 4.6 (we ignore carbon as $[\text{C}] \ll [\text{O}]$ for all samples investigated). The dependence with $[\text{O}]$ for the linewidth, $d\nu$, for all isotopes, and the peak energy of ^{77}Se , $\nu_{\text{max},77}$, and ^{78}Se , $\nu_{\text{max},78}$, were found have the following

dependencies:

$$d\nu = (0.00590 \pm 0.00007) \text{ cm}^{-1} + (0.01123 \pm 0.00011) \frac{\text{cm}^{-1}}{[\text{O}]/10^{17}}$$

$$\nu_{\text{max},77} = (3446.4194 \pm 0.0002) \text{ cm}^{-1} + (0.0080 \pm 0.0005) \frac{\text{cm}^{-1}}{[\text{O}]/10^{17}}$$

$$\nu_{\text{max},78} = (3446.5068 \pm 0.0003) \text{ cm}^{-1} + (0.00860 \pm 0.00013) \frac{\text{cm}^{-1}}{[\text{O}]/10^{17}}$$

In units of eV:

$$d\nu = (0.731 \pm 0.008) \text{ } \mu\text{eV} + (1.392 \pm 0.013) \frac{\mu\text{eV}}{[\text{O}]/10^{17}}$$

$$\nu_{\text{max},77} = (427.28708 \pm 0.00003) \text{ meV} + (0.99 \pm 0.06) \frac{\mu\text{eV}}{[\text{O}]/10^{17}}$$

$$\nu_{\text{max},78} = (427.29792 \pm 0.00003) \text{ meV} + (1.066 \pm 0.016) \frac{\mu\text{eV}}{[\text{O}]/10^{17}}$$

These fits exclude the data point from sample $^{28}\text{Si}:^{77}\text{Se}:\text{IB}$, marked with an arrow in Fig. 4.6. This sample did not appear to fit the same trend as all the other samples, possibly due to the more complicated two part diffusion process (See Sec. 3.1). There could also be other broadening mechanisms present in only this sample such as strain or Stark broadening.

Electrically neutral impurities like oxygen and carbon are expected to cause broadening and an energy shift due to random strain [113, 114]. The magnitudes of both the broadening and energy shift are expected to scale linearly with concentration [113]. The broadening is expected to scale as $\sim e^2 a^2 N$ (in CGS units) [114, 115], where e is the electron charge, a is the lattice constant, and N is the concentration of electrically neutral impurities. This gives an expected slope of $0.03 \frac{\text{cm}^{-1}}{N/10^{17}}$, or $4 \frac{\mu\text{eV}}{N/10^{17}}$, which is close to the value we measure. Additionally, both $\nu_{\text{max},77}$ and $\nu_{\text{max},78}$ have nearly identical dependencies with $[\text{O}]$ indicating that the mechanism causing the shifts acts on both isotopes of selenium equally.

From these trends we can extrapolate to the case of an ideal sample with no impurities. In this case the peak position for a ^{77}Se sample (triplet peak) would be $3446.4194 \pm 0.0002 \text{ cm}^{-1}$ ($427.28708 \pm 0.00003 \text{ meV}$) and the peak position for a ^{78}Se sample would be $3446.5068 \pm 0.0003 \text{ cm}^{-1}$ ($427.29792 \pm 0.00003 \text{ meV}$). In both cases the linewidth would be $0.00590 \pm 0.00007 \text{ cm}^{-1}$ ($0.731 \pm 0.008 \text{ } \mu\text{eV}$). If the impurities are the only broadening mechanism then this ideal linewidth would be the homogeneous lifetime-limited linewidth. From Eqn. 2.23 this would suggest a bound on the excited state lifetime, $\tau_{\text{exc}} > 0.900 \pm 0.010 \text{ ns}$.

This indicates a clear downside of using SeO_2 for diffusion. While it protects the surface of the sample (at least in some instances) the oxygen introduced is detrimental to the optical properties. However, despite this fact there still is remarkable homogeneity across all samples.

An important issue to be addressed is that only the wafer samples were expected to have a (nearly) uniform oxygen concentration (see Fig. 4.3). In the block samples the [O] in the local environment about the Se^+ was higher than the average [O] determined by absorption measurements due to the average being lower by the large regions with no oxygen content. Thus the [O] determined are lower bounds for the three block samples studied.

In Fig. 4.6 the block samples are the three points at the lowest [O]. The two block sample points included in the fit have a large effect on the outcome of the linear fit as the remaining points are clustered together and have larger error bars. Thus, the extracted [O] dependence of linewidth and peak position are lower bounds, and the extrapolated linewidth and peak positions at [O] = 0 are upper bounds.

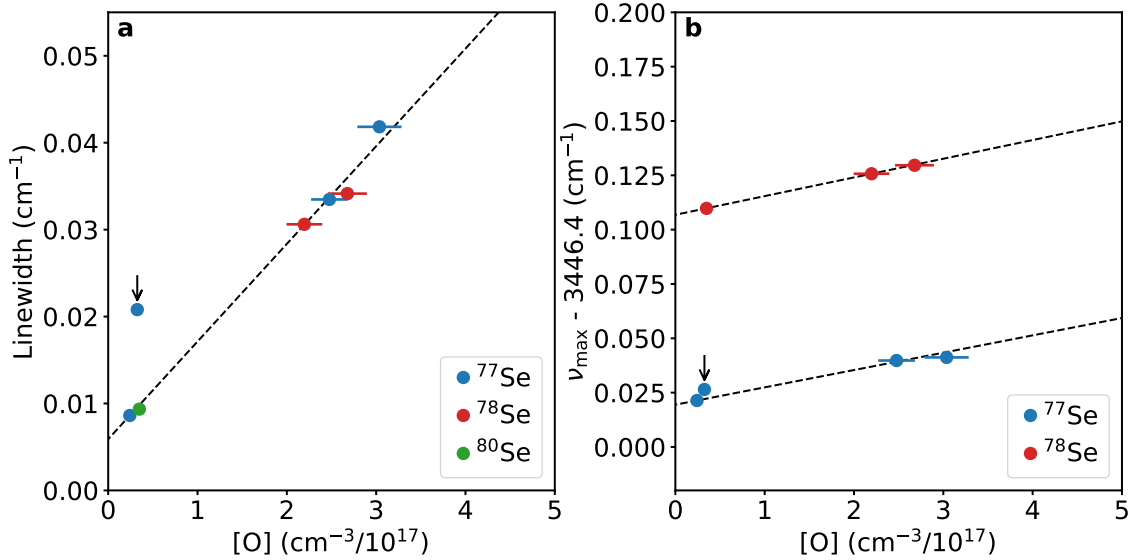


Figure 4.6: (a) Linewidth of the Se^+ $1s:A \Rightarrow 1s:T_2\Gamma_7$ transition versus [O] for all ^{28}Si samples, fit with a line. The selenium isotope of the transition is indicated. (b) The peak energy of the Se^+ $1s:A \Rightarrow 1s:T_2\Gamma_7$ transition versus [O] for all ^{28}Si samples. The two selenium isotopes studied are fit separately. In both (a) and (b) the data corresponding to the $^{28}\text{Si}:^{77}\text{Se}:\text{IB}$ sample are marked with an arrow. These data points are excluded from the fits.

4.2.3 Se^+ – Transition Dipole Moment

From Eqn. 2.20 the transition dipole moment depends on the concentration of Se^+ and the area of the absorption coefficient spectral line. To this end we measured the absorption spectra of the Se^+ $1s:A \Rightarrow 1s:T_2\Gamma_7$ for all wafer samples made, shown in Fig. 4.7. As we only need the area of the spectral line and FTIR spectroscopy is area conserving regardless of resolution, we worked at a lower resolution than previous measurements to obtain a higher signal to noise ratio. Measurements were performed with a KBr beamsplitter and a

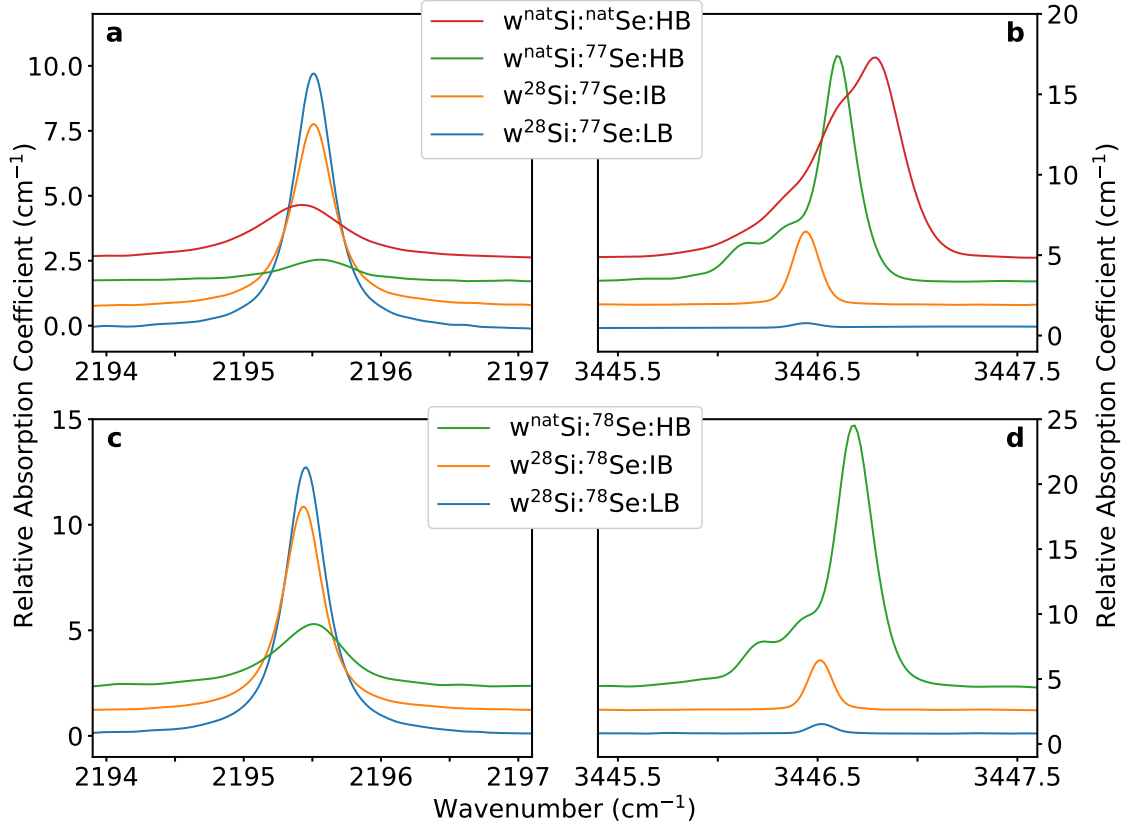


Figure 4.7: Absorption spectra of all wafer samples showing the (a) $^{77}\text{Se}^0$ $1s:A \Rightarrow 1s:T_2$, (b) $^{77}\text{Se}^+$ $1s:A \Rightarrow 1s:T_2\Gamma_7$, (c) $^{78}\text{Se}^0$ $1s:A \Rightarrow 1s:T_2$, and (d) $^{78}\text{Se}^+$ $1s:A \Rightarrow 1s:T_2\Gamma_7$ transitions for the wafer samples. The different lineshapes and absorption strengths are due to the different isotopic combinations and the different boron concentrations. Higher [B] samples have stronger Se^+ transitions and weaker Se^0 transitions, and vice-versa for lower [B] samples. All spectra were measured at 1.8 K at a resolution of 0.1 cm^{-1} .

liquid-nitrogen cooled MCT detector. We only considered the wafer samples as these were the only samples confirmed to be fully compensated with near-uniform [Se].

For these samples we estimate $[\text{Se}^+]$ from the measured [B]. We make the assumption that each boron acceptor in the samples creates one singly ionized selenium, ie., $[\text{Se}^+] = [\text{B}]$. Note that this gives an upper bound on $[\text{Se}^+]$ as there could be doubly ionized selenium, Se^{2+} , or selenium pairs which also act as double donors [90]. Furthermore, as discussed in Sec. 4.1.3, gallium and aluminum impurities have been introduced during diffusion. As both Ga and As are acceptors in silicon, their presence would increase $[\text{Se}^+]$, however, we assume that their concentrations are low enough that they will be negligible compared to the boron concentration. We will revisit this assumption below.

Calculated values for the transition dipole moment, μ , of the Se^+ $1s:A \Rightarrow 1s:T_2\Gamma_7$ transition are shown in Fig. 4.8. For this calculation we used the area extracted from fits to

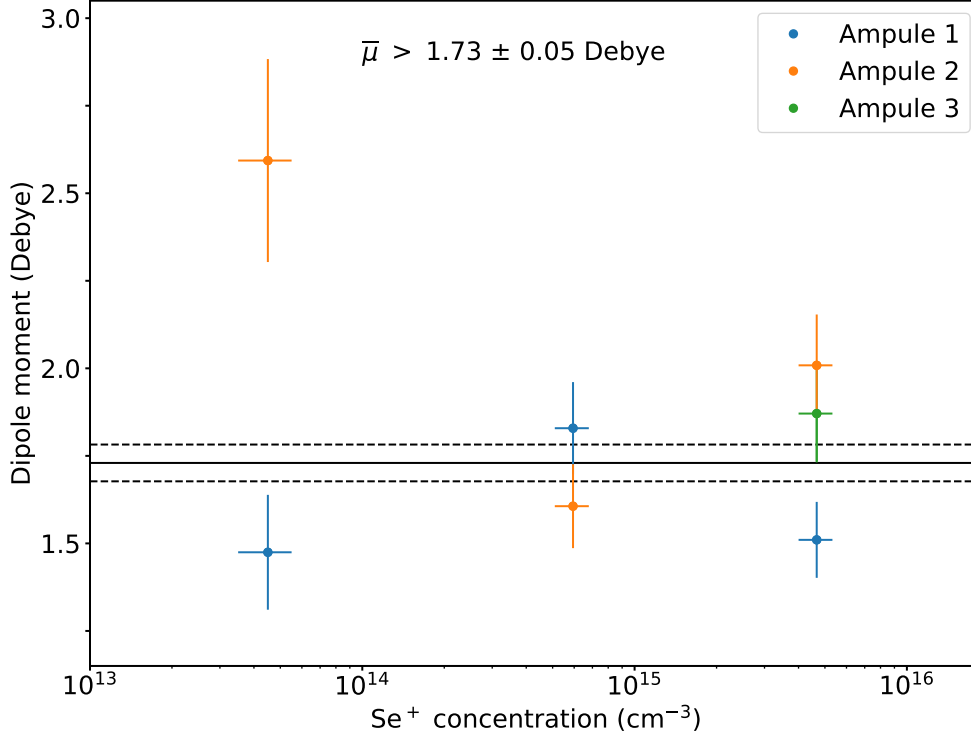


Figure 4.8: Transition dipole moment, μ , for all wafer samples using the estimate $[\text{Se}^+] = [\text{B}]$. The average transition dipole moment is 1.73 ± 0.05 Debye which is a lower bound (see text). The points are coloured based on which ampule the sample was from.

Eqn. 3.10 of the $1s:A \Rightarrow 1s:T_2\Gamma_7$ transition spectra shown in Fig. 4.7. We used $g_2 = g_1$ as both $1s:A$ and $1s:T_2\Gamma_7$ have two electronic states [89], $\epsilon_r = 11.56$, and $n = 3.4$ [116]. The average transition dipole moment over all seven wafer samples is 1.73 ± 0.05 Debye. As the Se^+ concentration values are upper bounds and $\mu \propto 1/[\text{Se}^+]$, the transition dipole moment calculated is a lower bound.

With the exception of the outlier at the lowest $[\text{Se}^+]$ level there is good agreement over three orders of magnitude. This suggests that our assumption that the gallium concentration is much lower than the boron concentration is valid. If this were not the case we would see a clear trend across the different levels of boron as the fractional change in acceptor level relative to the boron level would be drastically different.

On the other hand the aluminum present could be the reason for the outlier at the lowest $[\text{Se}^+]$ level in Fig. 4.8. This sample is $w^{28}\text{Si}:^{78}\text{Se}:LB$. If the aluminum were introduced at a concentration of $5 \times 10^{14} \text{ cm}^{-3}$ (the concentration present in $^{nat}\text{Si}:^{78}\text{Se}:Al$) then the change in acceptors would only be non-negligible for the lowest boron sample, namely,

w²⁸Si:⁷⁸Se:LB. In this case the [Se⁺] is higher than expected from only the boron and thus the calculated μ is higher than the actual value.

4.2.4 Se⁺ – Tip-Angle

As mentioned, the transition dipole moment value obtained in the previous section is likely a lower bound based on the fact that some selenium may become doubly ionized, or selenium pairs may be ionizing. To get a direct measurement of [Se⁺] we performed a tip-angle measurement.

However, we cannot obtain a measurement for all samples. First off, all ⁷⁸Se samples cannot be measured as there is no resolvable splitting in the absorption spectra at Earth’s magnetic field with which to optically hyperpolarize the spin population (See Fig. 4.5 b). Secondly, we do not expect the ^{nat}Si samples to be suitable. In principle, a subset of centers in ^{nat}Si:⁷⁷Se could be initialized by burning a hole in the large absorption linewidth [117]. However, the presence of ²⁹Si is likely a dominant factor in the magnetic field fluctuations [118] rather than that from instantaneous diffusion. Furthermore, the tip-angle measurement relies upon addressing all spins with the applied RF pulse. We expect the spread of transition frequencies in ^{nat}Si would be too high to address all spins simultaneously.

Finally, as the tip-angle measurement is inherently a low signal-to-noise experiment, we expect the low boron samples to have insufficient Se⁺ to provide high enough signal to noise. This leaves the w²⁸Si:⁷⁷Se:IB sample as the most suitable for a tip-angle measurement.

To increase the signal we cleaved the w²⁸Si:⁷⁷Se:IB sample in half and stacked the pieces within the resonator with faces normal to the applied laser using the setup shown in Fig. 3.4 a. With a chopper modulating the laser a lock-in measurement was made as the laser was scanned across the Se⁺ 1s:A \Rightarrow 1s:T₂Γ₇ transition. For this scan the laser power was set very low using ND filters to have negligible optical pumping as the laser was scanned across the transition. The transmission spectrum is shown in Fig. 4.9 a. The laser wavelength was then set to the peak of the 1s:A:T \Rightarrow 1s:T₂Γ₇ transition for the remainder of the experiment.

To perform the RF scan we increased the laser power substantially to ensure the system was hyperpolarized to the singlet state. The RF frequency applied to the resonator was swept over the S \Leftrightarrow T₋, T₀, T₊ transitions. As the RF magnetic field moves population from S to the triplet states the laser transmission decreases as transitions from T \Rightarrow 1s:T₂Γ₇ are driven. A small static magnetic field (\approx 1 G) is applied perpendicular to the axis of the RF magnetic field to split the three transitions. The magnetic resonance spectrum is shown in Fig. 4.9 b. The magnitude of the magnetic field is determined from the splitting between the S \Leftrightarrow T₀ and S \Leftrightarrow T₊ transitions and the fact that $\partial\nu/\partial B = 0$ and 14.036 GHz/T for the S \Leftrightarrow T₀ and S \Leftrightarrow T₊ transitions respectively [55, 54].

The tip-angle measurement requires $\partial\nu/\partial B > 0$ in order to observe the instantaneous diffusion decoherence effect. Thus, rather than use S \Leftrightarrow T₀, the qubit transition studied by

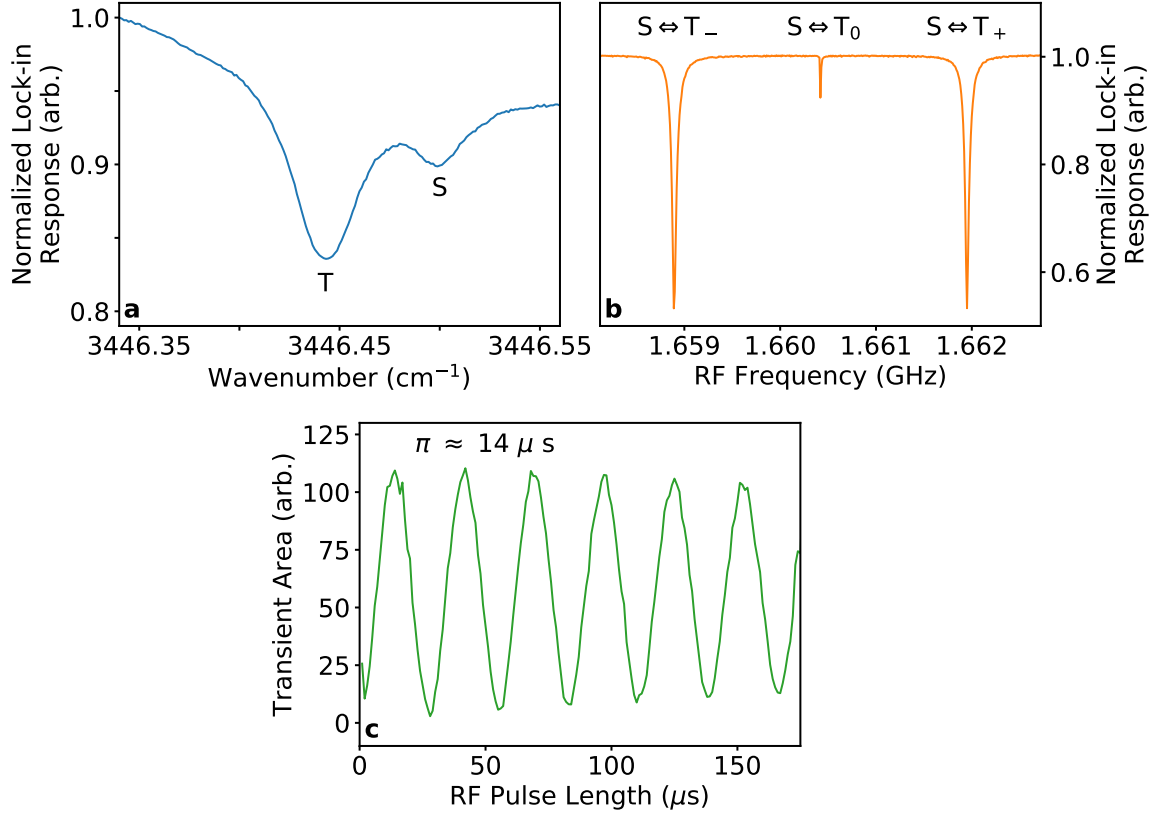


Figure 4.9: (a) Laser scan of the $^{77}\text{Se}^+ 1s:A \Rightarrow 1s:T_2\Gamma_7$ transition of the $w^{28}\text{Si}:^{77}\text{Se}:\text{IB}$ sample. (b) RF scan of the singlet to triplet transitions of the $w^{28}\text{Si}:^{77}\text{Se}:\text{IB}$ sample with the laser tuned to the triplet peak. (c) Rabi pulse of the $S \Leftrightarrow T_+$ transition. In this instance the time to rotate the spins by π radians was measured to be $14 \mu\text{s}$.

Morse et al. [54], we use the $S \Leftrightarrow T_+$ transition. We set the RF frequency to this transition for the remainder of the experiment.

With the laser and RF frequencies set we switched the setup to the pulsed RF setup shown in Fig. 3.3 b. We began by performing a Rabi pulse sequence to determine the conversion from pulse length to rotation angle. This measurement was repeated every day as the power coupling into the sample was not steady from day to day. The RF power was adjusted if necessary to have the the π length $\approx 14 \mu\text{s}$. The Rabi pulse sequence response is shown in Fig. 4.9 c. The signal is given by the laser transient area as explained in Sec. 3.3.

Finally, tip-angle measurements were obtained at a number of different refocusing pulse angles. To account for drift in the experimental conditions (B_0 , laser frequency, etc.) the transient area was measured relative to a fully decoherent transient. Specifically, after every transient measurement another pulse sequence was applied that consisted of only the initial $\pi/2$ pulse of the tip-angle pulse sequence. After the same dark time the transient is measured to provide the baseline transient of a completely decoherent collection of spins,

dephased from T_2^* (the 50 % polarization shown in Fig. 3.5). Subtracting this baseline from measurements made with refocusing allows the measurement to be insensitive to background drift as well as show a clear decay to 0 rather than to an arbitrary value. These two pulse sequences are shown in the inset of Fig. 4.10.

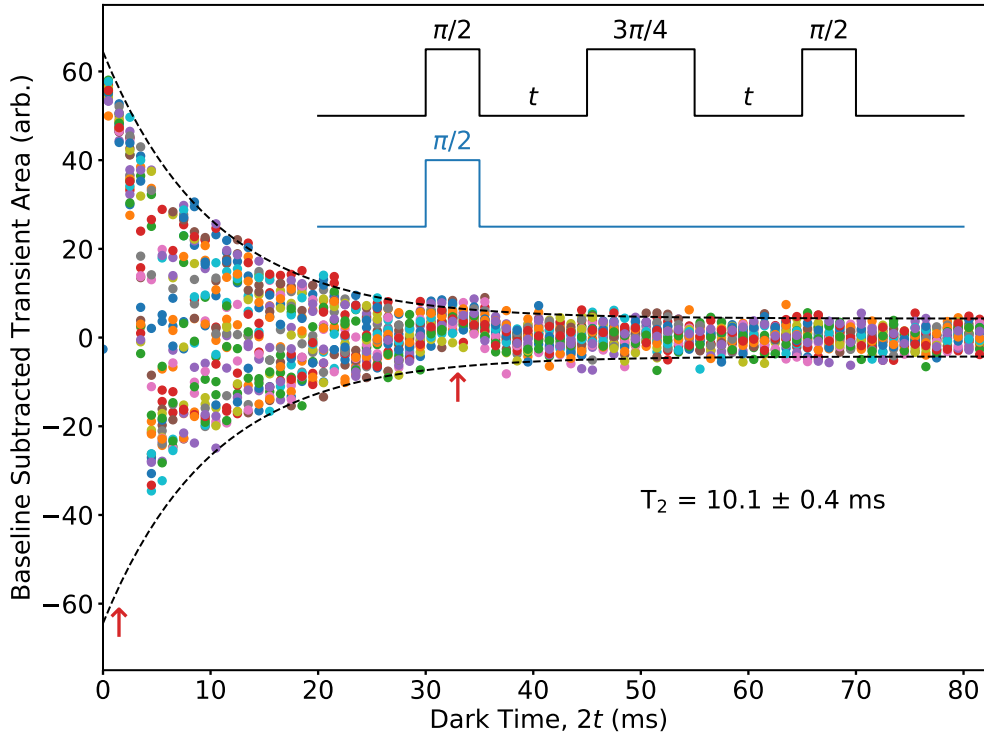


Figure 4.10: Repeated measurements of a $3\pi/4$ tip-angle pulse sequence (black inset). The baseline subtracted transient area was determined by taking the difference of back to back measurements at a given dark time, one using the black inset pulse sequence, and one using the blue inset blue sequence. The blue inset pulse sequence gives a measure of the decoherent baseline (see text). Using maximum magnitude at each dark time the envelope was fit to an exponential with time constant, $T_2 = 10.1 \pm 0.4$ ms. This envelope is mirrored about the y-axis to show the expected minimum magnitude envelope. The drops in phase noise are indicated by red arrows at ≈ 0 and ≈ 33 ms.

As $\partial\nu/\partial B > 0$, if the global magnetic environment is changing on the timescale of an applied pulse sequence then the average resonant frequency can change between the first and last pulse. This leads to phase noise [119], an accumulation of phase between the applied RF frequency and the central transition frequency of the entire spin ensemble. The result is that the final pulse, meant to rotate the state back to the T_+ state for read out will instead rotate the state to a random point on the Bloch sphere. If the phase noise is large, the average over multiple measurements will be zero. Thus, rather than averaging over multiple

measurements, the maximum magnitude [119] of all measurements at each dark time was taken. This selects only those instances where the phase mismatch was zero.

Fig. 4.10 shows the result of many measurements at the tip-angle pulse sequence of $\theta = 4\pi/3$. The maximum magnitude at each dark time is fit with a decaying exponential to account for the phase noise. The envelope is asymmetric at ≈ 0 ms and ≈ 33 ms. The asymmetry is expected at dark times lower than T_2^* as below the dephasing time the central transition frequency is always close to the applied RF frequency. Beyond this we expect a symmetric envelope for all dark times, however, we see a region of low phase noise at ≈ 33 ms. This could possibly be due to the phase noise being periodic rather than completely random. At certain dark times the phase accumulated before and after the refocusing pulse will cancel out. The frequency of the phase noise minima is 30 Hz which is likely due to rectified 60 Hz power noise affecting the coils.

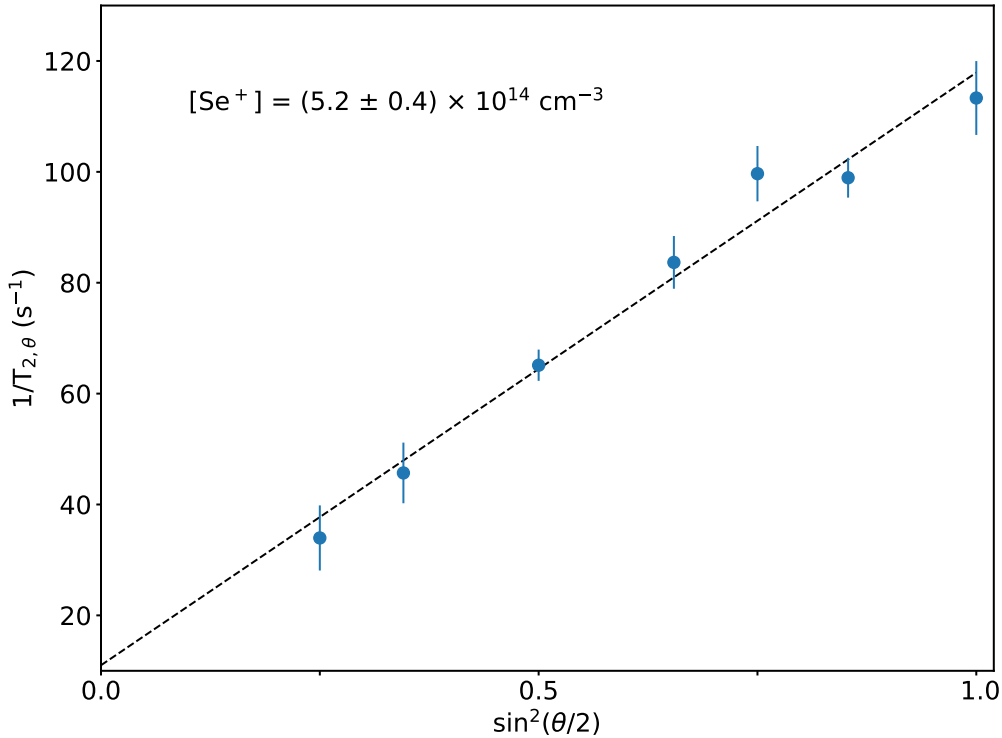


Figure 4.11: Inverse $T_{2,\theta}$ coherence times measured from tip-angle pulse sequences at different angles, θ . The result was fit with a line and the concentration, $[\text{Se}^+] = (5.2 \pm 0.4) \times 10^{14} \text{ cm}^{-3}$ was extracted which is lower than the boron concentration, $[\text{B}] = (5.9 \pm 0.8) \times 10^{14} \text{ cm}^{-3}$.

The tip-angle pulse sequence was repeated at multiple refocusing pulse angles. The inverse $T_{2,\theta}$ values are shown in Fig. 4.11. There is a clear linear response as expected

from Eqn. 2.28. From the fit we extract $[\text{Se}^+] = (5.2 \pm 0.4) \times 10^{14} \text{ cm}^{-3}$ using $\partial\nu/\partial B = 14.036 \text{ GHz/T}$ [55, 54]. As expected, this is lower than that determined by the [B] from Sec. 4.1.2 of $(5.9 \pm 0.8) \times 10^{14} \text{ cm}^{-3}$, although still within error. Using this concentration, the absorption spectrum of $w^{28}\text{Si}:^{77}\text{Se:IB}$ shown in Fig. 4.7 and Eqn. 2.20 we calculate a transition dipole moment of $\mu = 1.96 \pm 0.08 \text{ Debye}$. Again, as expected, this is higher than the lower bound determined in Sec. 4.2.3.

We can also extract the intrinsic Hahn-echo coherence time $T_{2,\text{Int}} = 0.09 \pm 0.04 \text{ s}$. This is much smaller compared to the value measured for the $S \Leftrightarrow T_0$ qubit: $T_2 = 2.14 \pm 0.04 \text{ s}$. This is due to the fact that $\partial\nu/\partial B \approx 0$ for the $S \Leftrightarrow T_0$ transition [54] making it a ‘clock transition’ [86] with much better coherence properties.

4.2.5 Se^+ – Radiative Lifetime and Conversion Factors

The radiative lifetime, as determined by the tip-angle result, is $\tau = 6.0 \pm 0.5 \mu\text{s}$. However, from Sec. 4.2.1 we saw that in addition to the resonant luminescence there is also non-resonant luminescence in the phonon-sideband. Our $\bar{\alpha}$ area measurements only take into account the *resonant* transition. Thus, this radiative lifetime is only the *resonant* radiative lifetime, $\tau_{\text{res}}^{\text{rad}}$. We can determine the lifetime for any radiative emission by taking into account the phonon-sideband – the *total* radiative lifetime, $\tau_{\text{total}}^{\text{rad}}$. The total radiative lifetime is simply the resonant radiative lifetime multiplied by the ZPL fraction: $\tau_{\text{total}}^{\text{rad}} = 0.90 \pm 0.07 \mu\text{s}$.

From Eqn. 2.20 we can determine the area conversion factor, $f_{\text{Se}^+} = (6.2 \pm 0.5) \times 10^{14} \text{ cm}^{-1}$ using $[\text{Se}^+]$ determined from the tip-angle concentration result and the $\bar{\alpha}$ area of the $w^{28}\text{Si}:^{77}\text{Se:IB}$ sample (we used the lower resolution spectra shown in Fig. 4.7 b).

We can further calculate the k_{Se^+} peak conversion factors but these will depend on the exact isotopic combinations, temperature, and resolution of the spectra. Multiplying f_{Se^+} by the ratio $\int \bar{\alpha}(\omega) d\omega / \bar{\alpha}(\omega_{\text{max}})$ we determined k_{Se^+} for all Si and Se isotopic combinations for spectra obtained at 1.8 K and a resolution of 0.1 cm^{-1} . Results from samples with the same isotopic combinations are averaged. These conversion factors are shown in Tab. 4.3.

At a resolution of 0.1 cm^{-1} the splitting due to the hyperfine interaction is unresolved thus we see the same conversion factor for both ^{77}Se and ^{78}Se samples. Furthermore, at this resolution, the broadening effects of oxygen are also unresolved.

Isotopes	k_{Se^+} (cm^{-2})
natSi:natSe	$(3.4 \pm 0.4) \times 10^{14}$
natSi: ^{77}Se	$(2.0 \pm 0.2) \times 10^{14}$
natSi: ^{78}Se	$(2.4 \pm 0.3) \times 10^{14}$
^{28}Si : ^{77}Se	$(1.06 \pm 0.09) \times 10^{14}$
^{28}Si : ^{78}Se	$(1.06 \pm 0.09) \times 10^{14}$

Table 4.3: The conversion factors to convert from peak absorption coefficient of the $1s:A \Rightarrow 1s:T_2\Gamma_7$ spectral line to the concentration of Se^+ for the specified isotopic combinations. These values are all calculated at a temperature of 1.8 K and a resolution of 0.1 cm^{-1} .

4.2.6 Se^+ – Hole Burning

Despite the huge improvements in linewidth from working with ^{28}Si , the absorption spectra linewidths are not lifetime limited. From Sec. 4.2.2 even the narrowest linewidth we observed is predicted to still have inhomogeneous broadening due to oxygen. In a perfect sample we would expect a linewidth of $0.00590 \pm 0.00007 \text{ cm}^{-1}$. Furthermore, from the total radiative lifetime determined in Sec. 4.2.5 the homogeneous lifetime-limited linewidth could be as low as $(5.8 \pm 0.5) \times 10^{-6} \text{ cm}^{-1}$ ($0.72 \pm 0.06 \text{ neV}$) if the excited state lifetime equals τ_{total} .

If we can resolve the homogeneous linewidth we will have a bound on the excited state lifetime – which is needed in order to determine the radiative efficiency of the Se^+ $1s:A \Rightarrow 1s:T_2\Gamma_7$ transition. To this end we pursued hole burning as a means of measuring the homogeneous linewidth.

Using the hole burning set up shown in Fig. 3.3 we performed hole burning on the ^{28}Si : ^{77}Se :IB sample measuring the resulting absorption spectra. Measurements were performed using a CaF_2 beamsplitter and a liquid-nitrogen cooled InSb detector with a band-pass filter (130 nm at 2850 nm) after the dewar in the detection arm. A tunable diode laser (Nanoplus) was used to burn the hole.

The laser was tuned to the $1s:A:T \Rightarrow 1s:T_2\Gamma_7$ transition. Population was pumped into the singlet state resulting in a hole in the triplet peak and an ‘anti-hole’ in the singlet state. A comparison of the absorption spectra with and without the laser excitation is shown in Fig. 4.12. By taking the difference we isolate the hole and anti-hole which we can use to determine the homogeneous linewidth. However, the (anti-) hole lineshape will be a convolution of the laser linewidth, the FTIR system’s inherent resolution, and the ‘true’ (anti-) hole. To this end we measured the spectrum of only the laser light, coupled in via the photoluminescence pathway (see Fig. 3.3). The laser lineshape was measured to be a Gaussian with FWHM of $0.00218 \pm 0.00007 \text{ cm}^{-1}$ when measured by the FTIR at the same resolution at which we measured the hole-burning, 0.002 cm^{-1} , the limit of our FTIR system. This lineshape is then the convolution of laser and FTIR response.

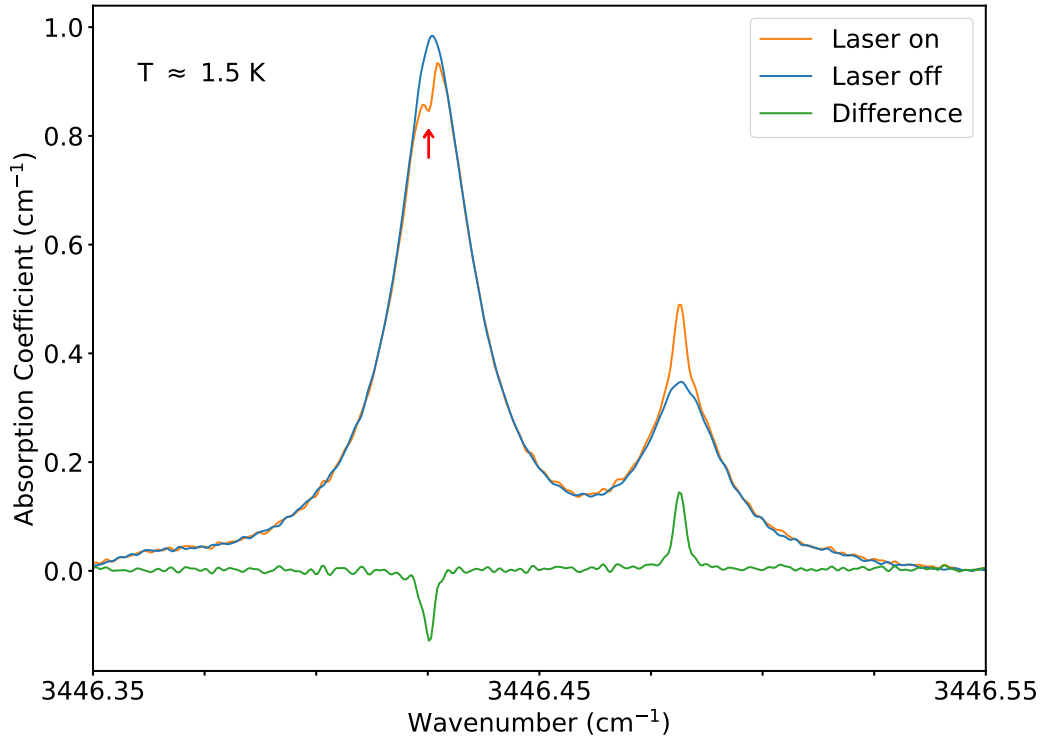


Figure 4.12: Absorption coefficient spectra of the $^{28}\text{Si}:^{77}\text{Se}:\text{IB}$ sample with and without a hole burning laser tuned to the triplet transition (red arrow). The difference is also shown in which the hole and anti-hole are visible. The resolution is 0.002 cm^{-1} .

The hole/anti-hole were fit with a Lorentzian convolved with a Gaussian of linewidth $0.00218 \pm 0.00007\text{ cm}^{-1}$. The extracted Lorentzian linewidth is then twice the homogeneous linewidth (see Eqns. 2.24, 2.25). We determine an upper bound on the homogeneous linewidth of $0.00100 \pm 0.00005\text{ cm}^{-1}$. This value is an upper bound as there could still be power broadening as well as non-static inhomogeneities broadening mechanism (see Sec. 2.3.2). We were at the resolution limit of the FTIR spectrometer and did not expect to be able to resolve the (anti-) hole at lower powers.

This gives a lower bound on the excited state lifetime of $6.8 \pm 0.5\text{ ns}$ from Eqns. 2.22, 2.23. Comparing this value to the radiative lifetime calculated in Sec. 4.2.5, the radiative efficiency of the $\text{Se}^+ 1s:A \Rightarrow 1s:T_2\Gamma_7$ is at least $0.75 \pm 0.08\%$.

This upper bound on the homogeneous linewidth is narrower than the minimum value determined from the [O] dependence. This suggests that there are other inhomogeneous broadening mechanisms still present in the samples other than those due to electrically neutral impurities. This could be due to residual ^{29}Si isotopes, Stark broadening, or random strain fields in the sample.

4.3 Se^0 Optical Properties

Although motivated by an investigation into the optical properties of $\text{Si}:\text{Se}^+$ the samples and measurements made for this work can be used to make estimates of the optical properties of the $1s:A \Leftrightarrow 1s:T_2$ transition of neutral $\text{Si}:\text{Se}^0$. While the $1s:A \Leftrightarrow 1s:^3T_2$ transition is the lowest excited state transition of Se^0 it is very weak except in highly strained samples [91].

Again, we limit the discussion to the wafer samples as only these samples have uniform $[\text{Se}]$. The absorption spectra of the Se^0 $1s:A \Leftrightarrow 1s:T_2$ transition for all wafer samples are shown in Fig. 4.7.

In an ideal, simplified system with $[\text{Se}] > [\text{B}]$ we would have $[\text{Se}^0] = [\text{Se}] - [\text{Se}^+]$. We can define a conversion factor, f_{Se^0} , analogous to f_{Se^+} and rearrange the simple model as $f_{\text{Se}^0} \int \bar{\alpha}_{\text{Se}^0} d\nu = [\text{Se}] - [\text{Se}^+]$. In Fig. 4.13 we plot the absorption coefficient area of the Se^0 $1s:A \Rightarrow 1s:T_2$ transition (determined via fits to Eqn. 3.10) versus $[\text{Se}^+]$ for all wafer samples. $[\text{Se}^+]$ is calculated from the Se^+ $1s:A \Rightarrow 1s:T_2\Gamma_7$ absorption coefficient area (determined via fits to Eqn. 3.10) and the conversion factor, f_{Se^+} , from Sec. 4.2.5.

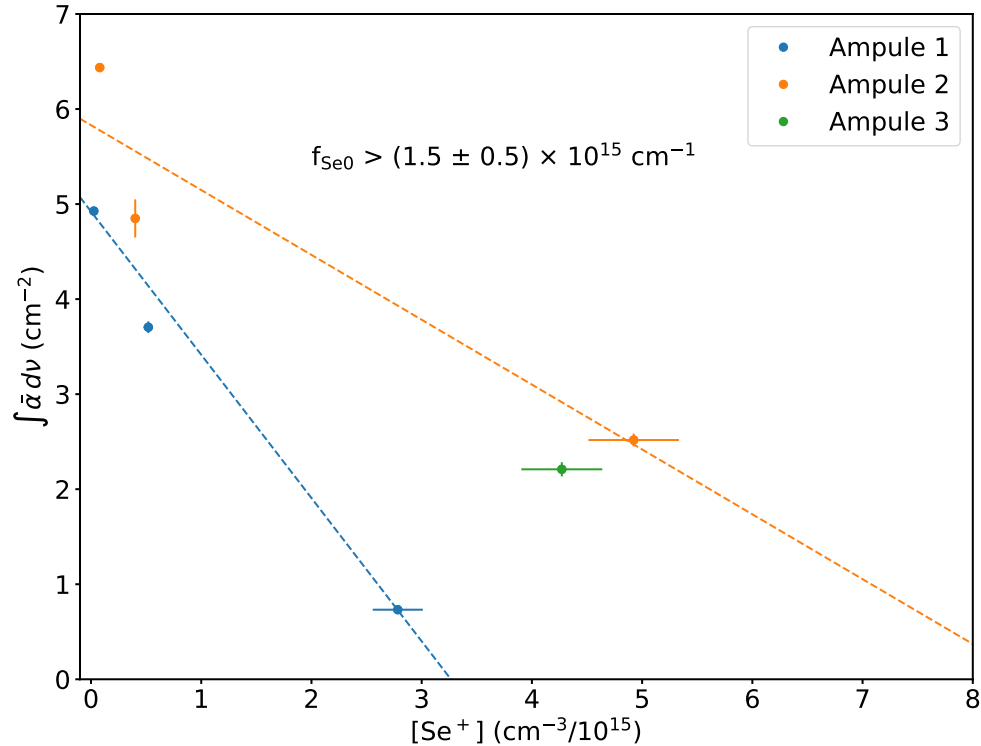


Figure 4.13: Absorption coefficient area of $[\text{Se}^0]$ versus $[\text{Se}^+]$ for all wafer samples studied. The samples from Ampule 1 and Ampule 2 have been fit with a lines separately, dashed blue and dashed orange lines respectively. From the fit to Ampule 2 samples we obtained a lower bound for the Se^0 conversion factor, $f_{\text{Se}^0} > (1.5 \pm 0.5) \times 10^{15} \text{ cm}^{-1}$ (see text).

Isotopes	k_{Se^0} (cm^{-2})
natSi:natSe	$(1.5 \pm 0.6) \times 10^{15}$
natSi: ^{77}Se	$(1.3 \pm 0.5) \times 10^{15}$
natSi: ^{78}Se	$(1.2 \pm 0.5) \times 10^{15}$
^{28}Si : ^{77}Se	$(7.5 \pm 2.0) \times 10^{14}$
^{28}Si : ^{78}Se	$(7.3 \pm 1.9) \times 10^{14}$

Table 4.4: The conversion factors to convert from peak absorption coefficient of the Se^0 1s:A \Rightarrow 1s:T₂ spectral line to the average concentration of Se^0 for the specified isotopic combinations. These values are all calculated at a temperature of 1.8 K and a resolution of 0.1 cm^{-1} .

In Fig. 4.13 we have fit the samples from Ampule 1 and 2 separately to account for the very different diffusion results of the two ampules. From the the y-intercepts (or equivalently the x-intercepts) the total diffused [Se] was higher in Ampule 2 than Ampule 1. This could be due to the SiO_2 layer that formed on samples in Ampule 1 inhibiting diffusion. This SiO_2 layer was absent from Ampule 2 samples. We measure the total diffused selenium for the two ampules to be $[\text{Se}]_{\text{A1}} = (3.27 \pm 0.18) \times 10^{15} \text{ cm}^{-3}$ and $[\text{Se}]_{\text{A2}} = (9 \pm 3) \times 10^{15} \text{ cm}^{-3}$ for Ampules 1 and 2 respectively. In both cases the concentration was much less than that expected from the diffusion parameters, $[\text{Se}]_D = 5 \times 10^{16} \text{ cm}^{-3}$.

The lower than expected [Se] could lead to doubly ionized selenium that would be unaccounted for in this simple model. This would be most apparent in the HB samples, and in particular, the HB sample from Ampule 1 as this sample appears to have $[\text{Se}] < [\text{B}]$. This effect can be seen in the slopes of the fits shown in Fig. 4.13. With lower [Se], the highest boron levels sample from Ampule 1 will have more $[\text{Se}^{2+}]$ leading to steeper slope in Fig. 4.13. As we cannot be sure the same issue is not present in Ampule 2 samples, the magnitude of the slope, $1/f_{\text{Se}^0}$, is an upper bound and thus the conversion factor $f_{\text{Se}^0} > (1.5 \pm 0.5) \times 10^{15} \text{ cm}^{-1}$ is a lower bound.

This leads to lower bound on the radiative lifetime, $\tau_{\text{Se}^0} > 70.0 \pm 25.9 \mu\text{s}$ and an upper bound on the transition dipole moment $\mu_{\text{Se}^0} < 1.1 \pm 0.2$ Debye. These values are calculated using $g_1 = 1$ as the 1s:A state consists only of a spin-singlet. We assume a degeneracy factor of 2 for the 1s:T₂ state based on theoretical calculations by Grossman et al. [75] We use $\epsilon_r = 11.56$, and $n = 3.4$ [116]. The peak conversion factors, k_{Se^0} , for all isotopic combinations are listed in Tab. 4.4 for a resolution of 0.1 cm^{-1} and a temperature of 1.8 K (calculated in the same manner as for k_{Se^+}).

Although it appears that the [Se] diffused into our samples was much less than expected it is important to note that both the LB and IB samples are in the regime $[\text{Se}] > [\text{B}]$. This is important as the tip-angle result for $[\text{Se}^+]$ assumed a near-uniform $[\text{Se}^+]$ which is justified as the tip-angle measurement was performed on an IB sample.

Chapter 5

Conclusion and Future Work

In this work we have presented measurements and results in the determination of the key optical properties of the Si:Se system: both the neutral Se^0 system and the singly-ionized Se^+ system. Our measurements elucidate the key parameters of the Si:Se⁺ spin-photon interface in the ongoing effort to realize Si:Se⁺ based integrated silicon quantum optoelectronics. Silicon samples, both ^{nat}Si and isotopically pure ²⁸Si, were made for the specific purpose of measuring the optical properties via photoluminescence, absorption, and hole burning measurements. Additionally, MR experiments were performed to have an independent determination of μ for a single sample.

5.1 Se^+ Spin-Photon Interface Assessment

The optical properties of the Si:Se⁺ 1s:A \Leftrightarrow 1s:T₂Γ₇ and Si:Se⁰ 1s:A \Leftrightarrow 1s:T₂ transitions determined in this work are summarized in Tab. 5.1. With these values we can now determine (or make estimates towards) the viability of the quantum computing platforms proposed by Morse et al. (outlined in Sec. 2.5.1).

In order to use a coupled cavity-qubit system for qubit readout or entanglement generation the splitting when in the coupled state must be resolvable. When in the coupled state the cavity transmission will show a dip when on resonance determined by the coupling cooperativity [20]:

$$C = \frac{4g^2}{\kappa\Delta\omega_{\text{hom}}} = \frac{2\mu^2}{\hbar\epsilon_0\epsilon_r\Delta\omega_{\text{hom}}} \frac{Q}{V} \quad (5.1)$$

where $\Delta\omega_{\text{hom}}$ is the homogeneous linewidth of the Se^+ 1s:A \Rightarrow 1s:T₂Γ₇ transition, g is the cavity-atom coupling constant (Eqn. 2.31) and κ is the cavity linewidth, $\kappa = \omega_c/Q$, where Q is the quality factor of the cavity. The normalized transmission on resonance is [20, 120]

$$T = \frac{1}{(1+C)^2}. \quad (5.2)$$

At a cooperativity $C = 1$, the splitting is well resolved with the on-resonance transmission dropping to 25 % when the qubit is in the coupled state. To reach this threshold for

	Se ⁰ 1s:A \Leftrightarrow 1s:T ₂	Se ⁺ 1s:A \Leftrightarrow 1s:T ₂ Γ ₇
μ (Debye)	$<1.1 \pm 0.2$	1.96 ± 0.08
f (cm ⁻¹)	$>(1.5 \pm 0.5) \times 10^{15}$	$(6.2 \pm 0.5) \times 10^{14}$
$\tau_{\text{res}}^{\text{rad}}$ (μs)	$>70.0 \pm 25.9$	6.0 ± 0.5
$\tau_{\text{total}}^{\text{rad}}$ (μs)	–	0.90 ± 0.07
τ_{exc} (μs)	–	$>(6.8 \pm 0.5) \times 10^{-3}$
ZPL fraction	–	$> 15.1 \pm 0.3$
$(\tau_{\text{total}}^{\text{rad}}/\tau_{\text{res}}^{\text{rad}})$ (%)	–	–
radiative efficiency	–	$> 0.75 \pm 0.08$
$(\tau_{\text{exc}}/\tau_{\text{total}}^{\text{rad}})$ (%)	–	–

Table 5.1: Optical properties of the Si:Se system determined in this work. μ is the transition dipole moment, f is the area conversion factor, $\tau_{\text{res}}^{\text{rad}}$ is the resonant radiative lifetime, $\tau_{\text{total}}^{\text{rad}}$ is the total radiative lifetime, and τ_{exc} is the excited state lifetime.

the Si:Se⁺ system, using $\mu = 1.96 \pm 0.08$ Debye and the upper bound on the homogeneous linewidth $\Delta\omega_{\text{hom}} = 2\pi \times 29$ MHz, the cavity must satisfy:

$$\frac{Q}{\bar{V}} > 1.4 \times 10^4 \quad (5.3)$$

where \bar{V} is the ratio $V/(\lambda/n)^3$. Increasing Q/\bar{V} will increase the transmission dip and thus the resolvability between the coupled and detuned qubit states.

Although mid-infrared silicon photonics is still a new area of research (see Mashanovich [121] and references therein for examples of recent work), this requirement already appears to be technologically feasible. Early mid-infrared, on-chip photonic cavity designs with $\bar{V} \approx 1$ have been simulated to have $Q \approx 7 \times 10^4$ at $\lambda = 4.4 \mu\text{m}$ and a fabricated device was measured to have $Q \approx 1 \times 10^4$ [94]. At the more commonly studied telecommunication wavelength, 1450-1650 nm, the results are even more encouraging: with fabricated cavities possessing Q and \bar{V} values of $Q \approx 10^5$, $\bar{V} \approx 0.6$ [122]; $Q \approx 10^6$, $\bar{V} \approx 1$ [60]; and $Q \approx 10^7$, $\bar{V} \approx 3$ [123]. Thus a cavity coupling scheme is viable although future work will need to be done to transfer over the telecommunication designs to work at the wavelength of interest, 2.9 μm .

While the ultra sharp lines of the Se⁺ 1s:A \Rightarrow 1s:T₂Γ₇ had been seen previously (1 μeV [55, 54]) we have shown that even narrower linewidths are possible simply by lowering the oxygen contamination (0.7 μeV). Further still, the lifetime-limited linewidth is lower than 0.12 μeV . Additionally, despite very different diffusion conditions and impurity concentrations the difference in resonance frequency is only $\approx 4 \mu\text{eV}$ at most. This excellent

homogeneity is very promising for any device manufacturing as cavity-qubit matching will require only minimal tuning.

This homogeneity is equally important when operating in a luminescence mode, as many entanglement schemes require the emitted photons of qubits to be indistinguishable. This is further complimented by the relatively high zero-phonon line fraction ($> 15.1 \pm 0.3$ %). Nitrogen-vacancy centers have a ZPL fraction of only 4 % [124] and yet have had great success in exploiting their emission for entanglement [24].

The low radiative efficiency measured, 0.75 ± 0.08 , is not encouraging for use of the Si:Se⁺ spin-photon interface in emission. However, this is a lower bound, the actual radiative efficiency might be high enough for efficient entanglement generation in luminescence. Further work will need to be done to either resolve the homogeneous lifetime-limited linewidth or else directly measure the excited state lifetime. Nevertheless, a low radiative efficiency can be compensated by using photonic cavities to enhance the radiative efficiency via the Purcell effect [125]. The enhancement is determined by the Purcell factor [125, 126]

$$F_P = \frac{\tau_{\text{free}}}{\tau_{\text{cav}}} = \frac{3}{4\pi^2} \frac{Q}{\bar{V}}. \quad (5.4)$$

Where τ_{free} and τ_{cav} are the radiative lifetimes of a free center (ie. τ_{rad}) and a center in a cavity respectively. Assuming a modal volume of $\bar{V} = 1$, modest Q-factors of $\sim 10^3$ are sufficient to have $\tau_{\text{cav}} \approx \tau_{\text{exc}}$ for our lower bound on τ_{exc} .

5.2 Future Work

There are many exciting directions for future work. As stated, work will need to be done to directly measure the excited state lifetime. Such a measurement will determine the radiative efficiency and will help determine the viability of the Si:Se⁺ spin-photon interface operating in a luminescence manner. In this work we have made a multitude of Se-doped Si wafer samples that could be used towards this future measurement.

These sample preparation techniques and optical measurements can also be applied to the other Group VI deep-double donors (sulfur and tellurium) which possess similar ground state Hamiltonians and mid-infrared optical transitions. These alternatives may have favourable optical or quantum mechanical properties over selenium.

Focusing on Si:Se⁺: future work will benefit greatly from the results presented here. Our sample fabrication procedure, our techniques for measuring impurity concentrations, and our results on the effect of impurities on the optical spectra will all be of great use for making new samples or devices. In particular, the incorporation of selenium into photonic devices will need to be developed. This may involve diffusion or ion-implantation, as suggested by Morse et al. [54]. Regardless of technique, the conversion factors tabulated in this work will

undoubtedly be of great use for future samples in which uniform [Se] cannot be achieved or tip-angle measurements cannot be performed.

Perhaps of most importance is the development of high-Q photonic cavities. Our measurements have shown that it is feasible to utilize the Si:Se⁺ spin-photon interface as the basis of a quantum computing/communication platform via strong coupling to photonic cavities. Operating in a luminescence manner may also require the use of photonic cavities to boost the radiative efficiency. Thus, the development of mid-IR photonics devices and the incorporation of selenium is a very promising direction to pursue in order to develop a Si:Se⁺ based integrated silicon quantum optoelectronics.

Bibliography

- [1] G. E. Moore. Cramming more components onto integrated circuits, reprinted from electronics, volume 38, number 8, april 19, 1965, pp.114 ff. *IEEE Solid-State Circuits Society Newsletter*, 11(3):33–35, Sept 2006. ISSN 1098-4232. doi: 10.1109/N-SSC.2006.4785860.
- [2] David C. Brock, editor. *Understanding Moore’s Law – Four Decades of Innovation*. Chemical Heritage Press, Philadelphia, Pennsylvania, 2006.
- [3] Rachel Courtland. Gordon Moore: The Man Whose Name Means Progress. <https://spectrum.ieee.org/computing/hardware/gordon-moore-the-man-whose-name-means-progress>. Online; accessed July 2018.
- [4] A. F. J. Levi. Towards quantum engineering. *Proceedings of the IEEE*, 96(2):335–342, Feb 2008. ISSN 0018-9219. doi: 10.1109/JPROC.2007.911071.
- [5] M Mitchell Waldrop. The chips are down for moore’s law. *Nature News*, 530(7589):144, 2016.
- [6] Stephen Jordan. Quantum algorithm zoo. <https://math.nist.gov/quantum/zoo/>. Online; accessed July 2018.
- [7] Richard P Feynman. Simulating physics with computers. *International journal of theoretical physics*, 21(6-7):467–488, 1982.
- [8] Oak Ridge National Laboratory. Summit. <https://www.olcf.ornl.gov/olcf-resources/compute-systems/summit/>. Online; accessed July 2018.
- [9] Markus Reiher, Nathan Wiebe, Krysta M. Svore, Dave Wecker, and Matthias Troyer. Elucidating reaction mechanisms on quantum computers. *Proceedings of the National Academy of Sciences*, 114(29):7555–7560, 2017. ISSN 0027-8424. doi: 10.1073/pnas.1619152114. URL <http://www.pnas.org/content/114/29/7555>.
- [10] Alejandro Perdomo-Ortiz, Neil Dickson, Marshall Drew-Brook, Geordie Rose, and Alán Aspuru-Guzik. Finding low-energy conformations of lattice protein models by quantum annealing. *Scientific Reports*, 2:571 EP –, Aug 2012. URL <http://dx.doi.org/10.1038/srep00571>. Article.
- [11] Dave Wecker, Bela Bauer, Bryan K. Clark, Matthew B. Hastings, and Matthias Troyer. Gate-count estimates for performing quantum chemistry on small quantum computers. *Phys. Rev. A*, 90:022305, Aug 2014. doi: 10.1103/PhysRevA.90.022305. URL <https://link.aps.org/doi/10.1103/PhysRevA.90.022305>.

- [12] Peter W Shor. Algorithms for quantum computation: Discrete logarithms and factoring. In *Foundations of Computer Science, 1994 Proceedings., 35th Annual Symposium on*, pages 124–134. IEEE, 1994.
- [13] Lov K. Grover. Quantum mechanics helps in searching for a needle in a haystack. *Phys. Rev. Lett.*, 79:325–328, Jul 1997. doi: 10.1103/PhysRevLett.79.325. URL <https://link.aps.org/doi/10.1103/PhysRevLett.79.325>.
- [14] S. Lloyd, M. Mohseni, and P. Rebentrost. Quantum algorithms for supervised and unsupervised machine learning. *ArXiv e-prints*, July 2013. URL <https://arxiv.org/abs/1307.0411>.
- [15] J. R. Petta, A. C. Johnson, J. M. Taylor, E. A. Laird, A. Yacoby, M. D. Lukin, C. M. Marcus, M. P. Hanson, and A. C. Gossard. Coherent manipulation of coupled electron spins in semiconductor quantum dots. *Science*, 309(5744):2180–2184, 2005. ISSN 0036-8075. doi: 10.1126/science.1116955. URL <http://science.sciencemag.org/content/309/5744/2180>.
- [16] P. L. Stanwix, L. M. Pham, J. R. Maze, D. Le Sage, T. K. Yeung, P. Cappellaro, P. R. Hemmer, A. Yacoby, M. D. Lukin, and R. L. Walsworth. Coherence of nitrogen-vacancy electronic spin ensembles in diamond. *Phys. Rev. B*, 82:201201, Nov 2010. doi: 10.1103/PhysRevB.82.201201. URL <https://link.aps.org/doi/10.1103/PhysRevB.82.201201>.
- [17] Rami Barends, Julian Kelly, Anthony Megrant, Daniel Sank, Evan Jeffrey, Yu Chen, Yi Yin, Ben Chiaro, Josh Mutus, Charles Neill, et al. Coherent josephson qubit suitable for scalable quantum integrated circuits. *Physical review letters*, 111(8):080502, 2013.
- [18] D. Leibfried, B. DeMarco, V. Meyer, D. Lucas, M. Barrett, J. Britton, W. M. Itano, B. Jelenkovic, C. Langer, T. Rosenband, and D. J. Wineland. Experimental demonstration of a robust, high-fidelity geometric two ion-qubit phase gate. *Nature*, 422:412 EP –, Mar 2003. URL <http://dx.doi.org/10.1038/nature01492>.
- [19] E. Knill, R. Laflamme, and G. J. Milburn. A scheme for efficient quantum computation with linear optics. *Nature*, 409:46 EP –, Jan 2001. URL <http://dx.doi.org/10.1038/35051009>. Article.
- [20] Tian Zhong, Jonathan M. Kindem, Evan Miyazono, and Andrei Faraon. Nanophotonic coherent light-matter interfaces based on rare-earth-doped crystals. *Nature Communications*, 6:8206 EP –, Sep 2015. URL <http://dx.doi.org/10.1038/ncomms9206>. Article.
- [21] X. Linpeng, M. L. K. Viitaniemi, A. Vishnuradhan, Y. Kozuka, C. Johnson, M. Kawasaki, and K.-M. C. Fu. Coherence properties of shallow donor qubits in ZnO. *ArXiv e-prints*, February 2018.
- [22] Kamyar Saeeadi, Stephanie Simmons, Jeff Z. Salvail, Phillip Dluhy, Helge Riemann, Nikolai V. Abrosimov, Peter Becker, Hans-Joachim Pohl, John J. L. Morton, and Mike L. W. Thewalt. Room-temperature quantum bit storage exceeding 39 minutes using ionized donors in silicon-28. *Science*, 342:830–833, 2013. ISSN 0036-8075. doi: 10.1126/science.1239584. URL <http://science.sciencemag.org/content/342/6160/830>.

- [23] T. F. Watson, S. G. J. Philips, E. Kawakami, D. R. Ward, P. Scarlino, M. Veldhorst, D. E. Savage, M. G. Lagally, Mark Friesen, S. N. Coppersmith, M. A. Eriksson, and L. M. K. Vandersypen. A programmable two-qubit quantum processor in silicon. *Nature*, 555:633 EP –, Feb 2018. URL <http://dx.doi.org/10.1038/nature25766>.
- [24] H. Bernien, B. Hensen, W. Pfaff, G. Koolstra, M. S. Blok, L. Robledo, T. H. Taminiau, M. Markham, D. J. Twitchen, L. Childress, and R. Hanson. Heralded entanglement between solid-state qubits separated by three metres. *Nature*, 497:86 EP –, Apr 2013. URL <http://dx.doi.org/10.1038/nature12016>.
- [25] L. DiCarlo, M. D. Reed, L. Sun, B. R. Johnson, J. M. Chow, J. M. Gambetta, L. Frunzio, S. M. Girvin, M. H. Devoret, and R. J. Schoelkopf. Preparation and measurement of three-qubit entanglement in a superconducting circuit. *Nature*, 467:574 EP –, Sep 2010. URL <http://dx.doi.org/10.1038/nature09416>.
- [26] J. Chiaverini, D. Leibfried, T. Schaetz, M. D. Barrett, R. B. Blakestad, J. Britton, W. M. Itano, J. D. Jost, E. Knill, C. Langer, R. Ozeri, and D. J. Wineland. Realization of quantum error correction. *Nature*, 432:602 EP –, Dec 2004. URL <http://dx.doi.org/10.1038/nature03074>.
- [27] Benjamin J. Metcalf, Justin B. Spring, Peter C. Humphreys, Nicholas Thomas-Peter, Marco Barbieri, W. Steven Kolthammer, Xian-Min Jin, Nathan K. Langford, Dmytro Kundys, James C. Gates, Brian J. Smith, Peter G. R. Smith, and Ian A. Walmsley. Quantum teleportation on a photonic chip. *Nat Photon*, 8(10):770–774, Oct 2014. ISSN 1749-4885. URL <http://dx.doi.org/10.1038/nphoton.2014.217>. Letter.
- [28] Stephanie Simmons, Richard M. Brown, Helge Riemann, Nikolai V. Abrosimov, Peter Becker, Hans-Joachim Pohl, Mike L. W. Thewalt, Kohei M. Itoh, and John J. L. Morton. Entanglement in a solid-state spin ensemble. *Nature*, 470:69 EP –, Jan 2011. URL <http://dx.doi.org/10.1038/nature09696>.
- [29] David P DiVincenzo. The physical implementation of quantum computation. *Fortschritte der Physik: Progress of Physics*, 48(9-11):771–783, 2000.
- [30] Peter W Shor. Scheme for reducing decoherence in quantum computer memory. *Physical review A*, 52(4):R2493, 1995.
- [31] Emanuel Knill, Raymond Laflamme, and Wojciech H. Zurek. Resilient quantum computation. *Science*, 279(5349):342–345, 1998. ISSN 0036-8075. doi: 10.1126/science.279.5349.342. URL <http://science.sciencemag.org/content/279/5349/342>.
- [32] W. K. Wootters and W. H. Zurek. A single quantum cannot be cloned. *Nature*, 299:802 EP –, Oct 1982. URL <http://dx.doi.org/10.1038/299802a0>.
- [33] Valerie Coffman, Joydip Kundu, and William K. Wootters. Distributed entanglement. *Phys. Rev. A*, 61:052306, Apr 2000. doi: 10.1103/PhysRevA.61.052306. URL <https://link.aps.org/doi/10.1103/PhysRevA.61.052306>.
- [34] Charles H Bennett and Gilles Brassard. Quantum cryptography: Public key distribution and coin tossing. *Theor. Comput. Sci.*, 560(P1):7–11, 2014.

- [35] Paul Jouguet, Sébastien Kunz-Jacques, Anthony Leverrier, Philippe Grangier, and Eleni Diamanti. Experimental demonstration of long-distance continuous-variable quantum key distribution. *Nature Photonics*, 7:378 EP –, Apr 2013. URL <http://dx.doi.org/10.1038/nphoton.2013.63>.
- [36] Sheng-Kai Liao, Wen-Qi Cai, Wei-Yue Liu, Liang Zhang, Yang Li, Ji-Gang Ren, Juan Yin, Qi Shen, Yuan Cao, Zheng-Ping Li, Feng-Zhi Li, Xia-Wei Chen, Li-Hua Sun, Jian-Jun Jia, Jin-Cai Wu, Xiao-Jun Jiang, Jian-Feng Wang, Yong-Mei Huang, Qiang Wang, Yi-Lin Zhou, Lei Deng, Tao Xi, Lu Ma, Tai Hu, Qiang Zhang, Yu-Ao Chen, Nai-Le Liu, Xiang-Bin Wang, Zhen-Cai Zhu, Chao-Yang Lu, Rong Shu, Cheng-Zhi Peng, Jian-Yu Wang, and Jian-Wei Pan. Satellite-to-ground quantum key distribution. *Nature*, 549:43 EP –, Aug 2017. URL <http://dx.doi.org/10.1038/nature23655>. Article.
- [37] ID Quantique Inc. <https://www.idquantique.com/quantum-safe-security/overview/qkd-technology/>. Online; accessed July 2018.
- [38] H.-J. Briegel, W. Dür, J. I. Cirac, and P. Zoller. Quantum repeaters: The role of imperfect local operations in quantum communication. *Phys. Rev. Lett.*, 81:5932–5935, Dec 1998. doi: 10.1103/PhysRevLett.81.5932. URL <https://link.aps.org/doi/10.1103/PhysRevLett.81.5932>.
- [39] Cody Jones, Danny Kim, Matthew T Rakher, Paul G Kwiat, and Thaddeus D Ladd. Design and analysis of communication protocols for quantum repeater networks. *New Journal of Physics*, 18(8):083015, 2016. URL <http://stacks.iop.org/1367-2630/18/i=8/a=083015>.
- [40] Koji Azuma, Kiyoshi Tamaki, and Hoi-Kwong Lo. All-photon quantum repeaters. *Nature Communications*, 6:6787 EP –, Apr 2015. URL <http://dx.doi.org/10.1038/ncomms7787>. Article.
- [41] B. E. Kane. A silicon-based nuclear spin quantum computer. *Nature*, 393:133–137, 1998. doi: 10.1038/30156.
- [42] Daniel Loss and David P. DiVincenzo. Quantum computation with quantum dots. *Phys. Rev. A*, 57:120–126, Jan 1998. doi: 10.1103/PhysRevA.57.120. URL <https://link.aps.org/doi/10.1103/PhysRevA.57.120>.
- [43] J. I. Cirac, P. Zoller, H. J. Kimble, and H. Mabuchi. Quantum state transfer and entanglement distribution among distant nodes in a quantum network. *Phys. Rev. Lett.*, 78:3221–3224, Apr 1997. doi: 10.1103/PhysRevLett.78.3221. URL <https://link.aps.org/doi/10.1103/PhysRevLett.78.3221>.
- [44] L.-M. Duan, M. D. Lukin, J. I. Cirac, and P. Zoller. Long-distance quantum communication with atomic ensembles and linear optics. *Nature*, 414:413 EP –, Nov 2001. URL <http://dx.doi.org/10.1038/35106500>. Article.
- [45] Andreas Reiserer and Gerhard Rempe. Cavity-based quantum networks with single atoms and optical photons. *Rev. Mod. Phys.*, 87:1379–1418, Dec 2015. doi: 10.1103/RevModPhys.87.1379. URL <https://link.aps.org/doi/10.1103/RevModPhys.87.1379>.

- [46] Robert Raussendorf and Hans J. Briegel. A one-way quantum computer. *Phys. Rev. Lett.*, 86:5188–5191, May 2001. doi: 10.1103/PhysRevLett.86.5188. URL <https://link.aps.org/doi/10.1103/PhysRevLett.86.5188>.
- [47] Nicolas Sangouard, Christoph Simon, Hugues de Riedmatten, and Nicolas Gisin. Quantum repeaters based on atomic ensembles and linear optics. *Rev. Mod. Phys.*, 83:33–80, Mar 2011. doi: 10.1103/RevModPhys.83.33. URL <https://link.aps.org/doi/10.1103/RevModPhys.83.33>.
- [48] Gary Wolfowicz, Stephanie Simmons, Alexei M. Tyryshkin, Richard E. George, Helge Riemann, Nikolai V. Abrosimov, Peter Becker, Hans-Joachim Pohl, Stephen A. Lyon, Mike L. W. Thewalt, and John J. L. Morton. Decoherence mechanisms of ^{209}Bi donor electron spins in isotopically pure ^{28}Si . *Phys. Rev. B*, 86:245301, Dec 2012. doi: 10.1103/PhysRevB.86.245301. URL <https://link.aps.org/doi/10.1103/PhysRevB.86.245301>.
- [49] Jeff Z. Salvail, Phillip Dluhy, Kevin J. Morse, Michael Szech, Kamyar Saeedi, Julian Huber, Helge Riemann, Nikolai V. Abrosimov, Peter Becker, Hans-Joachim Pohl, and Michael L. W. Thewalt. Optically enabled magnetic resonance study of ^{75}As and ^{121}Sb in ^{28}Si . *Phys. Rev. B*, 92:195203, Nov 2015. doi: 10.1103/PhysRevB.92.195203. URL <https://link.aps.org/doi/10.1103/PhysRevB.92.195203>.
- [50] Guilherme Tosi, Fahd A. Mohiyaddin, Hans Huebl, and Andrea Morello. Circuit-quantum electrodynamics with direct magnetic coupling to single-atom spin qubits in isotopically enriched ^{28}Si . *AIP Advances*, 4(8):087122, 2014. doi: 10.1063/1.4893242. URL <https://doi.org/10.1063/1.4893242>.
- [51] Guilherme Tosi, Fahd A. Mohiyaddin, Vivien Schmitt, Stefanie Tenberg, Rajib Rahman, Gerhard Klimeck, and Andrea Morello. Silicon quantum processor with robust long-distance qubit couplings. *Nature Communications*, 8(1):450, 2017. ISSN 2041-1723. doi: 10.1038/s41467-017-00378-x. URL <https://doi.org/10.1038/s41467-017-00378-x>.
- [52] Andrea Morello, Jarryd J. Pla, Floris A. Zwanenburg, Kok W. Chan, Kuan Y. Tan, Hans Huebl, Mikko Möttönen, Christopher D. Nugroho, Changyi Yang, Jessica A. van Donkelaar, Andrew D. C. Alves, David N. Jamieson, Christopher C. Escott, Lloyd C. L. Hollenberg, Robert G. Clark, and Andrew S. Dzurak. Single-shot readout of an electron spin in silicon. *Nature*, 467:687 EP –, Sep 2010. URL <http://dx.doi.org/10.1038/nature09392>.
- [53] J T Muhonen, A Laucht, S Simmons, J P Dehollain, R Kalra, F E Hudson, S Freer, K M Itoh, D N Jamieson, J C McCallum, A S Dzurak, and A Morello. Quantifying the quantum gate fidelity of single-atom spin qubits in silicon by randomized benchmarking. *Journal of Physics: Condensed Matter*, 27(15):154205, 2015. URL <http://stacks.iop.org/0953-8984/27/i=15/a=154205>.
- [54] Kevin J. Morse, Rohan J. S. Abraham, Adam DeAbreu, Camille Bowness, Timothy S. Richards, Helge Riemann, Nikolay V. Abrosimov, Peter Becker, Hans-Joachim Pohl, Michael L. W. Thewalt, and Stephanie Simmons. A photonic platform for donor spin qubits in silicon. *Science Advances*, 3(7), 2017. doi: 10.1126/sciadv.1700930. URL <http://advances.sciencemag.org/content/3/7/e1700930>.

- [55] M Steger, A Yang, MLW Thewalt, M Cardona, H Riemann, NV Abrosimov, MF Churbanov, AV Gusev, AD Bulanov, ID Kovalev, et al. High-resolution absorption spectroscopy of the deep impurities S and Se in Si 28 revealing the Se 77 hyperfine splitting. *Physical Review B*, 80:115204, 2009.
- [56] M. Hochberg, N. C. Harris, R. Ding, Y. Zhang, A. Novack, Z. Xuan, and T. Baehr-Jones. Silicon photonics: The next fabless semiconductor industry. *IEEE Solid-State Circuits Magazine*, 5(1):48–58, winter 2013. ISSN 1943-0582. doi: 10.1109/MSSC.2012.2232791.
- [57] Mashanovich G. Z., Reed G. T., Timotijevic B. D., and Chan S. P. *Silicon Photonic Waveguides*, chapter 2, pages 15–46. Wiley-Blackwell, 2008. ISBN 9780470994535. doi: 10.1002/9780470994535.ch2. URL <https://onlinelibrary.wiley.com/doi/abs/10.1002/9780470994535.ch2>.
- [58] Yun Wang, Xu Wang, Jonas Flueckiger, Han Yun, Wei Shi, Richard Bojko, Nicolas A. F. Jaeger, and Lukas Chrostowski. Focusing sub-wavelength grating couplers with low back reflections for rapid prototyping of silicon photonic circuits. *Opt. Express*, 22(17):20652–20662, Aug 2014. doi:10.1364/OE.22.020652. URL <http://www.opticsexpress.org/abstract.cfm?URI=oe-22-17-20652>.
- [59] Piero Orlandi, Francesco Morichetti, Michael John Strain, Marc Sorel, Andrea Melloni, and Paolo Bassi. Tunable silicon photonics directional coupler driven by a transverse temperature gradient. *Opt. Lett.*, 38(6):863–865, Mar 2013. doi: 10.1364/OL.38.000863. URL <http://ol.osa.org/abstract.cfm?URI=ol-38-6-863>.
- [60] Bong-Shik Song, Seung-Woo Jeon, and Susumu Noda. Symmetrically glass-clad photonic crystal nanocavities with ultrahigh quality factors. *Opt. Lett.*, 36(1):91–93, Jan 2011. doi: 10.1364/OL.36.000091. URL <http://ol.osa.org/abstract.cfm?URI=ol-36-1-91>.
- [61] Mohsen K. Akhlaghi, Ellen Schelew, and Jeff F. Young. Waveguide integrated superconducting single-photon detectors implemented as near-perfect absorbers of coherent radiation. *Nature Communications*, 6:8233 EP –, Sep 2015. URL <http://dx.doi.org/10.1038/ncomms9233>. Article.
- [62] Michael Riordan. The lost history of the transistor. *IEEE Spectrum*, 41(5):44–46, 2004.
- [63] W. Bludau, A. Onton, and W. Heinke. Temperature dependence of the band gap of silicon. *Journal of Applied Physics*, 45(4):1846–1848, 1974. doi: 10.1063/1.1663501. URL <https://doi.org/10.1063/1.1663501>.
- [64] J. H. Scaff, H. C. Theuerer, and E. E. Schumacher. P-type and n-type silicon and the formation of the photovoltaic barrier in silicon ingots. *JOM*, 1(6):383–388, Jun 1949. ISSN 1543-1851. doi: 10.1007/BF03377436. URL <https://doi.org/10.1007/BF03377436>.
- [65] Silicon (si), indirect energy gap: Datasheet from landolt-börnstein - group iii condensed matter · volume 41a1 β : “group IV elements, IV-IV and III-V compounds. part b - electronic, transport, optical and other properties” in springermaterials

(https://dx.doi.org/10.1007/10832182_434). URL https://materials.springer.com/lb/docs/sm_lbs_978-3-540-31356-4_434. Copyright 2002 Springer-Verlag Berlin Heidelberg.

- [66] P. J. Dean, J. R. Haynes, and W. F. Flood. New radiative recombination processes involving neutral donors and acceptors in silicon and germanium. *Phys. Rev.*, 161: 711–729, Sep 1967. doi: 10.1103/PhysRev.161.711. URL <https://link.aps.org/doi/10.1103/PhysRev.161.711>.
- [67] Sidney Perkowitz. *Optical Characterization of Semiconductors Infrared, Raman, and Photoluminescence Spectroscopy*. Academic Press, Boston, 1993. ISBN 978-0-12-550770-7s.
- [68] Yoon-Suk Kim, Martijn Marsman, Georg Kresse, Fabien Tran, and Peter Blaha. Towards efficient band structure and effective mass calculations for III-V direct band-gap semiconductors. *Phys. Rev. B*, 82:205212, Nov 2010. doi: 10.1103/PhysRevB.82.205212. URL <https://link.aps.org/doi/10.1103/PhysRevB.82.205212>.
- [69] Sokrates T. Pantelides. The electronic structure of impurities and other point defects in semiconductors. *Rev. Mod. Phys.*, 50:797–858, Oct 1978. doi: 10.1103/RevModPhys.50.797. URL <https://link.aps.org/doi/10.1103/RevModPhys.50.797>.
- [70] Bernard Pajot. *Optical Absorption of Impurities and Defects in Semiconducting Crystals*. Springer Series in Solid-State Sciences, 158. 2010. ISBN 1282928813.
- [71] Gordon Davies. The optical properties of luminescence centres in silicon. *Physics Reports*, 176(3):83 – 188, 1989. ISSN 0370-1573. doi: [https://doi.org/10.1016/0370-1573\(89\)90064-1](https://doi.org/10.1016/0370-1573(89)90064-1). URL <http://www.sciencedirect.com/science/article/pii/0370157389900641>.
- [72] Robert C. Hilborn. Einstein coefficients, cross sections, f values, dipole moments, and all that. *American Journal of Physics*, 50(11):982–986, 1982. doi: 10.1119/1.12937. URL <https://doi.org/10.1119/1.12937>.
- [73] D. W. Ditchburn. *Light*. Academic Press, New York, 3rd edition, 1976.
- [74] Alan Corney. *Atomic and Laser Spectroscopy*. Clarendon Press, Oxford, 1977.
- [75] G. Grossmann, K. Bergman, and M. Kleverman. Spectroscopic studies of double donors in silicon. In A. Baldereschi and R. Resta, editors, *Shallow Impurity Centers in Semiconductors*, pages 30 – 46. Elsevier, Oxford, 1987. ISBN 978-0-444-87087-2. doi: <https://doi.org/10.1016/B978-0-444-87087-2.50008-1>. URL <http://www.sciencedirect.com/science/article/pii/B9780444870872500081>.
- [76] David M. Larsen. Inhomogeneous broadening of the lyman-series absorption of simple hydrogenic donors. *Phys. Rev. B*, 13:1681–1691, Feb 1976. doi: 10.1103/PhysRevB.13.1681. URL <https://link.aps.org/doi/10.1103/PhysRevB.13.1681>.
- [77] Manuel Cardona and M. L. W. Thewalt. Isotope effects on the optical spectra of semiconductors. *Rev. Mod. Phys.*, 77:1173–1224, Nov 2005. doi: 10.1103/RevModPhys.77.1173. URL <https://link.aps.org/doi/10.1103/RevModPhys.77.1173>.

- [78] D. Karaiskaj, M. L. W. Thewalt, T. Ruf, M. Cardona, H.-J. Pohl, G. G. Deviatych, P. G. Sennikov, and H. Riemann. Photoluminescence of isotopically purified silicon: How sharp are bound exciton transitions? *Phys. Rev. Lett.*, 86:6010–6013, Jun 2001. doi: 10.1103/PhysRevLett.86.6010. URL <https://link.aps.org/doi/10.1103/PhysRevLett.86.6010>.
- [79] D. Karaiskaj, J. A. H. Stotz, T. Meyer, M. L. W. Thewalt, and M. Cardona. Impurity absorption spectroscopy in ^{28}Si : The importance of inhomogeneous isotope broadening. *Phys. Rev. Lett.*, 90:186402, May 2003. doi: 10.1103/PhysRevLett.90.186402. URL <https://link.aps.org/doi/10.1103/PhysRevLett.90.186402>.
- [80] M. Steger, A. Yang, T. Sekiguchi, K. Saeedi, M. L. W. Thewalt, M. O. Henry, K. Johnston, H. Riemann, N. V. Abrosimov, M. F. Churbanov, A. V. Gusev, A. K. Kaliteevskii, O. N. Godisov, P. Becker, and H.-J. Pohl. Photoluminescence of deep defects involving transition metals in Si: New insights from highly enriched ^{28}Si . *Journal of Applied Physics*, 110(8):081301, 2011. doi: 10.1063/1.3651774. URL <https://doi.org/10.1063/1.3651774>.
- [81] P. T. Landsberg. Non-radiative transitions in semiconductors. *physica status solidi (b)*, 41(2):457–489, 1970. doi: 10.1002/pssb.19700410202. URL <https://onlinelibrary.wiley.com/doi/abs/10.1002/pssb.19700410202>.
- [82] A. E. Siegman. *Lasers*. University Science Books, Sausalito, CA, 1986.
- [83] Malcolm H. Levitt. *Spin Dynamics*. Wiley, Chichester, 2001.
- [84] E. L. Hahn. Spin echoes. *Phys. Rev.*, 80:580–594, Nov 1950. doi: 10.1103/PhysRev.80.580. URL <https://link.aps.org/doi/10.1103/PhysRev.80.580>.
- [85] A. M. Tyryshkin, Z.-H. Wang, W. Zhang, E. E. Haller, J. W. Ager, V. V. Dobrovitski, and S. A. Lyon. Dynamical Decoupling in the Presence of Realistic Pulse Errors. *ArXiv e-prints*, November 2010.
- [86] Gary Wolfowicz, Alexei M. Tyryshkin, Richard E. George, Helge Riemann, Nikolai V. Abrosimov, Peter Becker, Hans-Joachim Pohl, Mike L. W. Thewalt, Stephen A. Lyon, and John J. L. Morton. Atomic clock transitions in silicon-based spin qubits. *Nature Nanotechnology*, 8:881 EP –, Nov 2013. URL <http://dx.doi.org/10.1038/nnano.2013.218>. Corrigendum.
- [87] A. Schweiger. *Principles of pulse electron paramagnetic resonance*. 2001. ISBN 0198506341.
- [88] M. Altarelli. Excited states of double donors in silicon. *Physica B+C*, 117:122–124, March 1983. doi: 10.1016/0378-4363(83)90459-X.
- [89] H. G. Grimmeiss, E. Janzén, and K. Larsson. Multivalley spin splitting of $1s$ states for sulfur, selenium, and tellurium donors in silicon. *Phys. Rev. B*, 25:2627–2632, Feb 1982. doi: 10.1103/PhysRevB.25.2627. URL <https://link.aps.org/doi/10.1103/PhysRevB.25.2627>.

- [90] E. Janzén, R. Stedman, G. Grossmann, and H. G. Grimmeiss. High-resolution studies of sulfur- and selenium-related donor centers in silicon. *Phys. Rev. B*, 29:1907–1918, Feb 1984. doi: 10.1103/PhysRevB.29.1907. URL <https://link.aps.org/doi/10.1103/PhysRevB.29.1907>.
- [91] K. Bergman, G. Grossmann, H. G. Grimmeiss, and M. Stavola. Observation of spin-triplet states for double donors in silicon. *Physical review letters*, 56(26):2827, 1986.
- [92] G. Breit and I. I. Rabi. Measurement of nuclear spin. *Phys. Rev.*, 38:2082–2083, Dec 1931. doi: 10.1103/PhysRev.38.2082.2. URL <https://link.aps.org/doi/10.1103/PhysRev.38.2082.2>.
- [93] Adam DeAbreu, Camille Bowness, Rohan J. S. Abraham, Alzbeta Medvedova, Kevin J Morse, Helge Riemann, Nikolay V. Abrosimov, Peter Becker, Hans-Joachim Pohl, Michael L. W. Thewalt, and Stephanie Simmons. Characterization of the Si:Se⁺ spin-photon interface. In progress.
- [94] Raji Shankar, Rick Leijssen, Irfan Bulu, and Marko Lončar. Mid-infrared photonic crystal cavities in silicon. *Opt. Express*, 19(6):5579–5586, Mar 2011. doi: 10.1364/OE.19.005579. URL <http://www.opticsexpress.org/abstract.cfm?URI=oe-19-6-5579>.
- [95] Joseph Kerckhoff, Luc Bouten, Andrew Silberfarb, and Hideo Mabuchi. Physical model of continuous two-qubit parity measurement in a cavity-QED network. *Phys. Rev. A*, 79:024305, Feb 2009. doi: 10.1103/PhysRevA.79.024305. URL <https://link.aps.org/doi/10.1103/PhysRevA.79.024305>.
- [96] Christoph Simon and William T. M. Irvine. Robust long-distance entanglement and a loophole-free bell test with ions and photons. *Phys. Rev. Lett.*, 91:110405, Sep 2003. doi: 10.1103/PhysRevLett.91.110405. URL <https://link.aps.org/doi/10.1103/PhysRevLett.91.110405>.
- [97] Sean D. Barrett and Pieter Kok. Efficient high-fidelity quantum computation using matter qubits and linear optics. *Phys. Rev. A*, 71:060310, Jun 2005. doi: 10.1103/PhysRevA.71.060310. URL <https://link.aps.org/doi/10.1103/PhysRevA.71.060310>.
- [98] A. Fick. Ueber Diffusion. *Annalen der Physik*, 170:59–86, 1855. doi: 10.1002/andp.18551700105.
- [99] Peter Pichler. *Intrinsic Point Defects, Impurities, and Their Diffusion in Silicon*. Springer-Verlag Wien, 1 edition, 2004.
- [100] G. G. Devyatykh, A. D. Bulanov, A. V. Gusev, I. D. Kovalev, V. A. Krylov, A. M. Potapov, P. G. Sennikov, S. A. Adamchik, V. A. Gavva, A. P. Kotkov, M. F. Churbanov, E. M. Dianov, A. K. Kaliteevskii, O. N. Godisov, H. J. Pohl, P. Becker, H. Riemann, and N. V. Abrosimov. High-purity single-crystal monoisotopic silicon-28 for precise determination of Avogadro’s number. *Doklady Chemistry*, 421(1):157–160, Jul 2008. ISSN 1608-3113. doi: 10.1134/S001250080807001X. URL <https://doi.org/10.1134/S001250080807001X>.

- [101] P Becker, H Friedrich, K Fujii, W Giardini, G Mana, A Picard, H-J Pohl, H Riemann, and S Valkiers. The avogadro constant determination via enriched silicon-28. *Measurement Science and Technology*, 20(9):092002, 2009. URL <http://stacks.iop.org/0957-0233/20/i=9/a=092002>.
- [102] Cheol-Seong Kim, Eiji Ohta, and Makoto Sakata. Electrical properties of selenium-diffused silicon. *Japanese Journal of Applied Physics*, 18(5):909, 1979. URL <http://stacks.iop.org/1347-4065/18/i=5/a=909>.
- [103] Cheol-Seong Kim and Makoto Sakata. Diffusion coefficient of selenium in silicon by sheet hall coefficient measurements. *Japanese Journal of Applied Physics*, 18(2):247, 1979. URL <http://stacks.iop.org/1347-4065/18/i=2/a=247>.
- [104] G. R. Waitkins and C. W. Clark. Selenium dioxide: Preparation, properties, and use as oxidizing agent. *Chemical Reviews*, 36(3):235–289, Jun 1945. ISSN 0009-2665. doi: 10.1021/cr60115a001. URL <https://pubs.acs.org/doi/abs/10.1021/cr60115a001>.
- [105] Aaron L. Stancik and Eric B. Brauns. A simple asymmetric lineshape for fitting infrared absorption spectra. *Vibrational Spectroscopy*, 47(1):66 – 69, 2008. ISSN 0924-2031. doi: <https://doi.org/10.1016/j.vibspec.2008.02.009>. URL <http://www.sciencedirect.com/science/article/pii/S0924203108000453>.
- [106] W. N. Hardy and L. A. Whitehead. Split-ring resonator for use in magnetic resonance from 200-2000 MHz. *Review of Scientific Instruments*, 52(2):213–216, 1981. doi: 10.1063/1.1136574. URL <https://doi.org/10.1063/1.1136574>.
- [107] R. Sauer. Evidence for bound multiple-exciton complexes in silicon. *Phys. Rev. Lett.*, 31:376–379, Aug 1973. doi: 10.1103/PhysRevLett.31.376. URL <https://link.aps.org/doi/10.1103/PhysRevLett.31.376>.
- [108] D. Karaiskaj, M. L. W. Thewalt, T. Ruf, M. Cardona, and M. Konuma. “Intrinsic” acceptor ground state splitting in silicon: An isotopic effect. *Phys. Rev. Lett.*, 89: 016401, Jun 2002. doi: 10.1103/PhysRevLett.89.016401. URL <https://link.aps.org/doi/10.1103/PhysRevLett.89.016401>.
- [109] S Zakel, S Wundrack, H Niemann, O Rienitz, and D Schiel. Infrared spectrometric measurement of impurities in highly enriched ‘Si28’. *Metrologia*, 48(2):S14, 2011. URL <http://stacks.iop.org/0026-1394/48/i=2/a=S02>.
- [110] P. G. Sennikov, T. V. Kotereva, A. G. Kurganov, B. A. Andreev, H. Niemann, D. Schiel, V. V. Emtsev, and H. J. Pohl. Spectroscopic parameters of the absorption bands related to the local vibrational modes of carbon and oxygen impurities in silicon enriched with ^{28}Si , ^{29}Si , and ^{30}Si isotopes. *Semiconductors*, 39(3):300–307, Mar 2005. ISSN 1090-6479. doi: 10.1134/1.1882791. URL <https://doi.org/10.1134/1.1882791>.
- [111] Zhiyi Yu, Y. X. Huang, and S. C. Shen. Spin-orbit splitting of the valence bands in silicon determined by means of high-resolution photoconductive spectroscopy. *Phys. Rev. B*, 39:6287–6289, Mar 1989. doi: 10.1103/PhysRevB.39.6287. URL <https://link.aps.org/doi/10.1103/PhysRevB.39.6287>.

- [112] C. de Tomas, A. Cantarero, A. F. Lopeandia, and F. X. Alvarez. Thermal conductivity of group-IV semiconductors from a kinetic-collective model. *Proceedings of the Royal Society of London A: Mathematical, Physical and Engineering Sciences*, 470(2169), 2014. ISSN 1364-5021. doi: 10.1098/rspa.2014.0371. URL <http://rspa.royalsocietypublishing.org/content/470/2169/20140371>.
- [113] A. M. STONEHAM. Shapes of inhomogeneously broadened resonance lines in solids. *Rev. Mod. Phys.*, 41:82–108, Jan 1969. doi: 10.1103/RevModPhys.41.82. URL <https://link.aps.org/doi/10.1103/RevModPhys.41.82>.
- [114] C. Jagannath, Z. W. Grabowski, and A. K. Ramdas. Linewidths of the electronic excitation spectra of donors in silicon. *Phys. Rev. B*, 23:2082–2098, Mar 1981. doi: 10.1103/PhysRevB.23.2082. URL <https://link.aps.org/doi/10.1103/PhysRevB.23.2082>.
- [115] Sh. M. Kogan and T. M. Lifshits. Photoelectric spectroscopy - a new method of analysis of impurities in semiconductors. *physica status solidi (a)*, 39(1):11–39, 1977. doi: 10.1002/pssa.2210390102. URL <https://onlinelibrary.wiley.com/doi/abs/10.1002/pssa.2210390102>.
- [116] Timothy J. Madison Bradley J. Frey, Douglas B. Leviton. Temperature-dependent refractive index of silicon and germanium. volume 6273, 2006. doi: 10.1117/12.672850. URL <https://doi.org/10.1117/12.672850>.
- [117] A. Yang, M. Steger, T. Sekiguchi, M. L. W. Thewalt, J. W. Ager, and E. E. Haller. Homogeneous linewidth of the 31P bound exciton transition in silicon. *Applied Physics Letters*, 95(12):122113, 2009. doi: 10.1063/1.3238268. URL <https://doi.org/10.1063/1.3238268>.
- [118] Eisuke Abe, Alexei M. Tyryshkin, Shinichi Tojo, John J. L. Morton, Wayne M. Witzel, Akira Fujimoto, Joel W. Ager, Eugene E. Haller, Junichi Isoya, Stephen A. Lyon, Mike L. W. Thewalt, and Kohei M. Itoh. Electron spin coherence of phosphorus donors in silicon: Effect of environmental nuclei. *Phys. Rev. B*, 82:121201, Sep 2010. doi: 10.1103/PhysRevB.82.121201. URL <https://link.aps.org/doi/10.1103/PhysRevB.82.121201>.
- [119] A M Tyryshkin, J J L Morton, S C Benjamin, A Ardavan, G A D Briggs, J W Ager, and S A Lyon. Coherence of spin qubits in silicon. *Journal of Physics: Condensed Matter*, 18(21):S783, 2006. URL <http://stacks.iop.org/0953-8984/18/i=21/a=S06>.
- [120] J. D. Thompson, T. G. Tiecke, N. P. de Leon, J. Feist, A. V. Akimov, M. Gullans, A. S. Zibrov, V. Vuletić, and M. D. Lukin. Coupling a single trapped atom to a nanoscale optical cavity. *Science*, 340(6137):1202–1205, 2013. ISSN 0036-8075. doi: 10.1126/science.1237125. URL <http://science.sciencemag.org/content/340/6137/1202>.
- [121] G. Z. Mashanovich. Mid-IR silicon photonics. In *2016 Progress in Electromagnetic Research Symposium (PIERS)*, pages 789–789, Aug 2016. doi: 10.1109/PIERS.2016.7734471.

- [122] W. Xie, M. Fiers, S. Selvaraja, P. Bienstman, J. Van Campenhout, P. Absil, and D. Van Thourhout. High-Q photonic crystal nanocavities on 300 nm SOI substrate fabricated with 193 nm immersion lithography. *Journal of Lightwave Technology*, 32(8):1457–1462, April 2014. ISSN 0733-8724. doi: 10.1109/JLT.2014.2308061.
- [123] Hiroshi Sekoguchi, Yasushi Takahashi, Takashi Asano, and Susumu Noda. Photonic crystal nanocavity with a Q-factor of 9 million. *Opt. Express*, 22(1):916–924, Jan 2014. doi: 10.1364/OE.22.000916. URL <http://www.opticsexpress.org/abstract.cfm?URI=oe-22-1-916>.
- [124] E. Togan, Y. Chu, A. S. Trifonov, L. Jiang, J. Maze, L. Childress, M. V. G. Dutt, A. S. Sørensen, P. R. Hemmer, A. S. Zibrov, and M. D. Lukin. Quantum entanglement between an optical photon and a solid-state spin qubit. *Nature*, 466:730 EP –, Aug 2010. URL <http://dx.doi.org/10.1038/nature09256>.
- [125] E. M. Purcell, H. C. Torrey, and R. V. Pound. Resonance absorption by nuclear magnetic moments in a solid. *Phys. Rev.*, 69:37–38, Jan 1946. doi: 10.1103/PhysRev.69.37. URL <https://link.aps.org/doi/10.1103/PhysRev.69.37>.
- [126] J. M. Gerard and B. Gayral. Strong Purcell effect for InAs quantum boxes in three-dimensional solid-state microcavities. *Journal of Lightwave Technology*, 17(11):2089–2095, Nov 1999. ISSN 0733-8724. doi: 10.1109/50.802999.